공학박사학위논문

가돌리늄과 $La(Fe,Mn,Si)_{13}H_y$를 활용한 자기 냉동 시스템에 관한 연구

Study on Magnetic Refrigeration System
Using Gadolinium and $La(Fe,Mn,Si)_{13}H_y$

2023년 2월

서울대학교 대학원

기계공학부

최 종 민

가돌리늄과 $La(Fe,Mn,Si)_{13}H_y$를 활용한 자기 냉동 시스템에 관한 연구

Study on Magnetic Refrigeration System
Using Gadolinium and $La(Fe,Mn,Si)_{13}H_y$

지도교수 김 민 수

이 논문을 공학박사 학위논문으로 제출함

2022년 10월

서울대학교 대학원

기계공학부

최 종 민

최종민의 공학박사 학위논문을 인준함

2022년 12월

위 원 장 : ____________________ (인)

부위원장 : ____________________ (인)

위 원 : ____________________ (인)

위 원 : ____________________ (인)

위 원 : ____________________ (인)

Abstract

Study on Magnetic Refrigeration System Using Gadolinium and $La(Fe, Mn, Si)_{13}H_y$

Jongmin Choi
Department of Mechanical Engineering
The Graduate School
Seoul National University

Global regulation on halocarbon refrigerants and intrinsic problems of natural refrigerants demand an alternative to the conventional vapor compression refrigeration system. Moreover, high CO2 emission from the air-conditioning system brings about the necessity for replacement. The magnetic refrigeration (MR) system, in this circumstance, is evaluated as one of the solutions. However, due to the completely distinguished configuration of the system and operating method, the MR system is required to be studied, especially for the operating parameters. Furthermore, the power consumption

by the pump in the MR system is significant when the mass flow rate of the heat transfer fluid (HTF) is large and the operating frequency of the magnet assembly is high. Because these parameters are essential to increase the MR system's cooling capacity, it is necessary to find a method to reduce the pressure drop in the MR system for a better coefficient of performance (COP). Moreover, even though the simulation model was developed by a great number of researchers, the energy equation was not correctly applied using the Nusselt number for the packed bed of the active magnetic regenerators (AMRs). Lastly, the Gadolinium in the MR system should eventually be substituted by an economical material for commercialization because the material is one of the rare-earth materials. Therefore, in this study, the methods for improving the cooling capacity and COP of the MR system are suggested.

In chapter 2, a comprehensive parametric study of the MR system is presented. In addition, the experimental setup and the operating method of the MR system are explained. In this chapter, the new parameter quantifies the synchronization between the magnet assembly and the AMRs, which are called phase shift and blow fraction. The utilization factor, operating frequency, and operating temperature were also evaluated to figure out their effect on the cooling capacity and COP of the MR system. Lastly, the second law of efficiency of the MR system was obtained. According to the experimental results, the best temperature span of the system was 11.5 K in 1.151 Hz in the no-load test. The maximum cooling capacity was 4.82 W in 1.128 Hz, and the highest COP of the system was 2.40. It was also proved that the most effective way for better performance of the MR system was to operate it at the proper operating temperature. It is because the parameter hardly affects the power consumption despite the better cooling capacity.

In chapter 3, a novel approach to reduce the pressure drop of the MR system is suggested. The irregular Gadolinium particles were aligned in the AMR by using the external magnetic field. This AMR was compared to the traditional AMR including randomly packed Gadolinium. The X-ray computed tomography presented that the particles were fairly aligned inside AMR parallel to the flow direction. In contrast, the non-aligned AMR contained irregular particles which were positioned almost perpendicular to the direction of the flow. Moreover, the aligned AMR showed less friction factor than the non-aligned AMR, which was even smaller than the packed bed with spheres obtained by the Carman correlation. In conclusion, this alignment of the irregular particles inside AMR improved the COP of the MR system up to 37.3% with 4.5 K of the temperature span in load condition in 0.56 Hz of the operating frequency.

In Chapter 4, the simulation model is developed, which utilizes the proper energy equation for the Nusselt number correlation for the packed bed. The modified dispersion-concentric model was used for the AMR. Moreover, the modeling of the auxiliary parts was added to the simulation modeling to consider the intrinsic cooling load in the MR system. This thermal load was induced by the bidirectional flow of the HTF which cooled down and heated up the surrounding tubes, repetitively. The simulation results followed the tendency of the temperature span from the experiments. However, the difference in the heat capacity of tubes in the MR system, thermal contact resistance, and simplified geometries resulted in differences between the simulation and experiment. Furthermore, it was verified that the discrepancy between the temperature measured by the HTF and the average temperature of the solid refrigerant is negligible.

In the last chapter, the optimal ratio of the $\mathrm{La(Fe,Mn,Si)_{13}H_y}$ alloys in the AMR with different Curie temperatures is investigated. In the no-load tests, the higher mass ratio of the moderate Curie temperature provided a better temperature span. On the other hand, the less mass ratio of it presented a deficient temperature span to reduce the cold-end temperature. In the load tests, the best mass ratio of the $\mathrm{La(Fe,Mn,Si)_{13}H_y}$ alloys produced 2.23 W of cooling capacity with 4.8 K of the temperature span and 0.8 of the COP. In conclusion, the optimal mass ratios of the $La(Fe, Mn, Si)_{13}H_y$ alloys with 287.9, 292.7, and 297.6 K of Curie temperature were 13.5, 58.0, and 41.4g, respectively.

This study is expected to give an understanding of the MR system to improve its performance for commercialization in the near future.

Keyword: Magnetic refrigeration system, Active magnetic regenerator, Gadolinium, Numerical simulation, Multi-layering, $\mathbf{La(Fe, Mn, Si)_{13}H_y}$

***Identification Number*: 2017-24111**

Contents

List of Figure

List of Table

Nomenclature

A	aera [m^2]
A_c	cross-sectinoal area [m^2]
$\mathrm{COP}_{\mathrm{Carnot}}$	Carnot COP [-]
C	heat capacity [J/K]
c_p	specific heat capacity at constant pressure [J/kg·K]
$D_{hydraulic}$	hydraulic diameter [m]
D_p	particle diameter [m]
D_{S_v}	Sauter mean diameter [m]
f	friction factor [-]
f_{Carman}	Carman friction factor [-]
G	mass flux [$kg/m^2 \cdot s$]
H	magnetic field intensity [A/m]
h_s	heat transfer coefficient between the solid and fluid phase [$W/m^2 \cdot K$]
j_h	heat transfer j factor [-]
j_d	mass transfer j factor [-]
K	permeability of the packed bed [m^2]
k	thermal conductivity [W/m·K]
k_e^o	effective thermal conductivity of a quiescent bed [W/m·K]
L	length of the packed bed [m]
l	length [m]
M	magnetization [A/m]

MSE	mean square error
m	mass [kg]
$\dot{m}$	mass flow rate [kg/s]
N	total number of measured values
Nu	Nusselt number [-]
Pr	Prandtl number [-]
p	pressure [Pa]
$\dot{Q}_c$	cooling capacity [W]
$\dot{Q}_{\mathrm{MCE}}$	heat source by MCE [W]
q	heat transfer rate [W]
R	arbitrary parameter
R_t	thermal resistance [K/W]
Re_d	Reynolds number in a packed bed [-]
Re_f	Reynolds number of fluid [-]
S_v	specific surface area of the particle [m^{-1}]
T	temperature [K]
T_{Curie}	Curie temperature [K]
T_{RTD}	temperature measured by an RTD
$T_{\mathrm{RTD,cal}}$	temperature measured by an RTD for calibration
T_{TC}	temperature measured by a thermocouple
$T_{\mathrm{TC,cal}}$	temperature measured by a thermocouple for calibration
$\bar{T}_{\mathrm{TC,cal}}$	average temperature measured by a thermocouple for calibration
t	time [s]

t_{delay}	time delay [s]
U	interstitial velocity [m/s]
U_o	superficial velocity [m/s]
u	fluid velocity [m/s]
u_s	standard uncertainty
u_c	combined standard uncertainty
u_{cal}	standard uncertainty for calibration
V	volume [m^3]
$\dot{V}$	volumetric flow rate [m^3/s]
$\dot{W}_{\mathrm{m}}$	power consumption by motor [W]
$\dot{W}_{\mathrm{p}}$	power consumption by pump [W]
$\dot{W}_{\mathrm{tot}}$	total power consumption [W]
Δp	pressure drop [Pa]
X	measured value

Greek Letters

α_{ax}	axial fluid thermal dispersion coefficient [m^2/s]
α_s	solid thermal diffusivity [m^2/s]
β_{blow}	blow ratio [-]
ϵ	porosity [-]
η_{2nd}	second law of efficiency [%]
η_{p}	overall efficiency of the pump [-]
μ	dynamic viscosity [Pa·s]

ρ	density [kg/m^3]
τ	torque [N·m]
Φ	utilization factor [-]
φ	phase shift [°]
ω	operating frequency [Hz]

Subscripts

ad	adiabatic
amb	ambient
avg	time average
blow	fluid blow
c	cold-end
cyc	cycle
f	heat transfer fluid
h	hot-end
i	inlet
o	outlet
r	radial direction
s	solid magnetocaloric material
span	span
sys	system
w	water
$wall$	tube wall

x	axial direction

Abbreviations

AMR	active magnetic regenerator
CHEX	cold side heat exchanger
COP	coefficient of performance
Fe	Ferrite
FOPT	first-order phase transition
HHEX	hot side heat exchanger
HTF	heat transfer fluid
La	Lanthanum
MCE	magnetocaloric effect
MCM	magnetocaloric material
Mn	Manganese
MR	magnetic refrigeration
RTD	resistance temperature detector
Si	Silicon
SOPT	second-order phase transition
XCT	X-ray computed tomography
SV	solenoid valve

Chapter 1. Introduction

1.1. Background of the study

About 80% of the refrigeration system in the market utilizes a vapor compression refrigeration cycle. Most of them use halocarbon refrigerants, which contribute to about 10% of greenhouse gas emissions in the world [1], [2]. To prevent climate change, one of the alternatives is a natural refrigerant such as CO2, propane (R290), iso-butane (R600a), or their blends [3]. However, the CO2 cycle induces considerable energy or exergy loss during the expansion process, which leads to low efficiency of the system [4], [5], [6]. On the one hand, R290 and R600a are classified as A3 by ASHRAE 34 due to their flammability, which restricts the cooling capacity of systems by the limited maximum refrigerant charge amount of 500 g [7], [8].

Meanwhile, according to International Energy Agency (IEA), the resultant CO2 emission from space cooling is projected to be from 1,135 Mt in 2016 to 2,070 Mt in 2050 mainly by using fossil fuels for power generation [9]. It was found that the energy consumption for air-conditioning in buildings had been rising to 6% of the total final energy use in 2016 in the world. Most of the energy was consumed in electricity, which accounted for almost 10% (2,000

TWh) of the total electricity use (21,000 TWh) in the world as seen in Figure 1.1 [9]. What is more, according to Isaac and Van Vuuren [10], the electricity demand for air-conditioning is anticipated to be expanded more than 40 times in 2100 compared to 2000, assuming current climate change. These facts imply that an alternative refrigeration system is required for saving energy and preventing greenhouse gas emissions at the same time.

A magnetic refrigeration (MR) system is evaluated as a potential replacement to overcome the drawbacks of the conventional vapor-compression refrigeration system mentioned earlier [11], [12]. It is characterized by comparable or even higher Carnot efficiency of up to 70%, compared to that of around 50% by vapor compression refrigeration [13], [14], [15], [16]. Moreover, it uses solid refrigerants such as Gadolinium-, $\mathrm{La(Fe,Si)_{13}}$- or $\mathrm{(Mn,Fe)_2P}$-based metals so that the MR system is free of halocarbon refrigerants [11], [17], [18].

The MR system uses the magnetocaloric effect (MCE) of those solid magnetocaloric materials (MCMs). It is first experimentally discovered by Weiss and Piccard in 1917 [19], [20]. The MCE is a temperature change of the MCM when a magnetic field varies around it, which is expressed by following assuming isentropic process.

$$dT = -\frac{T}{c_H}\left(\frac{\partial M}{\partial T}\right)_H dH \tag{1.1}$$

where, T is the temperature, c_H is the heat capacity at a constant external magnetic field, H, and M is the magnetization of the MCM [21]. The susceptibility of paramagnetic materials, such as Gadolinium, is inversely proportional to temperature at a constant external magnetic field by Curie's Law, which leads to $\left(\frac{\partial M}{\partial T}\right)_H < 0$ [22]. Hence, the temperature of the MCM rises or drops under increasing $(dH > 0)$ or decreasing $(dH < 0)$ external magnetic field, respectively [18], [23].

The simplified schematic diagram of the MR system is shown in Figure 1.2. As can be seen, the heat transfer fluid (HTF) absorbs or releases heat from hot or cold active magnetic regenerators (AMRs), the temperature change of which depends on the relative position of the moving magnet to the AMRs inducing MCE. This is why the direction of hot or cold blow is shifted during the MR cycle, which is distinguished from the vapor compression refrigeration cycle. Therefore, system configuration, components, materials, and operating parameters for the MR system should be investigated from a different viewpoint to the conventional refrigeration systems.

The AMR is a type of packed bed, which induces large pressure drop while HTF passes through it. Therefore, numerous researches were carried out to reduce the pressure drop by using different shapes of Gadolinium for better COP of the systems, such as parallel plates, microchannels, pins, or wires [24], [25], [26], [27]. Nevertheless, they are still hard to be applied due to their brittleness and high manufacturing cost for commercialization despite their lower power consumption by the hydraulic system [28], [29], [30].

Gadolinium is still a widely adopted MCM because it shows a second-order phase transition having reversible MCE with negligible hysteresis loss [31], [32], [33], [34], [35]. However, Figure 1.3 shows that Gadolinium will be in shortage when MR systems are commercialized. The reason is that it is estimated to be required up to 100 kg for one large system [11], [36], [37]. Moreover, The production or deposit of Gadolinium oxides is extremely minute compared to the other rare earth elements in worldwide [11]. Contrarily, Lanthanum is known as a relatively sufficient rare earth element from the earth's crusts. It is sometimes even omitted from the rare earth group due to its abundance [38], [39], [40]. Its production is also somewhat stable compared to Gadolinium, thanks to the demand from the battery industry [36]. Therefore, the first-order phase transition (FOPT) materials including Lanthanum alloys are promising MCMs to satisfy the future demand in the MR system industry. The FOPT materials, however, possess several drawbacks during the MR cycles. First of all, the volumetric change of the materials during the MCE induces poor fatigue life because the giant MCE comes from the structural transition. Secondly, they have higher hysteresis loss, which leads to magnetic irreversibility. Moreover, they readily react with HTF making corrosion.

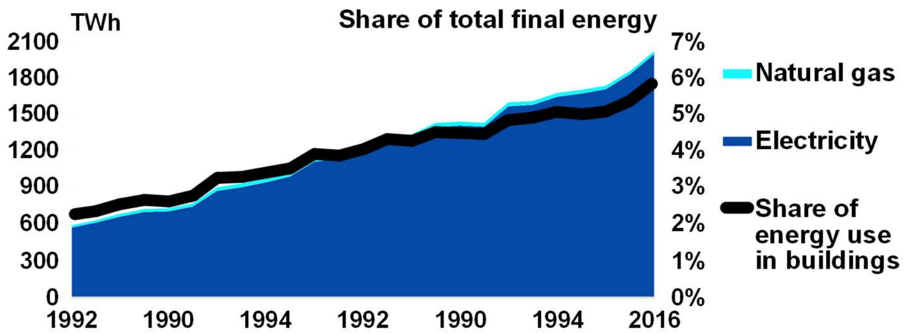

Figure 1.1 Increasing world energy consumption for air-conditioning and the share of it in buildings. Electricity for air-conditioning is the dominant type of energy [9].

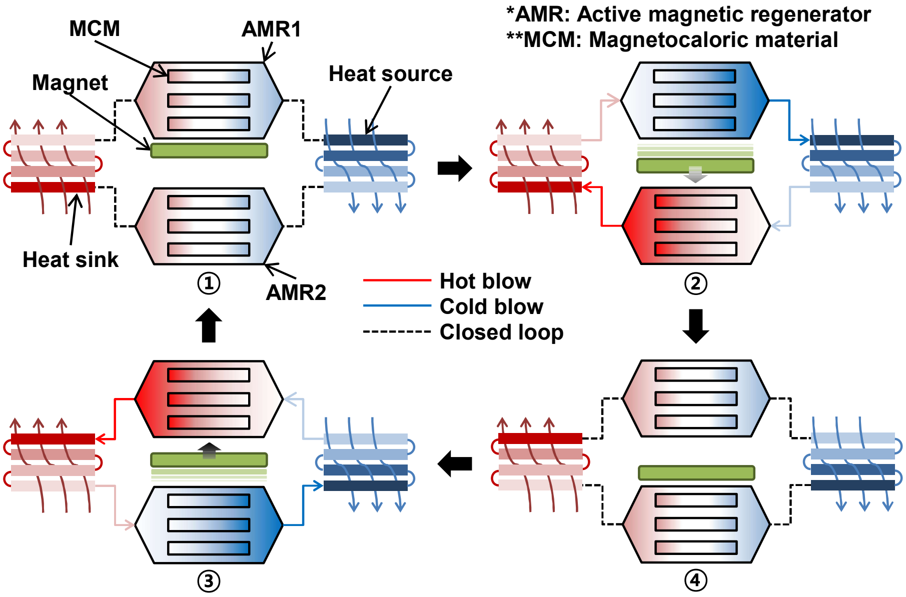

Figure 1.2 Schematic diagram of the magnetic refrigeration cycle. The cycle consists of ① complete magnetization, ② demagnetizing with the cold blow, ③ complete demagnetization, and ④ magnetizing with the hot blow for AMR1. The cycle for AMR2 is equivalent to AMR1 delaying by half-cyclic time.

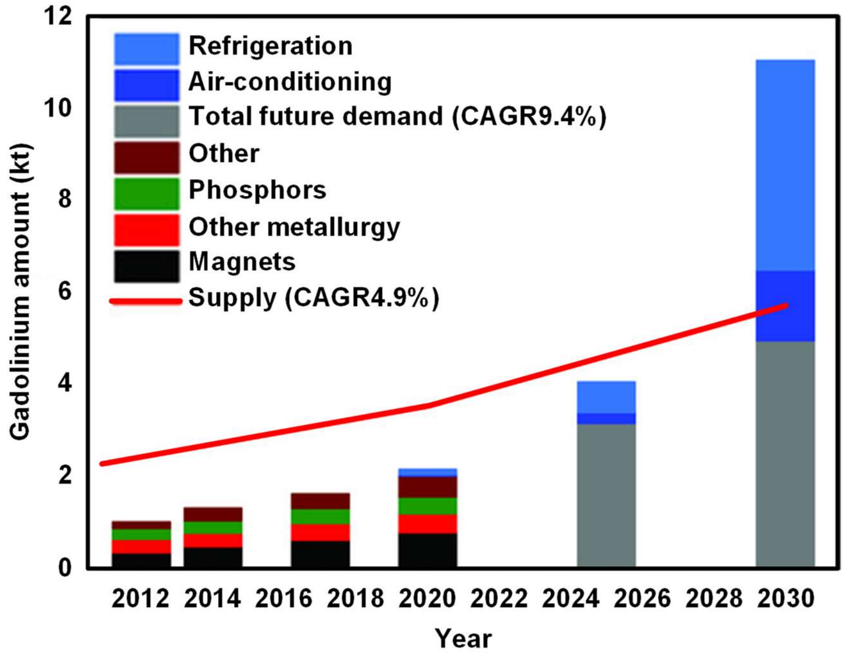

Figure 1.3 Global demand for Gadolinium now and in the future as magnetic refrigeration systems penetrate the market. The supply of Gadolinium is expected not to meet the demand in 2030 based on compound annual growth rates (CAGR) [11].

1.2. Literature survey

1.2.1. Parametric studies on magnetic refrigeration systems using Gadolinium

The utilization factor is the ratio of the heat capacities of the HTF at one blow to the total MCM in the system. It replaces the mass flow rate to quantify the mass of the HTF in a cycle in the MR system. The operating frequency is also an important parameter in the MR system, which is the inverse of one cycle time. This is equivalent to the compressor speed in a conventional vapor compression refrigeration system. Due to the intrinsic thermal load of the MR system, the temperature span in the no-load condition defines the performance of the MR system together with the cooling capacity in the load condition [41]. Therefore, such parameters have been widely studied to understand MR systems by other researchers. Benke et al. [42] devised a magnetic cooling demonstrator using recycled permanent magnets, having 0.95 T of average magnetic flux density in the magnetization area, and multi-layered AMRs with magnetic alloys from La-Fe-Mn-Si. The demonstrator showed a maximum temperature span of 33°C with Gadolinium as a baseline material, and 25°C with 5 staked multi-layered AMRs. In their tests, starting temperature of the system, and the different number of layering of MCMs were considered at 1 Hz of the operating frequency. Nakashima et al. [43] installed an MR system in a wine cooler, which was able to contain 2.24 kg of multilayered MCMs and had a rotary Halbach-arrayed cylindrical magnet presenting 0.98 T on average in an axial direction. The wine cooler maintained 12.5℃ of indoor ambient temperature with 0.38 of COP and 1.6% of the second law of efficiency under the condition of 0.5 Hz of operating frequency and 2.1 LPM of a volume flow rate of HTF. Inside temperature, cooling capacity, COP, and the second law of efficiency were tested as functions of the volumetric flow rate of the HTF, utilization factor, and operating frequency. Different flow waveforms were concerned, but their effects on the performance were not suggested. Griffith et al. [44] suggested a magnetic flux guide, which enabled to alteration of the maximum magnetic flux density in the air gap from 1.13 to 1.45 T in a rotary magnetic assembly, which was called CaloriSMART. According to the result, the system generated 19.3 K and 2.6 K of temperature span at no-load, and 20 W of thermal load condition, respectively, with 25 g of Gadolinium. The test was conducted in various utilization factors, operating frequencies, and cooling powers. Lozano et al. [41] evaluated temperature span, COP, exergetic-equivalent cooling power, and second-law efficiency of a rotary MR system. They considered operating parameters such as operating frequency, heat source, heat sink temperature, and utilization factor using an electric heater as a heat source. At this point, the temperature span is the difference between the hot-end and cold-end temperature of the AMR. In their research, the experimental results show that the cooling capacity of 200 W was achieved when the heat sink temperature was 297.7 K with 16.8 K of temperature span and 1.51 of COP. Huang et al. [45] also invented an MR system, which is named FAME cooler. The MR system had 0.875 T of magnetic flux density, and 1.18 kg of spherical Gadolinium. Temperature span was assessed in different hot-end temperatures, utilization factors, and thermal load. Under the condition of 295 K of the temperature of the hot-end of AMRs and 0.25 of utilization factor, the system produced 11.6 K of the temperature span without a cooling load, 162.4 W of cooling capacity, and 1.59 of COP at zero-temperature span. Li et al. [26] constituted an MR system with 0.06-1.40 T of magnetic flux density, and a single cylindrical AMR in the center of a double cylindrical rotary magnet assembly. The temperature span was tested under the utilization factors, operating frequencies, and cooling loads with different geometries of the MCMs. In their research, irregular Gadolinium performed the maximum temperature span of 14.8 K at the no-load condition with a 0.61 utilization factor. He et al. [46] proposed 3 different configurations of AMRs in their MR system, which generated 1.5 T of magnetic flux density by a rotary magnet assembly and included 277.4 g of spherical Gadolinium. In the experiment, two AMRs were connected in serial and parallel mode, and with an internal heat exchanger in cascade mode. The results showed that 5.66 K, 4.16 K, and 7.35 K of temperature span at no-load condition between 0.5 and 0.9 of utilization factor. In their research, the operating frequency was not suggested. Lionte et al. [47] improved their existing 3D rotary magnet assembly by external metal plates and modified iron yoke, which showed 0.508 T of maximum and 0.489 T of average magnetic flux density, in the magnetization area. The MR system, called BAU with the magnetic assembly was designed to satisfy an industrial purpose and it produced 789 W and 900 W of cooling power with 21.4 K and 18.35 K of temperature span, respectively. The operating frequency was 1.12 Hz and 7 L/min of HTF was measured. In his research, the mass flow rate of the HTF was not presented in a utilization factor. Tagliafico et al. [48] designed and constructed a simplified test setup of the MR system producing 1.55 T of the maximum flux density with a linearly moving AMR made up of 0.36 kg of plate Gadolinium. In their preliminary test, the system showed 2.8℃ of temperature span at 0.127 Hz of operating frequency, and 2.9 of utilization factor, before optimization. The temperature span was presented concerning the various utilization factors at different bypass times. Keawkamrop et al. [49] reformed their previous AMR design for better flow distribution in the MR system. The experimental tests were conducted using the maximum 0.94 T of magnetic field source using 229.82 g of plate Gadolinium. The maximum cooling capacity was 4.68 W in 1.0 of utilization factor, and the temperature span was 1.4 T in no-load condition. The operating frequency was controlled to be 0.16 Hz, and only the utilization factor was varied [50].

1.2.2. Researches on magnetic refrigeration systems using different geometries of Gadolinium

AMR provides a large heat transfer area but substantially causes pressure drops because it is a packed bed. Therefore, numerous researchers experimentally studied the different geometries of the solid refrigerants and their effect on the performance of the MR systems. Tušek et al. [24] conducted a comparative study on three different parallel plates and the other three types of packed beds of Gadolinium. The experimental results say that the parallel plate with the smallest spacing showed the best temperature span of 19.8 K in a no-load condition. The packed beds with spheres and powders result in about 16.0 K and 7.5 K of temperature span in the same no-load conditions. Moreover, the maximum COP was obtained by one of the parallel plates which was superior to the one by the packed bed with spheres of Gadolinium thanks to the relatively low pressure drop. Trevizoli et al. [25] also compared different AMRs with pins, parallel plates, and spheres of Gadolinium. According to the experimental results, the regenerator with sphere showed up to around 21 W of the cooling capacity, which exceeded around 17 W and 9 W of their maximum cooling capacity by the pins and spheres, respectively, in 1 Hz of the operating frequency. In the meantime, the better COP and the second law of efficiency of the system were obtained by the pin-arrayed AMR because of the lower pressure drop than the one with spheres. Li et al. [26] tested AMRs with Gadolinium in the shapes of a plate, sphere, and flake. According to the research, the maximum temperature span was obtained by the flaked Gadolinium having the largest heat transfer area in no-load conditions. The COP was not suggested, but the plated Gadolinium presented the smallest pressure drop by the HTF even though its average porosity was the smallest. For example, each AMR with plated, sphered, and flaked Gadolinium induced 0.6, 1.6, and 2.4 bar, respectively, in 1.0 of the utilization factor and 1.25 Hz of the operating frequency. Spiral Gadolinium wires were also investigated in comparison to the simple Gadolinium wire and particle by Kondo et al. [27]. The results said that 300 W/kg of the best specific cooling capacity was generated by the spiral wires with a diameter of 0.25 mm in 10 Hz. The spheres with a diameter of 0.3 mm, on the other hand, showed a maximum of 61.9 W/kg in 3.0 Hz.

1.2.3. Numerical analysis on magnetic refrigeration systems

Lionte et al. [51] developed a 2D AMR model to study the temperature span, cooling capacity, and COP of the MR system. The MCE was considered as a heat source using experimental results [52]. Plate-type hot and cold side heat exchangers were included in the model to calculate the heat released and absorbed. The MCM is also plate-type Gadolinium, which exchanges heat with fluid in the AMR. The dead zone between the AMR and each heat exchanger was assumed to be thermally insulated. Petersen et al. [53] also conducted numerical research for an AMR in the MR system. The model is in 2D, which is composed of the solid MCM, fluid, and hot and cold side heat exchangers. The MCM was parallel plates, but the correlation for its heat transfer coefficient between the fluid was not suggested. The MCE was calculated assuming that it was the abrupt temperature change of the MCM. Nielsen et al. [54] improved the 2D numerical model for the MR system by Petersen et al. [53]. In the research, the heat loss through the heat exchanger, and plastic flow guide were concerned as thermal resistance. The MCM was in a plate shape, and the MCE by it was considered a a function of the vacuum permeability, external magnetic field, and relative position to the permanent Halbach magnet. However, a detailed description to obtain the MCE was not mentioned, such as the time derivative of the magnetization of the MCM. Kamran et al. [55] verified the feasibility of the microchannel regenerators by 3D numerical analysis for the MR system. The MCE was applied by a source term using polynomial fitting to the $\Delta T_{\mathrm{MCE},ad}$ of Gadolinium, which was a function of the temperature of the MCM. The heat exchangers were modeled by the ϵ-NTU method for their geometries. The Nusselt number correlation for the heat exchanger to the fluid flow was adopted from [56]. Pressure drop was calculated by Darcy friction factors to obtain the power consumption by a pump. Engelbrecht [57] suggested 1D numerical model for an AMR. It consists of sold and fluid phase for the AMR, not including other parts in the entire MR system. The governing equation for thermal analysis for the fluid phase was derived from the energy conservation law. Specifically, the axial dispersion by an eddy flow was considered by the effective static thermal conductivity in a porous media. The MCE was applied by the time derivative of the entropy of the MCM and external magnetic field. Fortkamp et al. [58] carried out a parametric study on the effect of the magnetic circuit, regenerators, and valve system. The numerical method was adopted from the model developed by [59]. The model considered thermal dissipation by the effective thermal conductivity of the packed bed and longitudinal thermal dispersion coefficient. The adiabatic temperature change by the MCE came from the experimental results according to the initial and final external magnetic field, and initial temperature. Therefore, the abrupt temperature change of the MCM occurred by the MCE in the model. In their research, however, the heat transfer coefficient between the fluid and solid phase in the packed bed was not explained. Moreover, the heat loss through the regenerator wall and heat transfer between the other tubes and HTF were not considered. Silva et al. [60] implemented a 1D simulation study to verify the parameters which affect the temperature span of the MR system. In their research, only the energy equation for the solid phase was explained, not including the fluid phase. Moreover, the adiabatic temperature change by MCE and specific heat of Gadolinium were given by Petersen et al. [53]. Hamdani et al. [61] tested a multistage liquefier for hydrogen with six different MCMs using simulation. The Ansys Fluent was utilized so that heat transfer between the MCMs and HTF was dealt with by the coupled-wall method in the software, not suggesting a convective heat transfer correlation. MCE was adopted as a source term during the simulation. The regenerator was a parallel plate, as same as the research mentioned above. Lei et al. [29] compared five geometries of the MCM in the AMRs in the MR system using a 1D transient numerical model. It is noteworthy that the Nusselt number for a packed bed with spheres was based on Engelbrecht [57] where it was referred to Wakao and Kagei [62]. Tušek et al. [63] optimized the plate- and sphere-shaped Gadolinium inside AMRs. The numerical model was based on their other research, where 1D numerical model was developed [64]. The model coupled fluid and solid phase in a packed bed with an effective heat-transfer coefficient term which also accounted for temperature distribution in a perpendicular direction. Thermal dispersion was also considered with the effective thermal conductivity in a packed bed, which corresponds to the thermal conductivity of the fluid due to axial dispersion. Both the adiabatic temperature change by the MCE and the heat capacity of the MCM were adopted from experimental data. Nusselt number correlation for the convective heat transfer between the fluid and solid phase was obtained from Wakao and Kagei [62]. Guo et al. [65] developed a correction factor that accounts for the temperature distribution inside the particles of MCMs. They also conducted the numerical analysis for the AMR which model was based on Tušek et al. [63].

1.2.4. Application of $\mathbf{La(Fe, Mn, Si)_{13}H_y}$ on the magnetic refrigeration systems

La-Fe-Si-based ternary alloy is one of the promising FOPT MCMs because of high adiabatic temperature change by MCE, lower cost, and easily-tunable T_{Curie} [66], [67]. However, the volumetric change of the MCM during MCE causes fast aging during the MR cycles. Moreover, it shows larger hysteresis loss by the change of the external magnetic field [17], [68].

Partial hydrogenation can increase the T_{Curie} of the La(Fe, Si)_{13} with a better life cycle, but it restricts the large production [69]. Instead, Manganese substitution onto the Ferrite position of the fully hydrogenated is widely used to adjust the T_{Curie} leading to $\text{La(Fe, Mn, Si)}_{13}\text{H}_\text{y}$. After fully hydrogenation, T_{Curie} of La(Fe, Si)_{13} shifts to about 350 K, and more Manganese contents lower the T_{Curie} with more SOPT behavior having less hysteresis loss [70], [71], [72].

Under the change of 1 T of the external magnetic field, the temperature range of $\text{La(Fe, Mn, Si)}_{13}\text{H}_\text{y}$ where the entropy change is more than half of the maximum value is only 7 K, which is extremely small compared to 30 K of Gadolinium [71], [73]. This fact means that the range of the operating temperature of that material is narrow so layering the FOPT materials with different Curie temperatures is required for the MR system to provide a broad temperature span [74], [75]. However, a limited number of experiments have been conducted up to date using multi-layered AMRs with $\mathrm{La(Fe,Mn,Si)_{13}H_y}$.

Masche et al. [17] utilized 10 layers of $\mathrm{La(Fe,Mn,Si)_{13}H_y}$ refrigerant of 3.41 kg in total. The layers were decided by the design temperature span of the MR system. With a maximum of 1.44 T of magnetic field source, the system performed 176.1 W of the highest cooling power at 0.38 of utilization factor. When the operating utilization factor was higher than the optimal value, the cooling capacity rapidly dropped. Liang et al. [76] compared four single-layered AMRs containing the same materials as Masche et al. [17]. According to the research, the stabilized $\mathrm{La(Fe,Mn,Si)_{13}H_y}$ by high α-Fe produced the best temperature span of more than 10 K in no-load conditions among the others. Bez et al. [73] tested six types of AMRs with $\mathrm{La(Fe,Mn,Si)_{13}H_y}$ and experimentally evaluated their cooling performance depending on the layers and epoxy bonding. The experimental results say that the highest temperature span of around 13 K was obtained by the double-layered AMR with 2wt% of epoxy contents. The author said that it was attributed to the enhanced mechanical stability from the epoxy bonding. Vieira et al. [77] conducted numerical and experimental methods for the MR system having 3 layers of $\mathrm{La(Fe,Mn,Si)_{13}H_y}$ alloys, which Curie temperatures are 299.9, 303.5, and 307 K. According to their research, the maximum temperature span of 12 K was obtained at 0.5 Hz of operating frequency. Furthermore, the numerical model was validated within a 7% deviation from the no-load temperature span of the experiment. Navickaitė et al. [72] tested the effect of epoxy for bonding $La(Fe, Mn, Si)_{13}H_y$ refrigerants having different Curie temperatures. In the research, the 2 wt% of epoxy resin presented the best temperature spans among 1-4 wt% of it. Furthermore, 5 and 9 layers of AMRs produced stable temperature spans at the no-load conditions in the extended range of utilization factor. In contrast, 2 layers of AMRs showed a better temperature span in the large range of heat sink temperature.

1.3. Objectives and scopes

The main purpose of this study is to find novel methods, which make MR systems to be efficient. The first step is to extensively investigate operating parameters and their effect on an MR system. Next, a novel method using irregular particles of Gadolinium is proposed focusing on reducing power consumption due to the pressure drop of AMRs. Moreover, the new simulation model for the MR system is explained which helps to analyze the multi-layered MCMs in AMRs. And finally, the optimal mass ratios of the $\mathrm{La(Fe,Mn,Si)_{13}H_y}$ alloys with different T_{Curie} are presented for the higher COP of the MR system using a multi-layered AMR. The outline of this study is as follows.

In chapter 2, the parametric study for an MR system is introduced. the experimental setup for the MR system is explained before anything else. Specifically, the essential components of the setup are illustrated, which include a magnet assembly, a hydraulic system, and AMRs. The operating method for the experimental setup is also described during their work. To evaluate the MR system, measured or calculated parameters for the MR system are explained such as utilization factor, temperature span, and cooling capacity. The parameters to be investigated are phase shift, blow fraction, utilization factor, operating frequency, operating temperature, and heat source temperature for the

MR system. In the section of results and discussion, the effect of those parameters on the performance of the MR system are examined.

In chapter 3, a novel arrangement is suggested for the Gadolinium particles in an AMR using an external magnetic field. Both the random and aligned irregular Gadolinium particles in AMRs are prepared first. The inside arrangements for both cases in AMRs are qualitatively investigated using X-ray computed tomography. Moreover, the friction factors are obtained by geometrical data of both AMRs and quantitatively evaluated. What is more, the friction factor for the sphere having the equivalent spherical diameter to the irregular particles is inspected. Finally, temperature span, cooling capacity, and COP for both cases are investigated in the MR system established in Chapter 2. Therefore, it is determined whether the new packing method for the AMR is effective to improve the efficiency of the MR system.

In chapter 4, a new 2D numerical model for the MR system is described. This model uses governing equations for the fluid and solid phases, which were utilized when deriving the Nusselt number correlation for both phases. Moreover, the irregular particles of Gadolinium are applied to the simulation by using a shape factor. The intrinsic cooling load is also considered, which is attributed to the repetitive heating or cooling of tubes by the bidirectional flow. This model is validated with experimental results. This model also verifies whether the hot- or cold-end temperature measured by the HTF traces well the temperature of the MCM. This procedure is necessary for multi-layering because the MCMs must be layered according to their Curie temperatures and the actual solid temperature.

In the last chapter, the optimal mass ratio of $\mathrm{La(Fe,Mn,Si)_{13}H_y}$ alloys in an AMR is determined. These hydride alloys prepared for the tests indicate three different Curie temperatures, such as 287.9, 292.7, and 297.6 K. six different cases are tested with different numbers of inner tubes including $\mathrm{La(Fe,Mn,Si)_{13}H_y}$. For their evaluation, the results of the temperature span are presented in no-load conditions with respect to the utilization factor. The operating temperature and frequency are determined based on the results from Chapter 2, where the best COPs are obtained. In the load tests, the operating temperature and different mass flow rates of water for the thermal load are varied. Therefore, the optimal mass ratio of $\mathrm{La(Fe,Mn,Si)_{13}H_y}$ alloys in the multi-layered AMR is determined considering their Curie temperature, operating temperatures, and the temperature of the water for the thermal load.

Chapter 2. Experimental study on magnetic refrigeration system using Gadolinium

2.1. Introduction

In general, the performance parameters of the MR systems such as temperature span, cooling capacity, COP, or second law of efficiency are expressed in terms of MCMs [72], [78], [79], [80], utilization factor [25], [41], [45], [81], [82], or operating frequency [43], [44], [83]. However, even though the influence of the HTF flow profile was studied, the timing delay for synchronization between the AMRs and magnetic assembly has not been clearly suggested in references [84], [85], [86], [87]. Moreover, most of them use the electric heater for thermal load, where the temperature of the second fluid as a heat source can be underestimated [42], [44], [45], [46], [84], [88], [89], [90]. This, in turn, can lead to the second law of the efficiency of the system being overestimated. Furthermore, the mass flow rate of the second fluid for the thermal load in the heat source heat exchanger cannot be dealt with quantitively when using an electric heater.

In this chapter, the experimental setup for the MR system is introduced, which includes magnet assembly, hydraulic system, and AMRs. Next, various operating parameters are covered to study their effect on the performance parameters of an MR system. First of all, the phase shift is defined to quantify the time delay of the flow profile to the profile of the magnetic flux density during the MR cycle. Blow fraction is also quantified for the flowing time of the HTF during a cycle. The utilization factor is controlled and examined together with the temperature of the HTF at both ends of the AMRs. The performance of the system is also described with respect to the operating frequency, operating temperature, and heat source temperature. As the performance parameters, temperature span, cooling capacity, and COP are presented to find their effect in no-load or load conditions. Moreover, the second law of efficiency of the MR system is suggested during the tests for the heat source temperature.

2.2. Experimental method

2.2.1. Magnetic refrigeration cycle

Figure 2.1 demonstrates a fundamental magnetic refrigeration system, which consists of two active magnetic regenerators (AMR1 and AMR2), a magnet assembly, and a cold side heat exchanger (CHEX). As shown, the HTF passes through the AMR2 and AMR1 by releasing heat to the AMR2 (cold blow) and absorbing heat from the AMR1 (hot blow) during the processes from 1 to 2. At the moment, the AMR1 is fully magnetized, and AMR2 is, on the other hand, demagnetized, which is indicated by 1→2 in Figure 2.2 (a) and (b). The magnet assembly then abruptly moves to the left without the flow of the HTF for the magnetic Brayton cycle. At this time, the fixed AMR1 is out of, and the AMR2 is into the magnetization area, which is indicated by 2' in Figure 2.2 (a). For the magnetic Ericsson cycle, the magnet assembly slowly moves with the flow of the heat transfer fluid as indicated by 2' in Figure 2.2 (b). In the next, the direction of the HTF shifts during the processes from 3 to 4. When the magnet assembly moves to the right coming back to the initial position, the HTF stops flowing which is marked by 4' for the magnetic Brayton cycle in Figure 2.2 (a). For the magnetic Ericsson cycle, the HTF flows while the magnet assembly moves. The T-s diagrams for the magnetic Brayton cycle and for the magnetic Ericsson cycle are expressed in Figure 2.3 (a) and (b), respectively, showing each state from 1 to 4, including 2' and 4'.

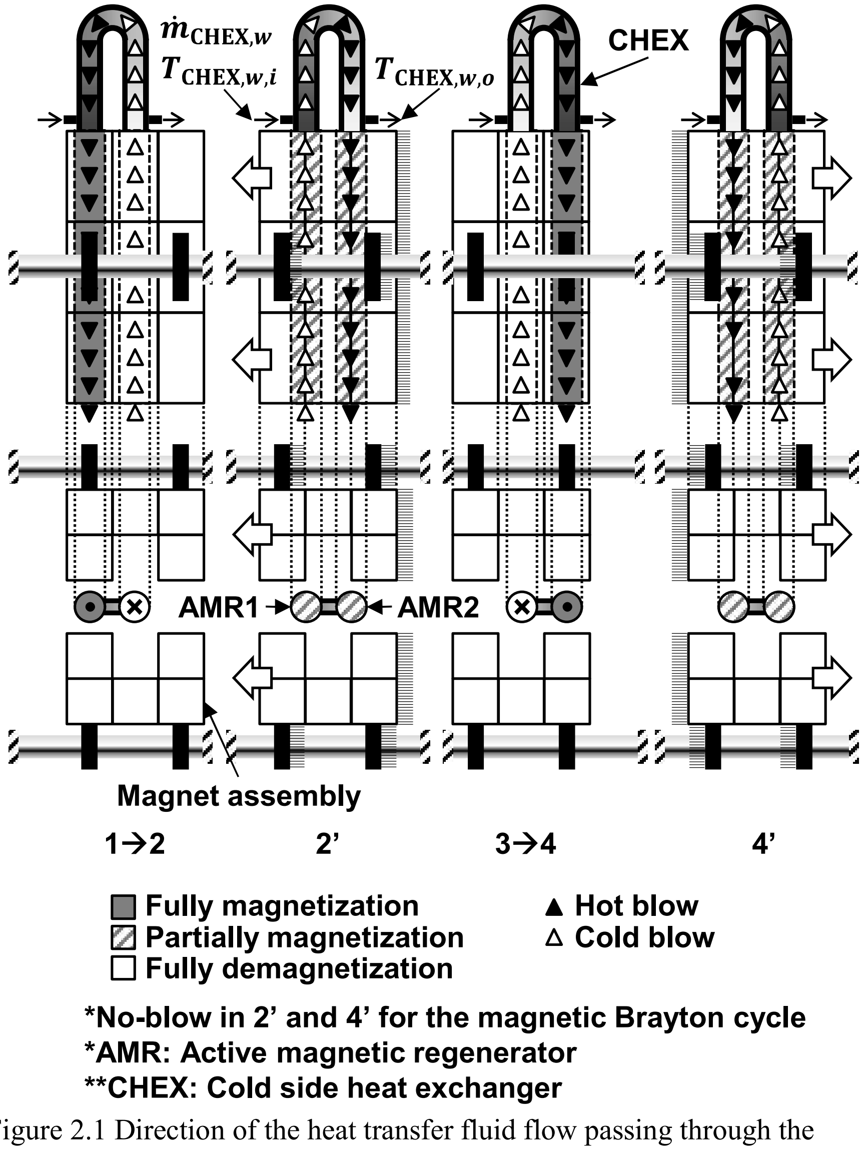

Figure 2.1 Direction of the heat transfer fluid flow passing through the fixed active magnetic regenerator 1, 2, and cold side heat exchanger with respect to the position of the reciprocating magnet assembly.

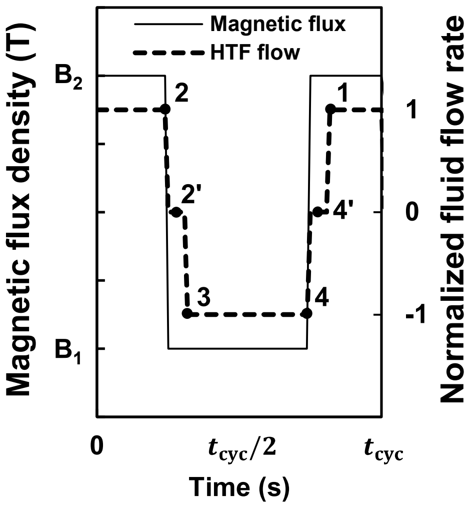

(a)

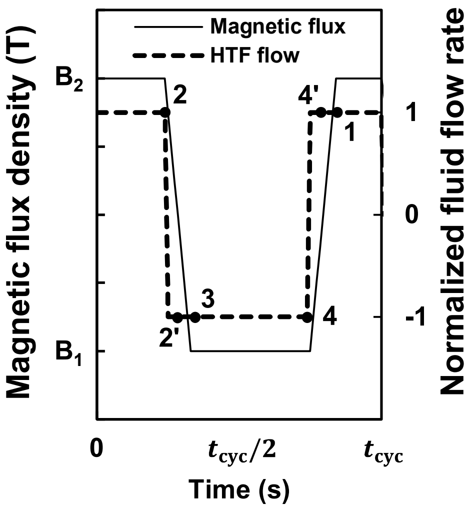

(b)

Figure 2.2 (a) Magnetic flux density and normalized fluid flow profiles for the AMR1 in Figure 2.1 during Mangetic Brayton cycle. (b) Magnetic Ericsson cycle.

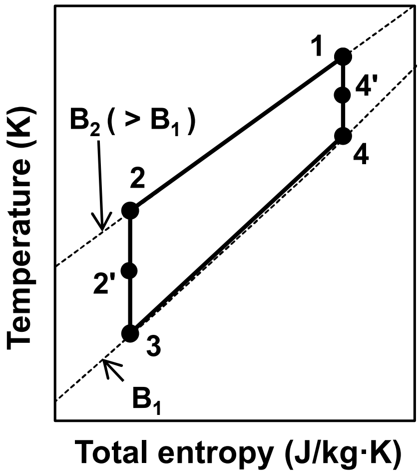

(a)

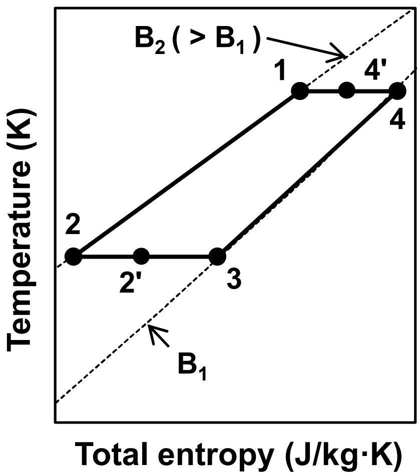

(b)

Figure 2.3 (a) T-s diagram for AMR1 in Figure 2.1 having a magnetic Brayton cycle when the magnetic field changes from B_1 to B_2. (b) T-s diagram for a magnetic Ericsson cycle.

2.2.2. Experimental setup

Figure 2.4 shows the experimental setup for the MR system. The setup consists of a magnetic assembly, AMRs, and a hydraulic system.

First of all, Figure 2.5 demonstrates the schematic diagram of the magnetic assembly. It is constructed with 72 cuboid neodymium magnets, each of them assembled to make up a Halbach array. The Halbach array concentrates the magnetic field in four areas, where the AMRs are positioned. The specifications of the magnets and the magnet assembly are tabulated in Table 2.1. The magnetic flux density is shown in Figure 2.6, which was measured at the center of the air gap for the left side of the magnet assembly by using Tenmars TM-197. As seen in the graph, the magnetic flux density increases as the measurement points are deeper from the $x = 0$. The maximum magnetic flux density of 0.968 T was obtained at $y = 93.75\ \text{mm}$ and $x = 40\ \text{mm}$.

The hydraulic system is controlled by the sequential flow controller in Figure 2.4 (a) to synchronize the flow direction and the position of the reciprocating magnet assembly. The sequential flow controller is composed of four solenoid valves, SV1-SV4, timing relays, R1-R4, and two proximity sensors installed at each end of the magnetic assembly. When the magnet assembly demagnetizes the AMR1 and AMR3 as seen in Figure 2.7, one of the proximity sensors close to AMR1 and AMR3 powers on R1 and R3. At this time, R1 opens and R3 closes the electric circuit. After a few seconds designated by the R1, it closes the electric circuit so that electric power can be delivered to the SV1 and SV3 at the same time as seen in solid gray lines in Figure 2.7. In this time, the HTF can pass through the AMR1 and AMR3, a CHEX, and finally the AMR2 and AMR4 in series as denoted by the black solid lines in Figure 2.7. After the time set by the R3, it opens the circuit so that SV1 and SV3 are closed. In the next half cycle, the same procedures are conducted by the other proximity sensors connected to the R2 and R4 to control the SV2 and SV4 so that cold blow can be supplied to the CHEX again by the AMR 2 and AMR4.

Figure 2.9 shows one of the AMRs. It consists of four inner PTFE tubes including irregular Gadolinium particles sorted by the meshes having aperture sizes from 850 to 500 μm. Those inner tubes are then serially positioned inside a stainless steel 316L tube for the single AMR. Overall, a total of 127.3 g of Gadolinium was prepared inside the four AMRs for the parametric tests. At both ends of the AMRs, T-type thermocouples are installed to measure the hot- and cold-end temperatures of the AMRs. The AMRs are then positioned in the system between the airgap of the magnet assembly as shown in Figure 2.5, the top view of which is also shown in Figure 2.10. As indicated in Figure 2.7 and

Figure 2.8, AMR1 and AMR3 are connected in parallel, and AMR2 and AMR4 are also.

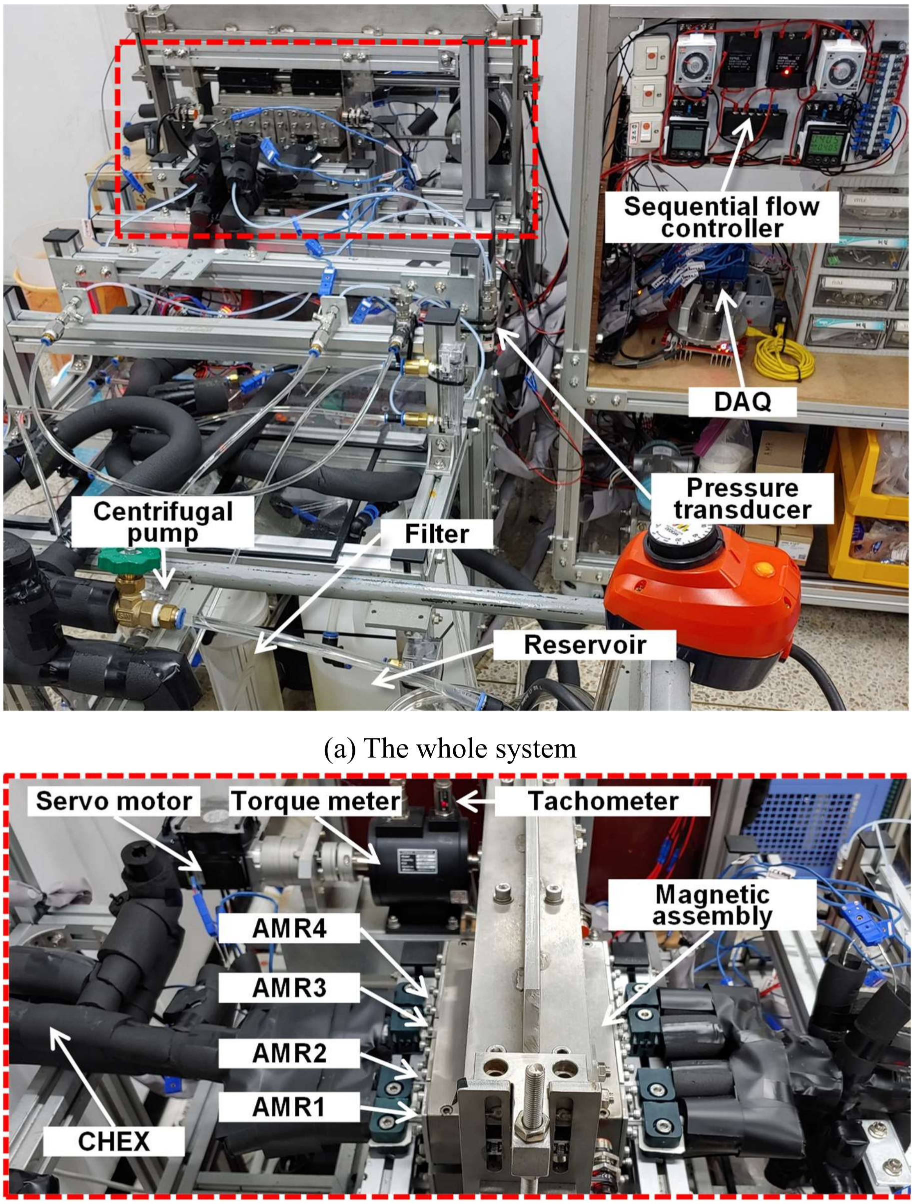

(a) The whole system

(b) Magnetic assembly and active magnetic regenerators

Figure 2.4 System configuration: (a) the whole system and (b) Magnetic assembly and active magnetic regenerators.

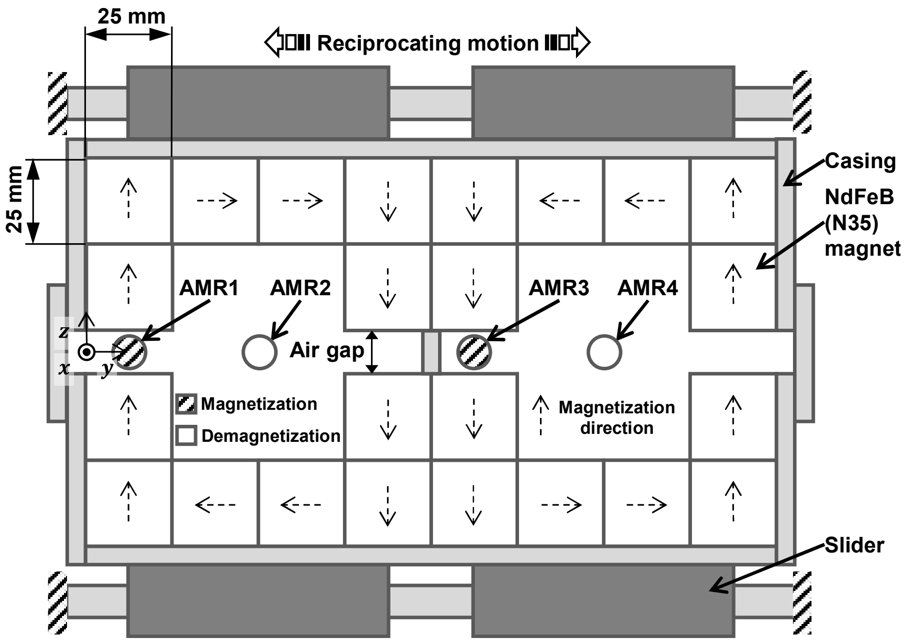

Figure 2.5 The schematic diagram for the front view of the magnetic assembly.

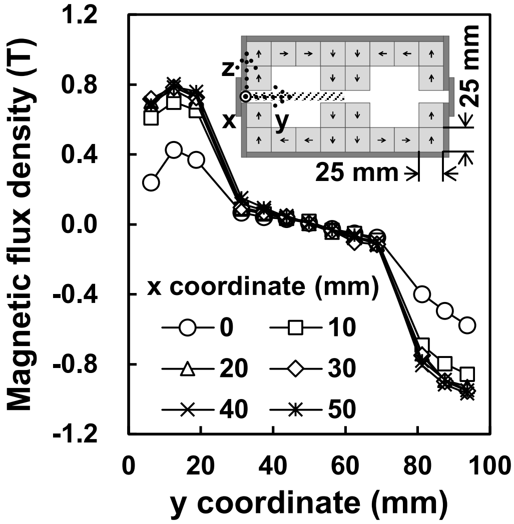

Figure 2.6 Measured magnetic flux density along the y-direction at $z = 0\ \text{mm}$ in different positions in the x-direction in the magnet assembly with a 13 mm air gap.

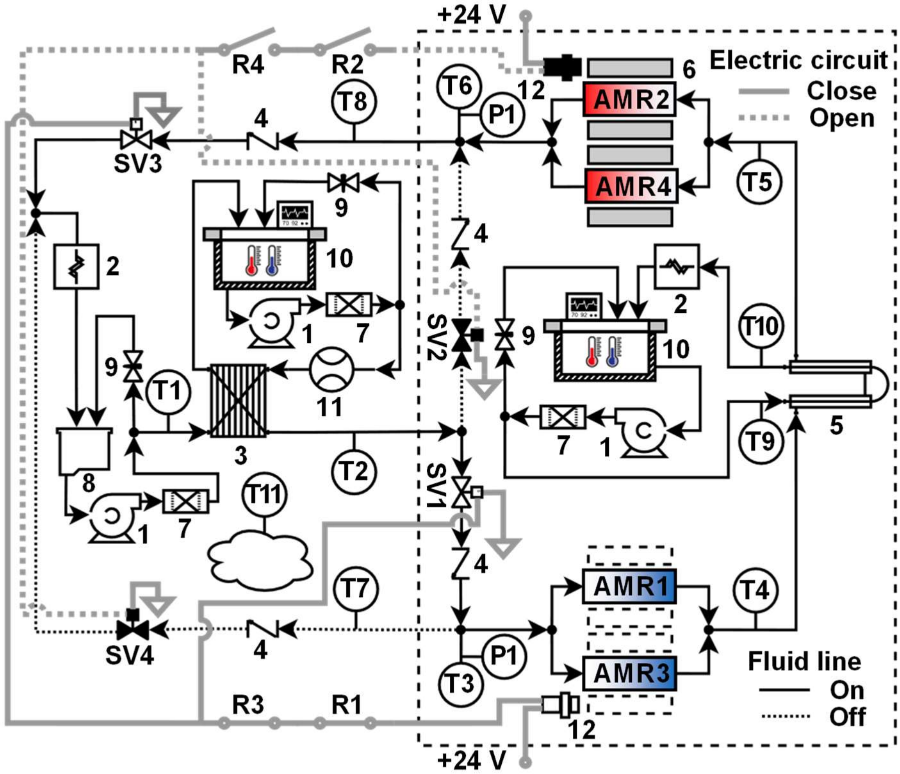

Figure 2.7 The schematic diagram of the experimental setup at (a) first-half and (b) second-half cycle. (1) Centrifugal pump; (2) Coriolis mass flow meter; (3) Hot side heat exchanger (HHEX); (4) Check valve; (5) Cold side heat exchanger (CHEX); (6) Magnet assembly; (7) Filter; (8) Reservoir; (9) Needle valve; (10) Thermostatic water bath; (11) Volumetric flow meter; (12) Proximity sensor; (SV1-4) Solenoid valve 1-4; (AMR1-4) AMR 1-4; (P1-2) Pressure transmitter 1-2; (R1-4) Timing relays 1-4; (T1) $T_{\mathrm{HHEX},f,i}$; (T2) $T_{\mathrm{HHEX},f,o}$; (T3) $T_{\mathrm{AMR1},f}$; (T4) $T_{\mathrm{CHEX},f,1}$; (T5) $T_{\mathrm{CHEX},f,2}$; (T6) $T_{\mathrm{AMR2},f}$; (T7) $T_{\mathrm{AMR1},f,o}$; (T8) $T_{\mathrm{AMR2},f,o}$; (T9) $T_{\mathrm{CHEX},w,i}$; (T10) $T_{\mathrm{CHEX},w,o}$; (T11) T_{amb}.

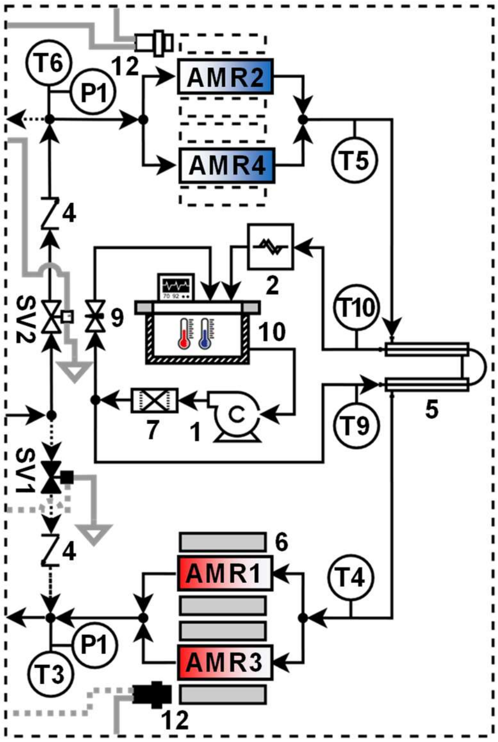

Figure 2.8 Dashed box from Figure 2.7 when the cold blow flows from AMR2 and AMR4 to AMR1 and AMR3.

Table 2.1 Characteristics of the magnets and the magnet assembly.

Parameter	Value
Permanent magnet	NdFeB (N35)
Magnet geometry (width × height × length)	25 mm × 25 mm × 50 mm
Magnet assembly geometry (Magnets only, width × height × depth)	200 mm × 100 mm × 150 mm
Maximum magnetic field in air gap	0.968 T
Minimum magnetic field in air gap	0.005 T
Air gap length	13 mm

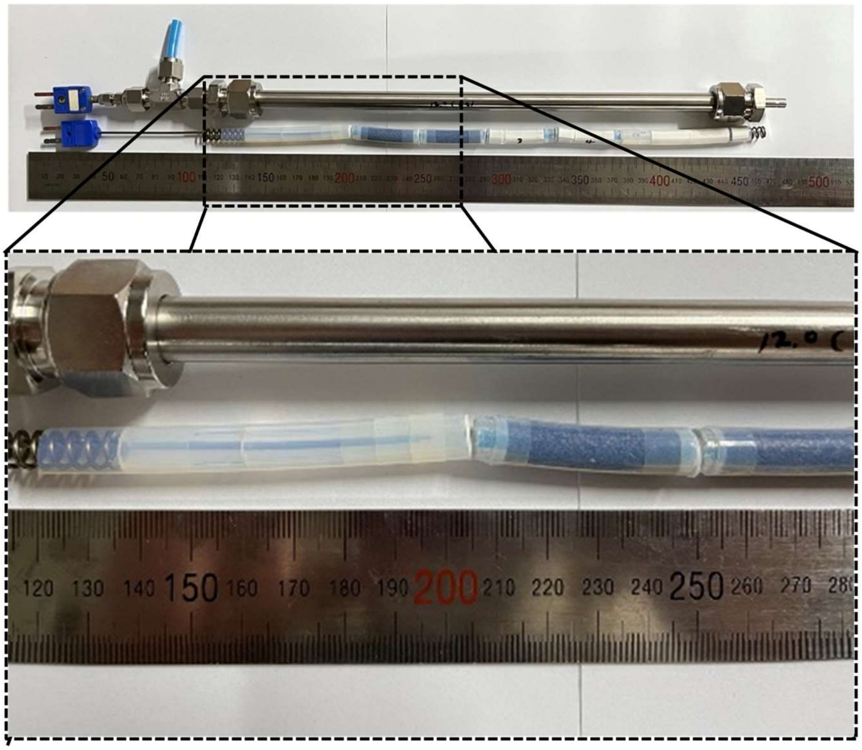

Figure 2.9 An active magnetic regenerator with serially connected four inner tubes containing irregular Gadolinium.

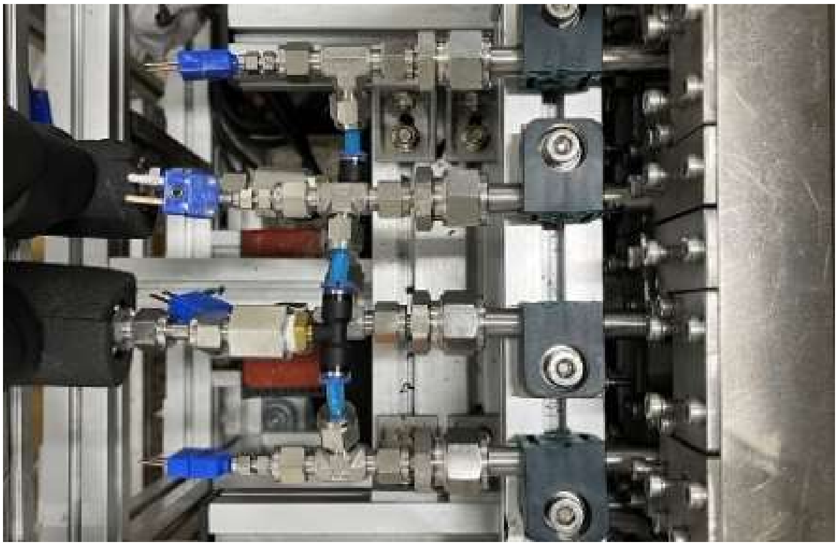

(a)

(b)

Figure 2.10 AMRs installed in the system between the airgap of the magnet assembly. (a) The cold-end of the AMRs connected to the CHEX before insulation, and (b) hot-end of them after insulation.

Table 2.2 Geometric data for the active magnetic regenerators.

Parameter	Value	Unit
Housing material	SUS 316L + PTFE	-
Number of beds	4 (Parallel)	-
Inner diameter	8.5	mm
Outer diameter	12.0	mm
Total effective length	150	mm
Magnetocaloric material (MCM)	Gadolinium	-
MCM geometry	Irregular particle	-
MCM particle size	500-850	μm
MCM total mass	127.3	g
Porosity	0.508	-

2.2.3. Uncertainty analysis of measuring devices

Performance parameters were calculated using experimental data measured by instruments tabulated in Table 2.3. The expanded uncertainties with a 95% confidence level of the parameters are presented in Table 2.4. They were obtained by the following procedure using the standard uncertainties from the measured values (Type A evaluation), and from the accuracy data of each measuring device in Table 2.3 (Type B evaluation).

When an arbitrary parameter R is calculated by a set of measured values, X_i, of a total number of *N*, then it is expressed as

$$R = R(X_1, X_2, \dots, X_N) \tag{2.1}$$

The combined standard uncertainty, u_c, of the parameter R is represented as

$$u_c = \sqrt{\sum_{i=1}^{N} \left(\frac{\partial R}{\partial X_i}\right)^2 u_s^2(X_i)} \tag{2.2}$$

where, $u_s(X_i)$ is the standard uncertainty of the parameter X_i. Finally, the expanded uncertainty is then obtained by u_c multiplied by a coverage factor of 2.0. It is noteworthy that the standard uncertainty of the i-th parameter, X_i, is calculated assuming the true value exists in rectangular distribution using the accuracy of the relevant instrument. The uncertainty caused by the random error is considered with the standard deviation of measured values divided by the root of a total number of them. All the independent standard uncertainty concerned are then combined into the root sum squares to derive the total expanded uncertainty of the parameter.

Temperature measured by T-type thermocouples was calibrated using a precision thermometer (CTR2000, Wikai) and a resistance temperature detector (RTD, CTP 5000-170, Wikai). The linear regression model of temperature by the RTD was regressed onto that by a T-type thermocouple using 30 data in a range from 0 to 50 °C. It is expressed by the least-square fitting as below [91].

$$T_{\mathrm{RTD}} = 0.2957 + 0.9961 \cdot T_{\mathrm{TC}} \tag{2.3}$$

Herein, T_{RTD} and T_{TC} are temperatures measured by an RTD and a thermocouple, respectively. T_{TC} in (2.3) was substituted by the temperature in the system during tests by which calibrated temperature was obtained. The standard uncertainty for calibration, u_{cal}, was obtained according to the equation next, which occurred due to the linear regression [92].

$$u_{\mathrm{cal}} = \sqrt{MSE\left(\frac{1}{n} + \frac{\left(T_{\mathrm{TC}} - \bar{T}_{\mathrm{TC,cal}}\right)^2}{\sum_{j=1}^{n}\left(T_{\mathrm{TC,cal},j} - \bar{T}_{\mathrm{TC,cal}}\right)^2}\right)} \tag{2.4}$$

where MSE is the mean square error of the linear model which is defined by

$$MSE = \sum_{j=1}^{n} \frac{\left(T_{\mathrm{RTD,cal},j} - 0.2957 - 0.9961 \cdot T_{\mathrm{TC,cal},j}\right)^2}{(n-2)} \tag{2.5}$$

Herein, $T_{\mathrm{TC,cal},j}$ is the j-th temperature measured by the thermocouple for calibration, and $\bar{T}_{\mathrm{TC,cal}}$ is their average with a total number of n. $T_{\mathrm{RTD,cal},j}$ is the j-th temperature measured by the RTD for calibration corresponding to $T_{\mathrm{TC,cal},j}$.

Table 2.3 Measuring instruments and their specifications by manufacturers

Sensors	Range	Accuracy
Platinum resistance thermometer	-200–962 °C	±0.3 °C Annual drift ±0.01 °C
T-type thermocouple	-250–350 °C	±0.5 °C
Mass flow meter	0.2–60 kg/h	±0.2% RD
	0.001–1.920 kg/h	±0.2% RD
Pressure transmitter	0–400 kPa	±0.5% FS
	0–600 kPa	
Torque meter	0–19.62 N m	Nonlinearity ±0.1% RO Hysteresis ±0.1% RO Repeatability ±0.1% RO
Electronic balance	2–500 g	±0.05 g
Magnetic field meter	0-2000.0 mT	±(4% RD + 1.0 mT)
Proximity sensor	3.5–5.0 mm	±0.75 mm

Table 2.4 Expanded uncertainties of the system parameters

Parameter	Expanded uncertainty (95% confidence level, coverage factor, k=2)
T	±0.3 K
T_{span}	±0.5 K
Δp_f	±4 kPa
τ	±0.04 N m
$\dot{m}_f$	±0.08 kg/h
$\dot{m}_w$	±0.002 kg/h
m_s	±0.1 g
ω	±0.1 Hz
Φ	±0.04
$\dot{Q}_c$	±0.5 W
$\dot{W}_{\mathrm{p}}$	±0.02 W
$\dot{W}_{\mathrm{m}}$	±0.2 W
$\dot{W}_{\mathrm{tot}}$	±0.2 W
COP	±0.2

2.2.4. Performance parameters

Phase shift, φ, is about the time delay of the flow profile to the magnetic flux density profile in one cyclic time of the MR system as seen in Figure 2.11. It is defined as follows.

$$\varphi = t_{\text{delay}} * \omega * 360 \tag{2.6}$$

where, t_{delay} is the lagging time of the flow profile after the magnetic flux density profile starts in one MR cycle. ω is the operating frequency of the MR cycle, or the speed of the magnet assembly to reciprocate.

Blow ratio, β_{blow}, is ratio of the blow time of the hot or cold blow to the half cyclic time defined by

$$\beta_{\text{blow}} = \frac{t_{\text{blow}}}{\left(\frac{t_{\text{cyc}}}{2}\right)} \tag{2.7}$$

where, t_{blow} is the blow time for the HTF, and t_{cyc} is the cyclic time for the MR cycle.

Utilization factor is defined as the ratio of the total thermal capacity of the MCMs in AMRs to it of HTF at one blow. It is expressed as below.

$$\Phi = \frac{m_{f,\text{blow}} c_{p,f}}{m_s c_{p,s}} = \frac{\dot{m}_{f,\text{avg}} c_{p,f}}{2 m_s c_{p,s} \omega} \tag{2.8}$$

Herein, $m_{f,\text{blow}}$ is the total mass of the HTF during the cold or hot blow at one cycle. $\dot{m}_{f,\text{avg}}$ is the time-averaged mass flow rate and $c_{p,f}$ is the specific heat at a constant pressure of the HTF. Besides, m_s is the total mass and $c_{p,s}$ is the specific heat at a constant pressure under the zero external magnetic field of the MCM. It is noted that $c_{p,f}$ and $c_{p,s}$ were assumed as 4,190 J/kg K and 350 J/kg K for Gadolinium [93].

Temperature span, T_{span}, was defined below.

$$T_{\text{span}} = T_h - T_c \tag{2.9}$$

This parameter demonstrates the highest temperature of the HTF in the system subtracted by its lowest temperature. In no-load conditions, the temperature span is utilized to determine the performance of the MR system.

Both hot- and cold-end temperatures, T_h and T_c, are calculated as below.

$$T_h = \frac{T_{\text{AMR1},f} + T_{\text{AMR2},f}}{2} \tag{2.10}$$

$$T_c = \frac{T_{\text{CHEX},f,1} + T_{\text{CHEX},f,2}}{2} \tag{2.11}$$

The temperatures, $T_{\text{AMR1},f}$, $T_{\text{AMR2},f}$, $T_{\text{CHEX},f,1}$, and $T_{\text{CHEX},f,2}$, in (2.10) and (2.11) were measured by T3, T6, T4, and T5 denoted in the schematic diagram of the system in Figure 2.7 or Figure 2.8. Most of all, those temperatures are measured under the steady state condition of the system.

In load conditions, the cooling capacity, $\dot{Q}_c$, of the MR system is calculated by

$$\dot{Q}_c = \dot{m}_w c_{p,w}\left(T_{\text{CHEX},w,i} - T_{\text{CHEX},w,o}\right) \tag{2.12}$$

Herein, $\dot{m}_w$ is the mass flow rate of water supplied to the cold side heat exchanger (CHEX) for a thermal load. $c_{p,w}$ is the specific heat capacity of the water. Moreover, $T_{\mathrm{CHEX},w,i}$, and $T_{\mathrm{CHEX},w,o}$ are the temperature of the water at the inlet and outlet of the CHEX. During the load tests, $\dot{m}_w$ is varied for a different thermal load to the system. Furthermore, $T_{\mathrm{CHEX},w,i}$ is controlled to be the certain value for the test condition.

The COP of the MR system is calculated as follows.

$$\mathrm{COP} = \frac{\dot{Q}_c}{\dot{W}_{\mathrm{tot}}} \tag{2.13}$$

Herein, total power consumption by the MR system, $\dot{W}_{\mathrm{tot}}$, is a summation of the power consumption by the pump, $\dot{W}_{\mathrm{p}}$, and motor, $\dot{W}_{\mathrm{m}}$. Those values are also calculated with measured parameters as below, respectively.

$$\dot{W}_{\mathrm{p}} = \frac{\dot{m}_f \, \Delta p_{f,\mathrm{sys}}}{\eta_{\mathrm{p}} \rho_f} \tag{2.14}$$

$$\dot{W}_{\mathrm{m}} = 2\pi\omega\tau \tag{2.15}$$

where, $\dot{m}_f$ is the mass flow rate of the HTF, $\Delta p_{f,\mathrm{sys}}$ is the pressure drop by the HTF passing through the entire AMRs in the MR system. The value is calculated by the correlation with respect to $\dot{m}_f$. η_{p} is the pump efficiency assumed as 0.7 by literature during the tests. In (2.15), ω is the operating frequency of the MR system, which represents the speed of the magnetic assembly for one reciprocating cycle. τ is the torque generated by the servo motor to overcome the magnetic force between the magnetic assembly and MCMs in the AMRs.

The second law of efficiency is defined as below.

$$\eta_{2nd} = \frac{\mathrm{COP}}{\mathrm{COP}_{\mathrm{Carnot}}} \times 100(\%) \tag{2.16}$$

Herein, the Carnot COP of the system, $\mathrm{COP}_{\mathrm{Carnot}}$, is calculated using the heat source and heat sink temperature, which are T_L and T_H, respectively, as follows.

$$\mathrm{COP}_{\mathrm{Carnot}} = \frac{T_L}{T_H - T_L} \tag{2.17}$$

where, T_L and T_H are defined in the MR system as below.

$$T_L = \frac{T_{\mathrm{CHEX},w,i} + T_{\mathrm{CHEX},w,o}}{2} \tag{2.18}$$

$$T_H = T_{\mathrm{HHEX},f,o} \tag{2.19}$$

In (2.18), T_L means the average temperature of the second fluid at the inlet and the outlet of the CHEX. Moreover, (2.19) says that the heat source is assumed to have infinite thermal capacity.

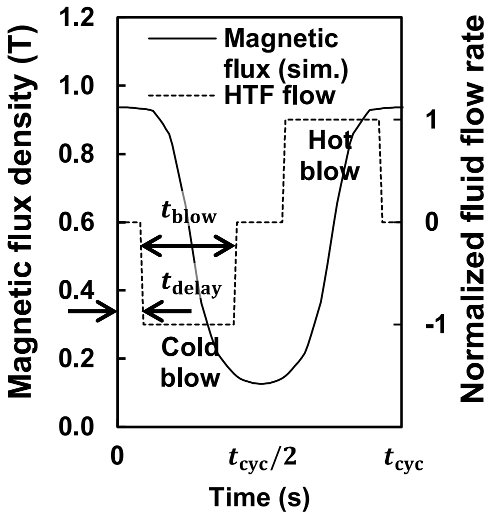

Figure 2.11 Magnetic flux density and normalized fluid flow profiles having a phase shift corresponding to the time delay, t_{delay} when $\beta_{\mathrm{blow}} = 0.66$.

2.2.5. Test procedure

The parameters to be tested in this research are presented in Table 2.5. The phase shift is tested ahead of all the other parameters. The optimal value of the phase shift is then applied during other parametric studies. In the next, the optimal utilization factor is to be found from 0.031 to 0.476. The optimal value of the parameter is determined by the maximum temperature span or the lowest cold-end temperature. Another parameter to affect the performance of the MR system is operating frequency. The higher operating frequency improves the temperature span or cooling capacity in the system, but it may diminish the COP due to more power consumption by the motor. According to data, the MCE is maximized around the Curie temperature of Gadolinium. Therefore, the system performance and efficiency are evaluated under various operating temperatures of the system in 294.8, 296.8, 298.8, 300.8 K. Last but not least, the COP and second law of efficiency of the system are obtained under the heat source temperature of 291.2, 292.2, 293.0, 294.0 K.

The parameters for the system performance such as temperature span, cooling capacity, and COP are acquired during the test under the steady state condition. The steady steady-state is determined by the standard deviation of hot- and cold-end temperature under 0.1 K for 10 minutes.

Table 2.5 Experimental conditions.

Parameter	Values
Phase shift (°)	10.4 – 109.9
Utilization factor (-)	0.031 – 0.476
Operating frequency (Hz)	0.719, 0.999, 1.128
Operating temperature (K)	294.8, 296.8, 298.8, 300.8
Heat source temperature (K)	291.2, 292.2, 293.0, 294.0

2.3. Results and discussion

It can be seen that the phase shift drastically affects the temperature span of the system in Figure 2.12 (a). It can also be found that the optimal phase shift becomes smaller when the blow ratio is operated to be longer. It is because cold blow (or hot blow) can be flooded into the magnetized (or demagnetized) AMRs when the phase shift is too large in high blow ratio. Moreover, enough phase shift should be guaranteed during the system operation so the HTF can exchange heat with fully magnetized or demagnetized MCMs. Nonetheless, the maximum temperature span was maintained almost the same as 11.0, 10.8, and 11.1 K at 0.6, 0.8, and 1.0 of blow ratio. This fact suggests that the blow ratio hardly affects the performance of the MR system provided that the phase shift is appropriate. The effect of the operating frequency on the phase shift is also shown in Figure 2.12 (b). The blow ratio was controlled to be fixed as 0.8 during the tests. As the result says, the optimal phase shifts are almost similar regardless of the operating frequency in Figure 2.12 (b) compared to the effect of the blow ratio in Figure 2.12 (a). In other words, this result implies that when the blow ratio is the same, the operating phase shift can be controlled by referring to the optimal value from Figure 2.12 (a) in any operating frequency.

Figure 2.13 (a) shows the trend of the temperature span according to different utilization factors in no-load conditions. In 0.990 and 1.151 Hz of the operating frequency, the optimal utilization factor seems to be less than 1.0 to maximize the temperature span of the system. However, the cold-end temperature deteriorated in Figure 2.13 (b) as the utilization factor is getting smaller. This is because the enough amount of the mass flow rate of the HTF was not supplied to the AMRs. That is to say, the improvement of the temperature span was only due to the high hot-end temperature when the utilization factor was less than 1.0 as seen in Figure 2.13 (b). Therefore, the optimal utilization factor should be determined in consideration of the hot- and cold-end temperature as well, not only by the temperature span. The optimal temperature span, therefore, is around 0.24 where the lowest value of the cold-end temperature is observed in every operating frequency in Figure 2.13 (b).

In a load condition, the cooling capacity of the system improves as the utilization factor expands in Figure 2.14 (a). It is because higher utilization factor led to more heat capacity at one blow. However, the COP rapidly declines as the utilization factor is higher in Figure 2.14(b). As illustrated in Figure 2.15 (a), it is because of the abrupt increment of the power consumption by the pump as the utilization factor is enlarged. The proportional relationship between the utilization factor and power consumption by the pump is attributed to the quadratic relationship between the mass flow rate of the HTF and the pressure drop passing through the AMRs. Thus, these results from Figure 2.14 to Figure

2.15 say that an appropriate amount of utilization factor should be supplied in the MR system to simultaneously secure a decent temperature span, cooling capacity, and COP.

The influence of the operating frequency on the system performance is suggested in Figure 2.16 and Figure 2.17. As predicted, the higher operating frequency causes a better temperature span in Figure 2.16 (a) and cooling capacity in Figure 2.16 (b) at the same mass flow rate of the water supplied to the CHEX for a thermal load. It is because more MCE occurred in a unit of time in the higher operating frequency. This phenomenon enhanced the amount of heat absorbed from the heat source and released to the heat sink during every refrigeration cycle. However, the COP is getting worse as the operating frequency increase for higher cooling capacity at the same mass flow rate of the water to the CHEX as shown in Figure 2.17 (a). As mentioned earlier, higher frequency enables the system to have a greater number of MCE in a unit of time. This means that it dedicates more total mass flow rate of HTF in the unit time as well. In other words, higher frequency causes limited duration for the flow so more mass flow rate of HTF was required for the same utilization factor. Therefore, more power consumption by the motor and pump is induced at the same time with increasing operating frequency as presented in Figure 2.17 (b).

Another parameter to be considered in an MR system is operating temperature. It is the temperature of the HTF flowing into the AMRs after it passes through the HHEX, $T_{\mathrm{HHEX},f,o}$. It should be noted that the HHEX is the heat sink in the system. Figure 2. (a) and (b) demonstrate that as the operating temperature lowers, the temperature span and cooling capacity improve at the same time in every mass flow rate of the water in CHEX.

On the one hand, the cooling capacity drops more quickly at a higher mass flow rate of the water in the CHEX, $\dot{m}_{\mathrm{CHEX},w}$, as the operating temperature increases. In other words, the slope of the line marked by the black diamonds is higher than the one by the black squares in Figure 2. (a). It is because as the more thermal load is supplied, the cold-end temperature of the AMRs moves apart from the Curie temperature of the Gadolinium, but the extent is substantial when $\dot{m}_{\mathrm{CHEX},w}$ is higher as seen in Figure 2. (b). Because the MCE maximizes around the Curie temperature, the resultant cold-end temperature diminished the system performance, such as the cooling capacity, faster when $\dot{m}_{\mathrm{CHEX},w}$ was higher.

It is noteworthy that the improvement of the cooling capacity in Figure 2.19 (a) proportionally affects the COP in Figure 2.19 (b) with respect to the operating temperature. It is because the operating temperature does not influence the power consumption by the motor and pump in the system as shown in Figure 2.20. This fact contrasts with the utilization factor and operating frequency where a higher value of them considerably deteriorated the COP while increasing the cooling capacity in the MR system. In other words, adjusting the operating temperature close to the Curie temperature is the most effective way in MR systems to provide cooling capacity.

To evaluate the system by calculation of the second law of efficiency, different heat source temperature, $T_{\mathrm{CHEX},w,i}$, was tested as shown in Figure 2.21 and Figure 2.22. First of all, cooling capacity and COP are adversely affected as the heat source temperature reduces in Figure 2.21 (a) and (b). It is because of the less temperature difference between the heat source temperature and the temperature of the HTF in the CHEX. Similar to the different refrigeration systems, the MR system also generates better cooling capacity and COP as the mass flow rate of water increases. It is due to the larger convective heat transfer by the higher mass flow of the water, which is the second fluid in CHEX. Moreover, the tendency of the cooling capacity and COP is the same in Figure 2.21 (a) and (b). It is because the power consumption by the motor and pump was not affected by the heat source temperature.

In the meantime, the Carnot COP was calculated to obtain the second law of efficiency of the MR system as presented in Figure 2.22 (a). Even though the COP of the system decreases as the heat source temperature drops in Figure

2.21 (b), the second law of efficiency increases in Figure 2.22 (b). It is because the rate of decrement of the Carnot COP is higher than that of the COP as shown in Figure 2.22 (a), which leads to a larger value by (2.16). Most of all, the obtained second law of efficiency of the MR system is relatively minute in Figure 2.22 (b) compared to the references [14], [15], [94]. However, some researchers reported similar η_{2nd} from their experiments to our results [43], [82]. The large discrepancies in the second law of efficiency among researchers originated from theoretical and actual system efficiency. For example, Lozano et al. [41] compared the overall and cycle second law of efficiency. At their maximum, the overall system η_{2nd} was just 5%, but the η_{2nd} of the MR cycle itself was in the range of 30-35%. This means that inefficient heat transfer occurs between MCM and HTF or between HTF and the second fluid in CHEX. Moreover, the bidirectional flow of the HTF in the system can also diminish the η_{2nd} of the system by heating and cooling the tubes repetitively in the system.

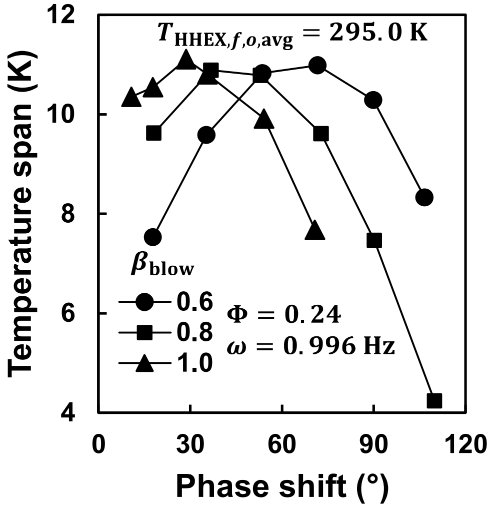

(a)

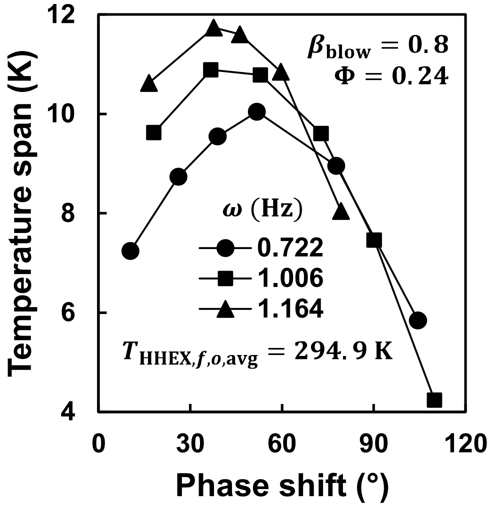

(b)

Figure 2.12 Temperature span with respect to the phase shift (a) in different blow ratio and (b) operating frequencies in no-load conditions.

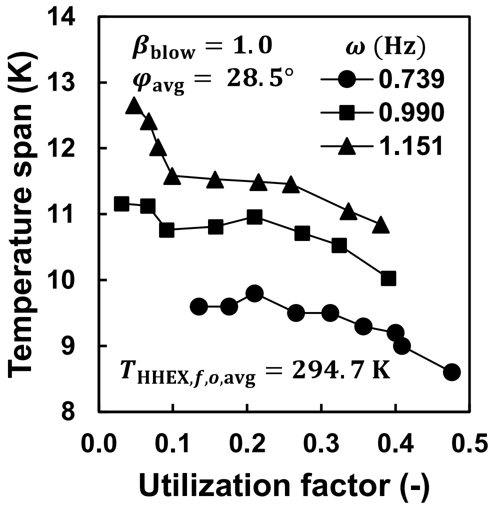

(a)

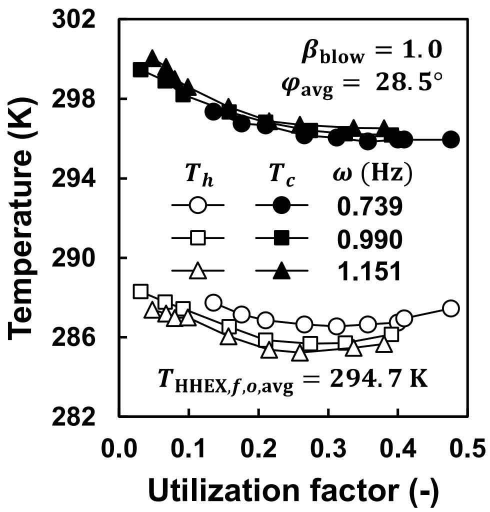

(b)

Figure 2.13 Temperature span with respect to the utilization factor (a) in different operating frequencies and (b) average hot- and cold-end temperatures of the AMRs in no-load conditions.

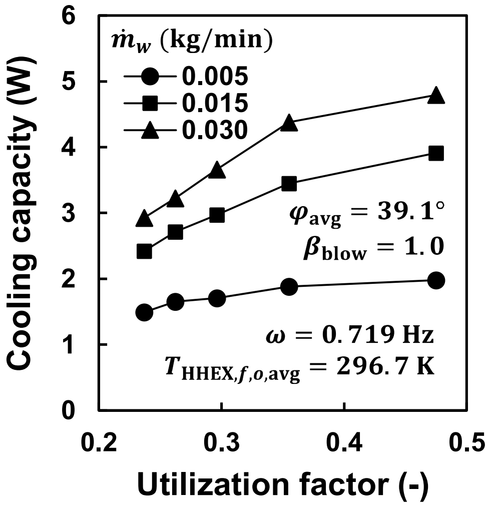

(a)

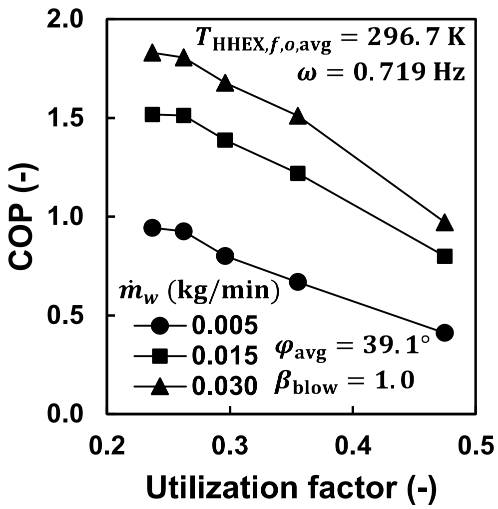

(b)

Figure 2.14 (a) Cooling capacity and (b) COP with respect to the utilization factor in different mass flow rate of the water in the CHEX in load conditions.

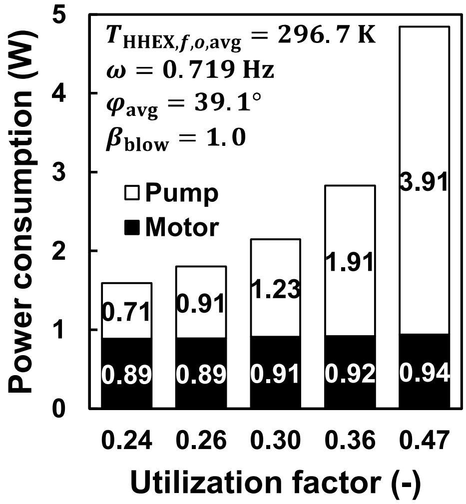

(a)

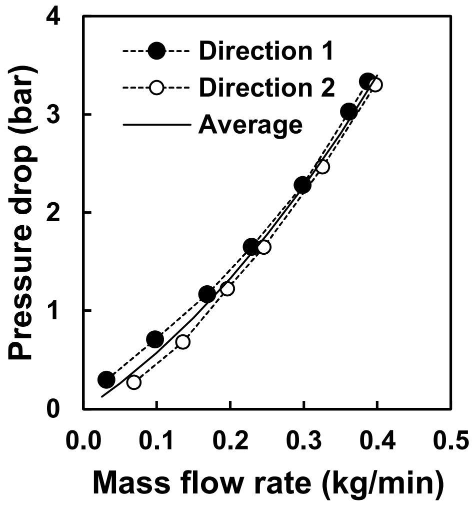

(b)

Figure 2.15 (a) Power consumption by the pump and motor in the system in different utilization factors and (b) pressure drop of the AMRs with respect to the mass flow rate of HTF.

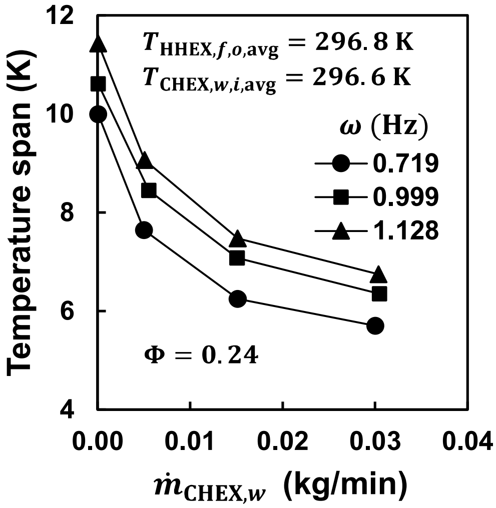

(a)

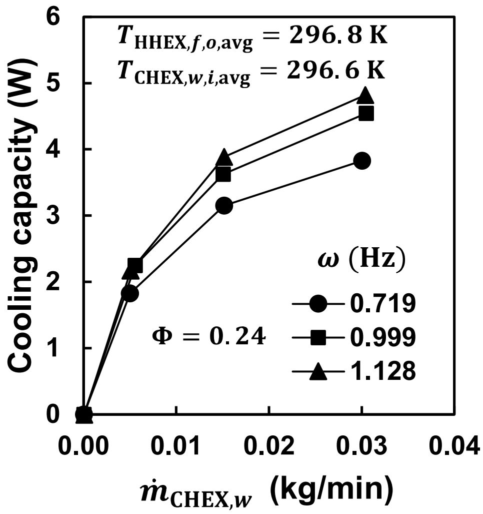

(b)

Figure 2.16 (a) Temperature span and (b) cooling capacity in different operating frequencies with respect to the mass flow rate of the water in the CHEX in load conditions.

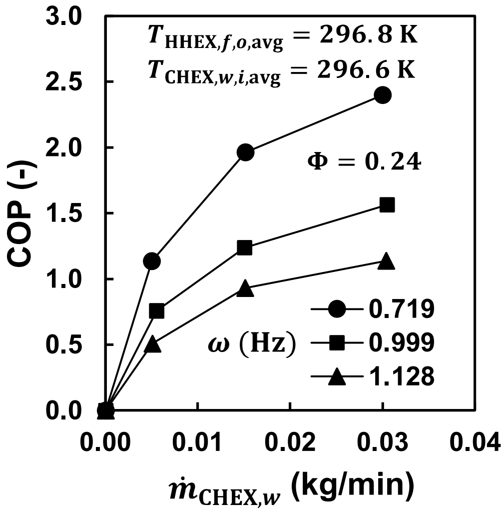

(a)

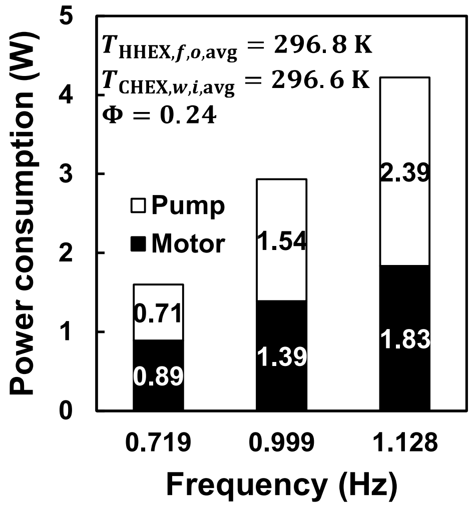

(b)

Figure 2.17 (a) COP with respect to the mass flow rate of the water in the CHEX and (b) power consumption by the pump and motor in different operating frequencies in load conditions.

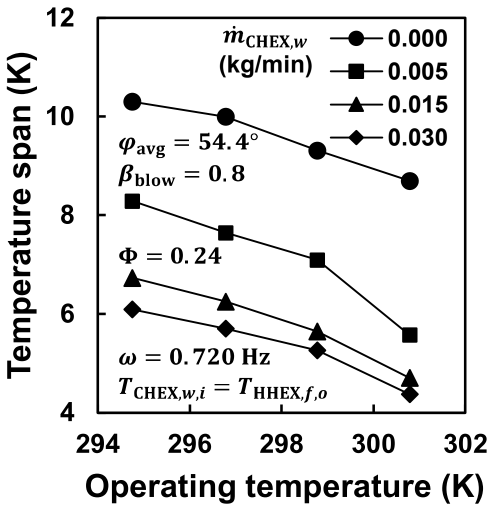

(a)

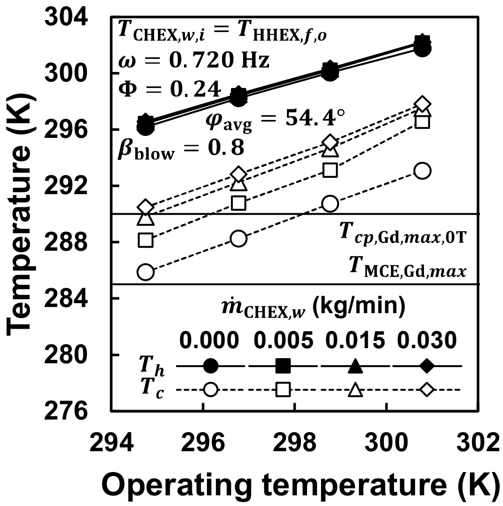

(b)

Figure 2.18 (a) Temperature span and (a) average hot- and cold-end temperatures of the AMRs with respect to operating temperautre in different mass flow rate of the water in the CHEX in load conditions.

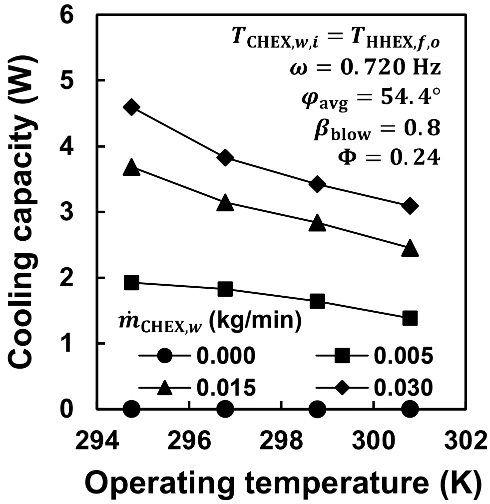

(a)

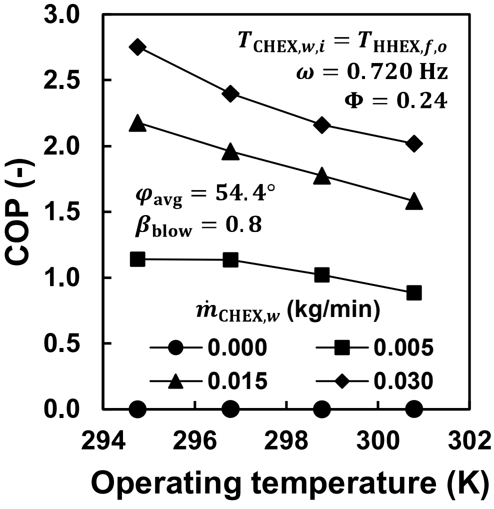

(b)

Figure 2.19 (a) Cooling capacity and (b) COP with respect to operating temperautre in different mass flow rate of the water in the CHEX in load conditions.

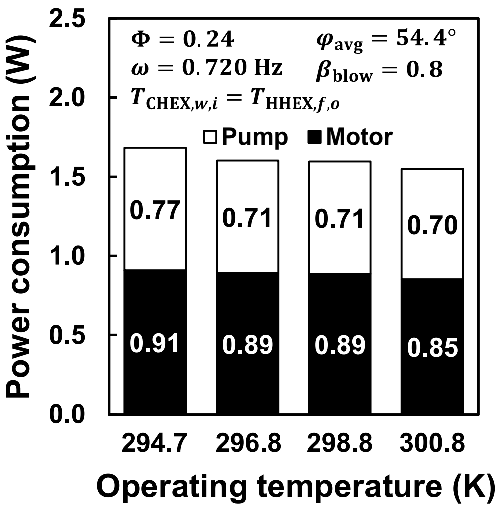

Figure 2.20 Power consumption by the pump and motor with respect to operating temperautre.

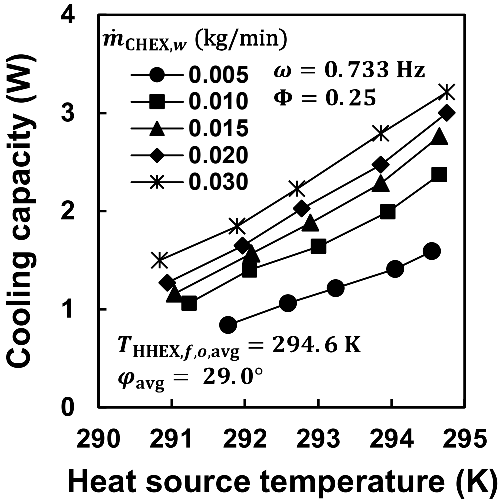

(a)

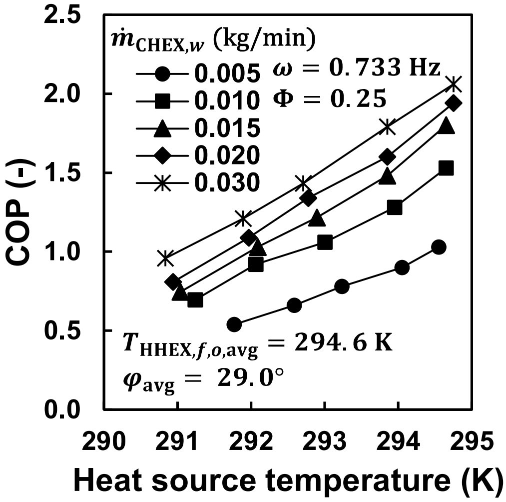

(b)

Figure 2.21 (a) Cooling capacity and (b) COP with respect to heat source temperature in different mass flow rate of the water in the CHEX in load conditions.

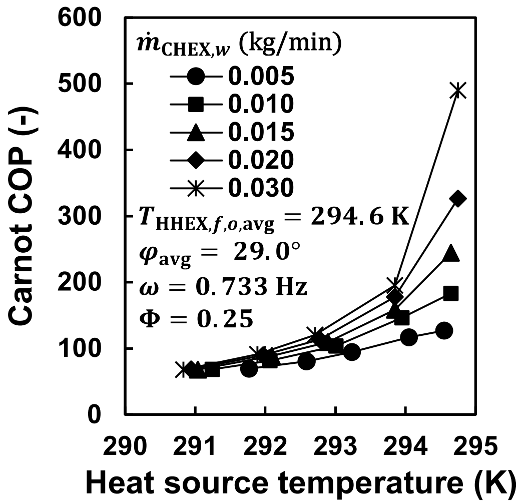

(a)

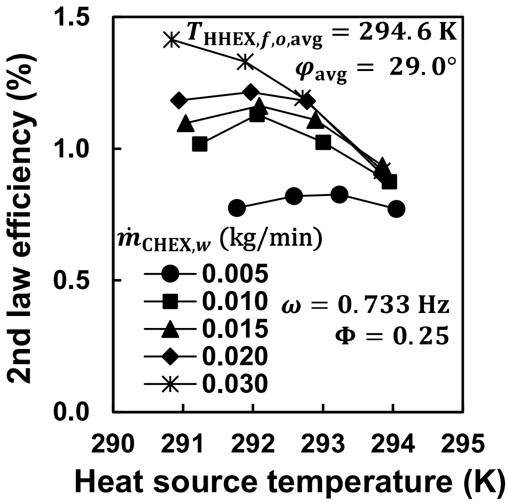

(b)

Figure 2.22 (a) Carnot COP and (b) second law of efficiency with respect to heat source temperature in different mass flow rate of the water in the CHEX in load conditions.

2.4. Summary

In this research, a variety of operating parameters were verified to investigate their effect on temperature span, cooling capacity, COP, and the second law of efficiency. First of all, the phase shifts were tested in different blow ratios and operating frequencies. It was found that the optimal phase shift becomes smaller as the blow ratio increases. Meanwhile, the optimal phase shift was maintained almost the same in different operating frequencies. In extremely low utilization factors, the temperature span was found to grow due to rising hot-end temperature. Therefore, the optimal utilization factor should be determined considering the cold-end temperature of the MR system. Therefore, the temperature span was 9.5, 10.7, and 11.5 K in the no-load condition at 0.739, 0.990, and 1.151 Hz of the operating frequency in each optimal utilization factor of 0.312, 0.274, and 0.259, where the cold-end temperature of the MR system was the lowest. Furthermore, the higher utilization factor presents an improved cooling capacity due to the larger heat capacity. However, the COP diminished due to the exponential increase in power consumption by the pump when the utilization factor is higher. This suggests that the MR system is demanded to be operated with as low a utilization factor as possible from the viewpoint of the COP. In the meantime, the higher operating frequency provided better cooling capacity but it reduces the COP due to the higher power consumption by the motor. Consequently, the maximum cooling capacity and COP were obtained during the test, which were 4.82 W at 1.128 Hz and 2.40 at 0.719 Hz, respectively. The most effective way to increase COP was securing the proper operating temperature of the MR system. It was because it least affects the power consumption by the motor and pump compared to the other operating parameters. The heat source temperature was also tested to obtain the second law of efficiency of the MR system. It was found that the maximum value of it was 1.41% due to extended dead zones in the system and inefficient heat transfer in the CHEX.

Chapter 3. COP improvement by packing arrangement in the active magnetic regenerator[1]

3.1. Introduction

According to the results from Chapter 1, power consumption by the pump exponentially rises when the utilization factor increases in Figure 2.15 (a). Moreover, when increasing frequency, the portion of the power consumption by the pump is ascending in total power consumption as seen in Figure 2.17 (b). The higher utilization factor and operating frequency are required to improve the cooling capacity of the MR system under the condition that a certain amount of COP is secured. This fact, therefore, demands a novel geometry of the AMR with Gadolinium particles which can alleviate pressure drop in MR systems.

A variety of research has been conducted to find the best geometries of MCM for the AMRs in the MR systems. Those shapes included chips (or flakes), spheres, plates, pins, wire, microchannels, and others. Although most of them were proposed for lower viscous loss by HTF, they are limited to be applied in a commercial MR system due to their brittleness and economical issue [28],

[1] The contents of chapter 3 are submitted in the Energy Conversion and Management on 2022.

[29], [30]. Therefore, flaked or sphered Gadolinium is still the best choice in MR systems with its huge heat transfer area and effectiveness [25], [26], [63]. In these circumstances, it should be introduced to reduce pressure drop through the AMRs including Gadolinium particles [13], [81], [95], [96].

3.2. Experimental method

3.2.1. Experimental setup

The irregular Gadolinium particles between the meshes with aperture sizes from 850 to 500 μm were prepared. Those were contained in an inner PTFE tube. Every four of them is serially positioned in a single stainless steel 316L tube. The random distribution of the non-aligned AMRs is shown in Figure 3.1 (a) during the packing. On the contrary, Gadolinium particles were packed in the inner tubes under the external magnetic field for the aligned AMRs to make them aligned as shown in Figure 3.1 (b). Therefore, the particles were aligned to the axial direction of the inner tube. By this procedure, each of four of the non-aligned and aligned AMRs is made in Figure 3.2. The general characteristics of each AMR are presented in Table 3.1.The magnetic field source was utilized in Figure 2.5 by adjusting the air gap to 10 mm which is described in Table 3.2. Moreover, the same experimental setup and operation method were adopted from Figure 2.7 and Figure 2.8.

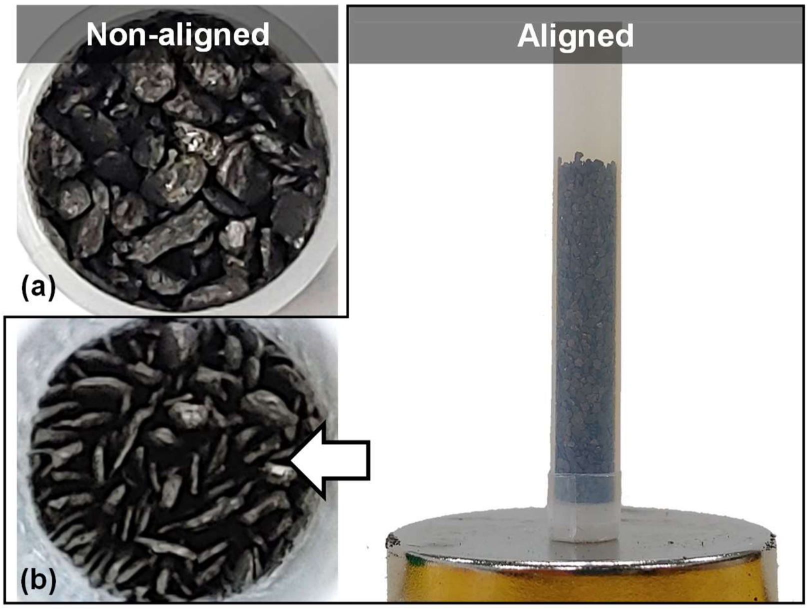

Figure 3.1 Top view of the active magnetic regenerators: (a) Non-aligned and (b) aligned AMR

Figure 3.2 Inner tubes for active magnetic regenerators.

Table 3.1 Geometric data for the non-aligned and aligned AMRs.

Parameter	Value	Unit
Housing material	SUS 316L + PTFE	-
Number of beds	4 (Parallel)	-
Inner diameter	6.0	mm
Outer diameter	9.5	mm
Total effective length	150	mm
Magnetocaloric material (MCM)	Gadolinium	-
MCM geometry	Irregular particle	-
MCM particle size	500-850	μm
MCM total mass	64.0	g
Average porosity	0.434 (non-aligned)	-
	0.415 (aligned)	-

Table 3.2 Characteristics of the magnets and the magnet assembly for the comparative study between the non-aligned and aligned AMRs.

Parameter	Value
Permanent magnet	NdFeB (N35)
Magnet geometry (width × height × length)	25 mm × 25 mm × 50 mm
Magnet assembly geometry (Magnets only, width × height × depth)	200 mm × 100 mm × 150 mm
Maximum magnetic field in air gap	0.921 T
Minimum magnetic field in air gap	0.013 T
Air gap length	10 mm

3.2.2. Test procedure

A more detailed arrangement of the particles was examined inside AMRs by X-ray computed tomography (XCT). Three samples were prepared for each non-aligned and aligned AMRs. They were scanned by using the Zeiss Xradia 620 Versa. The X-ray source voltage was set to 160 kV. The exposure time was from 12 to 20 s, and the objective magnification was 0.4. As a result, a thousand 2D cross-sectional images were taken in 1,000 and 1,024 pixels in width and height for every sample, respectively during the sample rotating in their axial direction [97], [98], [99]. The post-processing was conducted with the 2D images to rebuild the 3D model of the samples by Object Research Systems Dragonfly (version 2022.1). Therefore, the specific surface area of the AMRs can be obtained using the 3D reconstructed model, which results are tabulated in Table 3.3 [99], [100], [101].

Two types of AMRs with different arrangement method are installed between the magnetic assembly. For both cases, total pressure drops of the AMRs are measured. The correlations of the pressure drop for each case are then obtained to calculate the power consumption by pump for the refrigeration system. Moreover, the friction factors are calculated using not only the average pressure drop of each AMRs for both cases but also the geometric data of the

AMRs to compare each other. Last but not least, the performance parameters of the MR system are measured such as temperature span, cooling capacity, COP and power consumption.

Table 3.3 Specific surface area obtained by XCT results from the samples of the non-aligned and aligned AMRs.

AMR type	Sample number	Specific surface area (mm^{-1})
Non-aligned	1	12.02
	2	11.88
	3	12.42
	Average	12.11
Aligned	1	12.11
	2	12.58
	3	11.87
	Average	12.19

3.2.3. Performance parameters

The experimental parameters, such as utilization factor, temperature span, cooling capacity, COP, and power consumption by the motor (or pump), are described in chapter 2.2.3. For the calculation of the power consumption by the pump in (2.14), the total pressure drops of non-aligned and aligned AMRs with respect to the mass flow rate of the HTF was utilized. The obtained results are presented in Figure 3.3. By using the results, the correlations of average $\Delta p_{f,\mathrm{sys}}$ for non-aligned AMR,

$$\Delta p_{f,\mathrm{sys}} = 7.664\,\dot{m}_f^2 + 3.8592\,\dot{m}_f \tag{3.1}$$

and for aligned AMR

$$\Delta p_{f,\mathrm{sys}} = 5.1755\,\dot{m}_f^2 + 3.7218\,\dot{m}_f \tag{3.2}$$

is obtained in quadratic equations. These equations are utilized to find out $\dot{W}_{\mathrm{p}}$ in (2.14).

To consider the different porosity of the cases, the friction factors of both packed beds are calculated by using the next equation.

$$f = \frac{\Delta p_f}{L \rho_f U_o^2} D_p \frac{\epsilon^3}{1-\epsilon} \tag{3.3}$$

Herein, f is the friction factor, Δp_f is the pressure drop of the HTF, L is the length of the packed bed, ϵ is the porosity, and D_p is the particle diameter. In addition, U_o is the superficial velocity and ρ_f is the density of the HTF. For reference, Carman correlation is utilized to find the friction factor of the packed bed with spherical particles having equivalent spherical diameter to the irregular Gadolinium. The Carman correlations is

$$f_{Carman} = \frac{180}{\mathrm{Re}_d} + \frac{2.87}{\mathrm{Re}_d^{0.1}} \tag{3.4}$$

where the Reynolds number of the HTF in a packed bed, Re_d, is defined as below.

$$\mathrm{Re}_d = \frac{\rho_f U_o D_p}{\mu_f (1-\epsilon)} \tag{3.5}$$

where μ_f is the dynamic viscosity of the HTF. The equivalent spherical diameter of a particle is calculated by the next equation.

$$D_{S_v} = \frac{6}{S_v} \tag{3.6}$$

Herein, S_v is the specific surface area of the particle. The specific surface area is a total surface area divided by the total volume of the particles. Those values for the particles in the non-aligned and aligned AMRs are obtained by the XCT with 3-D reconstructing, which are presented in Table 3.3.

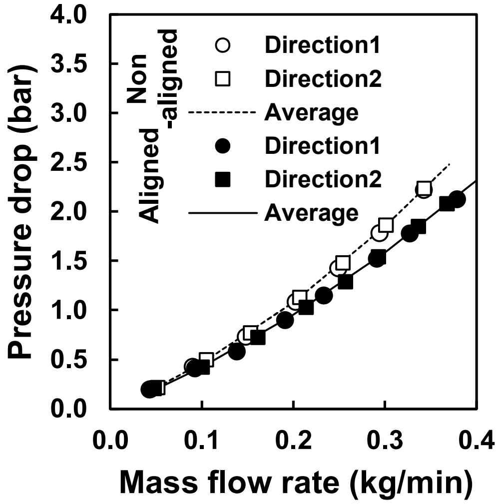

Figure 3.3 The pressure drops of the HTF measured between P1 and P2 for the mass flow rate of the HTF in the MR system. Direction 1 indicates the flow from P1 to P2 and direction 2 is the opposite way. The average values of direction 1 and 2 are indicated as well.

3.3. Results and discussion

The representative 2D images for both cases are shown in Figure 3.4. Most of the particles are slightly perpendicular to the flow direction for the non-aligned AMRs in Figure 3.4 (a). On the other hand, the particles are included in the AMR almost parallel to the flow direction in case of aligned AMR in Figure 3.4 (b). This fact implies that the pressure drop can be improved by the alignment of Gadolinium in an MR system using the external magnetic field.

The pressure drops for single AMR for both cases are presented in Figure 3.5. In most cases, the aligned AMRs have lower pressure drop than the non-aligned ones. When it comes to the mass flow rate of HTF from 0.10 to 0.35 kg/min, around 18.8% of reduction of pressure drop was obtained by using the aligned AMRs. The average pressure drops for each case in Figure 3.5 are applied to obtain friction factors in (3.3).

Figure 3.6 shows the friction factors for non-aligned, aligned AMRs. At the same time the friction factor for the AMR with particles, which have the equivalent spherical diameters to the irregular particles for the above cases. At a glance, the curve for the friction factor by the aligned AMRs is shown under the other cases. Specifically, the friction factor by the aligned AMR is 20.5% lower than by the packed bed with spheres on average. This fact elucidates that the arrangement of the irregular Gadolinium can provide less pressure drop, which is even lower than the packing only with the spheres.

Figure 3.7 presents the temperature span under the no-load condition for both cases of non-aligned and aligned AMRs according to the utilization factor. In overall, it can be said that the aligned AMRs shows better performance than the non-aligned AMRs. It is because the aligned AMRs had less porosity, which resulted in more mass of the Gadolinium positioned at the center of the magnetic assembly. The magnetic assembly was in the 3D shape so that the magnetic flux density became to be lower as it approaches the boundary of the magnetic field source, as seen in Figure 2.6. This means that the magnetic field change for the MCE of the MCM could be lower when the porosity was larger under the condition that the total mass of the MCM was identical.

Meanwhile, Figure 3.8 (a) shows the temperature span results with respect to the cooling capacity for both aligned and non-aligned cases at different operating frequency. Relatively higher temperature span was provided by the aligned AMRs at the same cooling capacity. This result is consistent to the temperature span results in the no-load condition. This is also induced by the improved porosity in the aligned AMR.

It is the most appreciable that the COP of the aligned AMRs is fairly larger than the non-aligned one in Figure 3.8 (b) when having the same cooling capacity in both cases.

To make it more clearly, cooling capacity and COP are presented in Figure 3.9 and Figure 3.10 at 3.8 and 4.5 K of temperature spans, respectively. Those cooling capacity and COP are obtained by the interpolation by the experimental data as denoted by the broken lines in Figure 3.8 (a). Firstly, the cooling capacity increases by 23.8%, 14.1% and 3.5%, respectively at 3.8 K of the temperature span in Figure 3.9 (a). However, Figure 3.9 (b) says the COP of the aligned AMRs are improved further by 27.8%, 23.1%, and 11.8% in 0.56, 0.71, and 1.00 Hz of the nominal operating frequency compared to the non-aligned ones. In addition, as shown in Figure 3.10 (a) and (b) the COP of the aligned one are also enhanced by 37.3%, 27.3%, and 10.5%, while the cooling capacity rises only by 30.6%, 12.8%, and 8.4% in each operating frequency, respectively, at 4.5 K of the temperature span. These facts say that the improvement of both the cooling capacity and total power consumption brought about better COP results in aligned AMRs.

To evaluate the power consumption for the non-aligned and aligned AMRs, Figure 3.11 is suggested. As can be seen, the power consumption by the motor is increasing as the operating frequency rises. However, they are maintained to be almost same between both cases in every operating frequency. This is due to the same total mass of the Gadolinium utilized in both cases. On contrast, the power consumption by the pump slightly reduces in 0.56 Hz of the operating frequency, but the rate of the reduction of it increases as the operating frequency rises. Specifically, lower total power consumption was obtained in case of the aligned AMRs by 3.3%, 8.1%, and 5.5%, which was mainly led by 8.9%, 16.4%, and 9.4% reduction of the power consumption by the pump by using the aligned AMRs in 0.56, 0.71, and 1.00 Hz of the nominal operating frequency, respectively. This is firstly because of the less $\Delta p_{f,\mathrm{sys}}$ in (2.14) in the case of the aligned AMRs at the same mass flow rate of the HTF as seen in Figure 3.3. Furthermore, as the operating frequency increases, the $\dot{m}_f$ also grows, which leads to higher $\Delta p_{f,\mathrm{sys}}$ in bigger operating frequency. Therefore, the rate of the reduction of the power consumption by the pump improves at higher operating frequency.

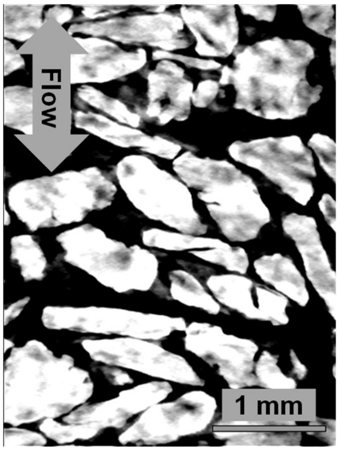

(a)

(b)

Figure 3.4 The particles of Gadolinium inside the (a) non-aligned and (b) aligned AMRs obtained from the X-ray computed tomography

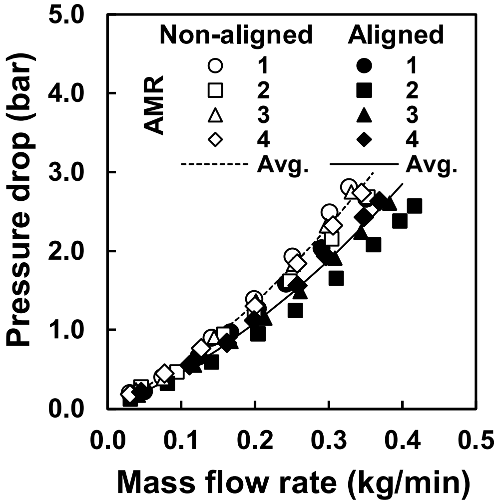

Figure 3.5 Pressure drop in the non-aligned and aligned AMRs with respect to the mass flow rate of the HTF. The solid and dotted lines indicate the average values.

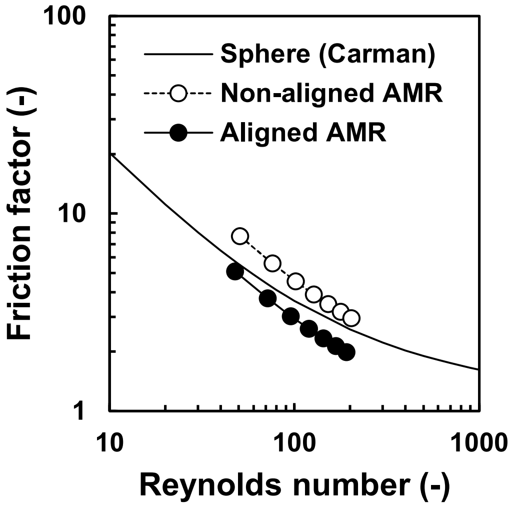

Figure 3.6 The friction factor of non-aligned and aligned AMRs with irregular Gadolinium. The solid line indicates the friction factor of the packed bed with sphere particles by Carman correlation. The spheres was assumet to have an equivalent particle diameter.

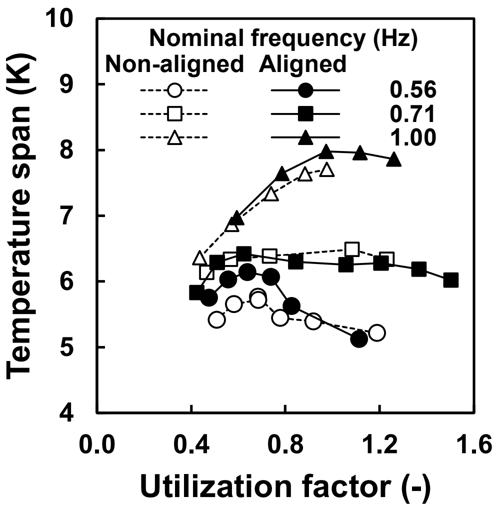

Figure 3.7 Temperature span from the non-aligned and aligned AMRs with respect to utilization factor in different operating frequencies in no-load conditions.

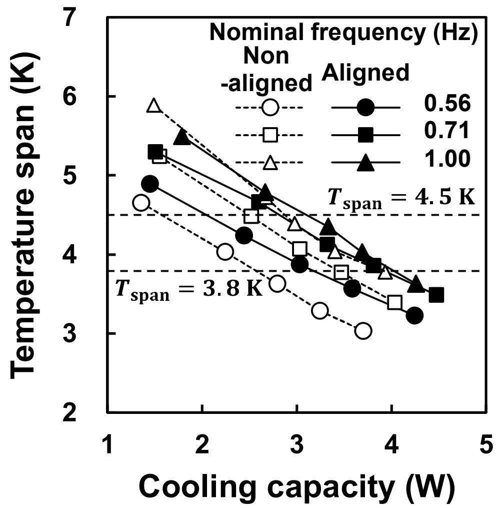

(a)

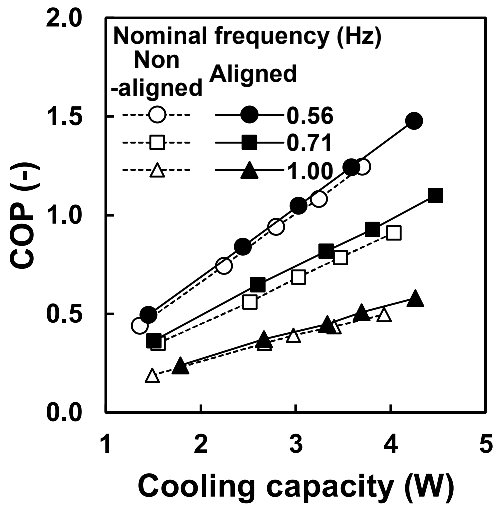

(b)

Figure 3.8 Temperature span and COP of the non-aligned and aligned AMRs with respect to cooling capacity in different nominal operating frequencies at load condition.

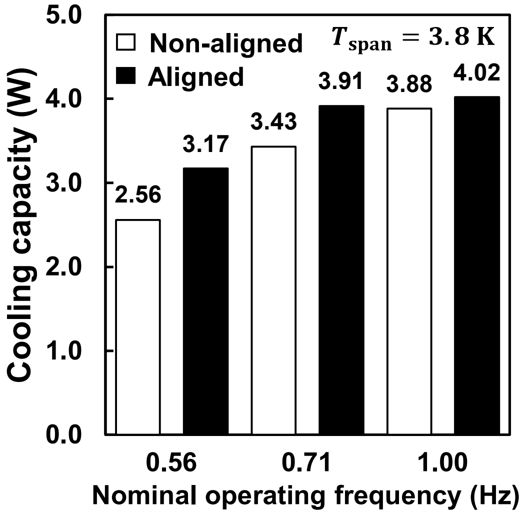

(a)

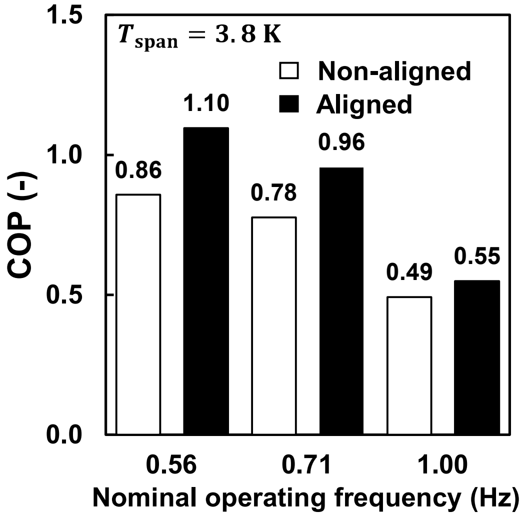

(b)

Figure 3.9 Cooling capacity and COP of the non-aligned and aligned AMRs at 3.8 K of temperature span in different nominal operating frequencies in load condition.

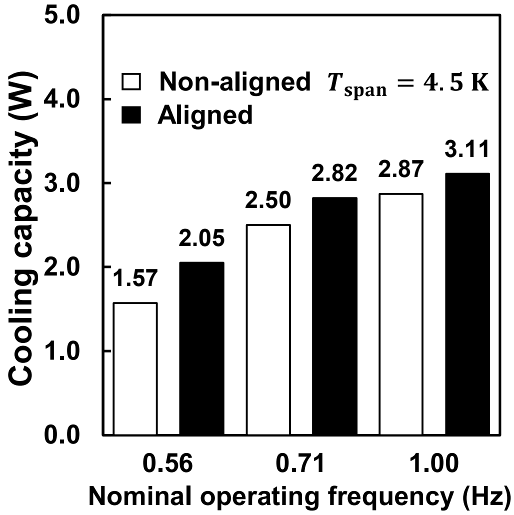

(a)

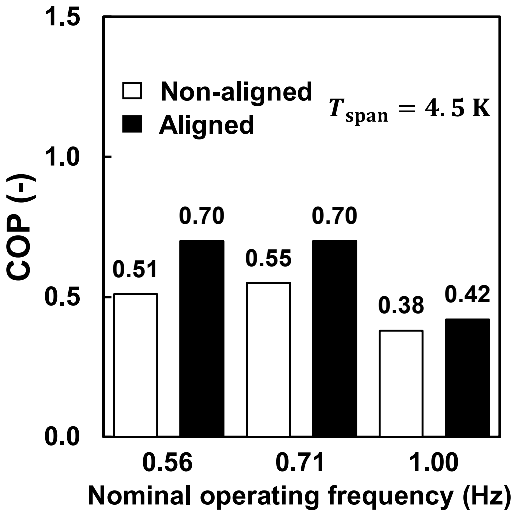

(b)

Figure 3.10 Cooling capacity and COP of the non-aligned and aligned AMRs at 4.5 K of temperature span in different nominal operating frequencies in load condition.

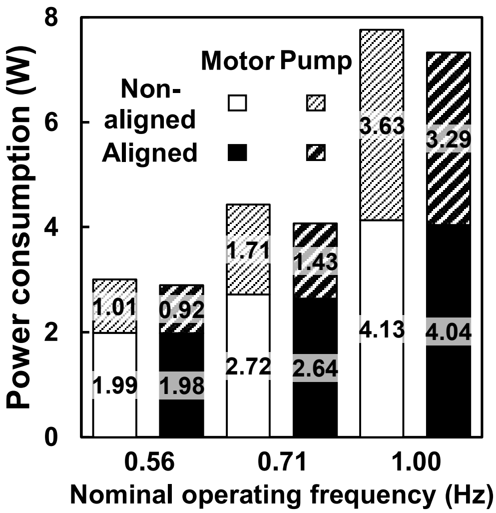

Figure 3.11 Power consumption by the motor and pump from the non-aligned and aligned AMRs in different nominal operating frequencies in the load tests.

3.4. Summary

The performance of both the AMRs with non-aligned and aligned irregular Gadolinium particles are compared in the MR system. First of all, XCT results said that the Gadolinium particles were packed in parallel to the flow direction for the aligned one, but they were in random distribution for the non-aligned one. The friction factor for the aligned AMRs was 35.9% lower, and it led to an 18.8% reduction of the pressure drop, compared to the non-aligned one. There was a slight improvement in temperature span in no-load condition, and cooling capacity in load condition by using the aligned AMRs. However, it shows a significantly higher COP than the non-aligned AMRs. Specifically, 27.8%, 23.1%, and 11.8% of COP improvement were observed at 3.8 K of the temperature span in load condition. Moreover, 37.3%, 27.3%, and 10.5% higher COP were obtained at 4.5 K of the temperature span by using the aligned AMRs in the MR system for 0.56, 0.71, and 1.00 Hz of the nominal operating frequencies. These were mainly due to the reduction of the pressure drop which was 8.9%, 16.4%, and 9.4% on average at each nominal operating frequency by the aligned AMRs.

Chapter 4. A numerical model for thermal analysis of the magnetic refrigeration system using a modified dispersion-concentric model

4.1. Introduction

So far, various numerical models were developed to investigate MR systems or AMRs. When considering the AMR with the particles of MCMs, the Nusselt number correlation for a packed bed by Wakao and Kagei [62] is widely adopted [57], [63], [64], [65]. However, it is important that the energy equation should match the convective heat transfer coefficient unless other modifications are not conducted. In typical experiments for the convective heat transfer coefficient, researchers make advantage of Newton's law of cooling to calculate the coefficient by detecting the temperature of the solid. In contrast, the convective heat transfer coefficient in a packed bed is estimated from one of the energy equations by using the temperature of the fluid phase at the inlet and outlet of the packed bed [102], [103], [104]. If the correct energy equation was not used when applying the Nusselt number correlation, some factors could be underestimated. Moreover, the reciprocating flow of the HTF heats up and cools down the tubes in one cycle in the MR system. This means that the heat transfer from tubes is an intrinsic cooling load, which also has to be considered during the numerical analysis. However, few pieces of research dealt with it by simplified geometries [53].

In this chapter, the numerical model for the MR system is suggested. Most of all, the modified dispersion-concentric (DC) model was applied as the energy equation for the packed beds of AMRs. It is because this is the only energy equation for the Nusselt number correlation by Wakao and Kagei [62]. Furthermore, tubes surrounding the HTF in the MR system is considered. In this way, the intrinsic cooling load by a bidirectional flow of the HTF can be applied during the calculation. Finally, the simulation is validated with the experimental results.

4.2. Numerical model

4.2.1. Active magnetic regenerator modeling

The mass balance of the packed bed in the time domain, t, is expressed as below.

$$\frac{\partial \rho}{\partial t} + \nabla \cdot \rho u = 0 \tag{4.1}$$

The density of the fluid, ρ, is assumed to be constant for the incompressible pipe flow in a circular tube. At the inlet of the packed bed, the vector, u, is the flow velocity for the packed bed. In addition, we assume the flow is parallel to the wall ($u_r = u_\theta = 0$) so that the equation becomes as below.

$$\frac{\partial u_x}{\partial x} = 0 \tag{4.2}$$

Herein, x is the axial distance. If the flow is steady, axisymmetric, and uniformly distributed to the cross-sectional area, the axial velocity, u_x, is uniform flow, or simply called the superficial flow for the packed bed. Meanwhile, by using the volumetric flow rate, $\dot{V}$, for the packed bed, u_x is also expressed as

$$u_x = \frac{\dot{V}}{A_c} \tag{4.3}$$

where A_c is a cross-sectional area at the inlet of the packed bed [105].

In a packed bed, Darcy's law was used for the momentum equation to find out the pressure drop through it. The equation was empirically obtained but also can be derived from the Navier-Stokes equation [106]. For one-direction flow at steady-state in the medium, Darcy's law is expressed below.

$$u_x = -\frac{K}{\mu}\frac{\Delta p}{L} \tag{4.4}$$

where K is the permeability of the packed bed, μ is the dynamic viscosity of the fluid, Δp is the pressure drop in the axial direction by the laminar flow in the packed bed, and L is the total length of the packed bed [107], [108]. In the meantime, the Ergun equation was used to predict pressure drop through a packed bed in a large range of Reynolds numbers including form drag [109].

$$\frac{\Delta p \rho}{G^2}\frac{D_p}{L}\frac{\epsilon^3}{1-\epsilon} = 150\frac{\mu(1-\epsilon)}{\rho u D_p} + 1.75 \tag{4.5}$$

Herein, G is the mass flux of the fluid, ϵ is the porosity of the packed bed, and D_p is the particle diameter. The Ergun equation covers the laminar-turbulent transition region which is the operating range in this research. Moreover, it is a superposition of the Blake-Kozeny equation for laminar and the Burke-Plummer equation for turbulent flow [110]

In porous media, the modified dispersion-concentric (DC) model was applied for thermal analysis between the solid and fluid phases. The DC model is defined below including the heat flux from the tube wall and MCE as a source term.

$$\frac{\partial T_f}{\partial t} = \alpha_{ax}\frac{\partial^2 T_f}{\partial x^2} - U\frac{\partial T_f}{\partial x} - \frac{h_s(1-\epsilon)S_v}{\epsilon c_{p,f}\rho_f}\left(T_f - T_s\right) + \frac{q_{wall}}{C_f} \tag{4.6}$$

$$\frac{\partial T_s}{\partial t} = \alpha_s \frac{1}{r^2}\frac{\partial}{\partial r}\left(r^2 \frac{\partial T_s}{\partial r}\right) + \frac{\dot{Q}_{MCE}}{C_s} \tag{4.7}$$

Herein, each subscript, f, and s, means fluid and solid phase in the packed bed and $wall$ designates tube wall. Furthermore, T is temperature, α_{ax} is axial fluid thermal dispersion coefficient, U is the interstitial velocity of the fluid, h_s is the heat transfer coefficient between the solid and fluid phase, q_{wall} is the heat transfer rate from the wall to the fluid, C_f is the thermal capacity of the fluid, $c_{p,f}$ is the specific heat of the fluid phase at constant pressure. Moreover, α_s is solid thermal diffusivity, and r is the radial distance from the center of the solid particle, C_s is the thermal capacity of the solid, and $\dot{Q}_{MCE}$ is heat source by MCE.

The representative nodal domains for both fluid and solid phases are described in Figure 4.1 (a) and (b), respectively. In the numerical calculation, the differential equation for the fluid phase from the DC model was discretized for the nth node as below.

$$\frac{T_{f,n}^{p+1}-T_{f,n}^{p}}{\Delta t}=\alpha_{ax,n}^{p}\frac{\left(T_{f,n+1}^{p}+T_{f,n-1}^{p}-2T_{f,n}^{p}\right)}{(\Delta x)^2}-U^{p}\frac{T_{f,n+1}^{p}-T_{f,n-1}^{p}}{2\Delta x}$$
$$-\frac{h_{s,n}^{p}(1-\epsilon)S_v}{\epsilon c_{p,f,n}^{p}\rho_{f,n}^{p}}\left(T_{f,n}^{p}-T_{s,n,M}^{p}\right)+\frac{q_{wall,n}^{p}}{C_{f,n}^{p}} \tag{4.8}$$

$T_f = T_{\mathrm{HHEX},f,o}\ at\ n = 0$ and N

For the time derivative, the explicit method was used to obtain the fluid temperature at the next time, $p+1$ with the properties at the previous time, p. In addition, the central difference method was applied to the spatial derivatives. The differential equation for the solid particle was also discretized for the inner nodes with the same numerical schemes as following.

$$\frac{T_{s,n,m}^{p+1}-T_{s,n,m}^{p}}{\Delta t}=\alpha_{s,n,m}^{p}\left\{\frac{2}{(m-1)\Delta r}\frac{T_{s,n,m+1}^{p}-T_{s,n,m-1}^{p}}{2\Delta r}\right.$$
$$\left.+\frac{\left(T_{s,n,m+1}^{p}+T_{s,n,m-1}^{p}-2T_{s,n,m}^{p}\right)}{(\Delta r)^2}\right\} \tag{4.9}$$
$$+\frac{\dot{Q}_{MCE}^{p}}{C_{s,n,m}^{p}}\ (2\leq m\leq \mathrm{M}-1)$$

In the central node, energy conservation law was applied:

$$\rho_{s,n,m}c_{p,s,m}V_{s,n,m}\frac{\partial T_{s,n,m}}{\partial t}$$
$$=k_{s,n,m}A_{s,m,m+1}\frac{T_{s,n,m+1}-T_{s,n,m}}{\Delta r}+\dot{Q}_{\mathrm{MCE}} \tag{4.10}$$

Likewise, the unsteady heat transfer in the volume of the boundary nodes is expressed below:

$$\rho_{s,n,m} c_{p,s,m} V_{s,n,m} \frac{\partial T_{s,n,m}}{\partial t} = k_{s,n,m} A_{s,m-1,m} \frac{T_{s,n,m-1} - T_{s,n,m}}{\Delta r} + \hbar_{s,n} A_{s,m} \left(T_{f,n} - T_{s,n,m} \right) + \dot{Q}_{\mathrm{MCE}} \tag{4.11}$$

Both the equations for the central and boundary nodes above are discretized as follows.

$$\rho_{s,n,m}^{p} c_{p,s,m}^{p} \left\{ \frac{4}{3}\pi \left(\frac{\Delta r}{2} \right)^3 \right\} \frac{T_m^{p+1} - T_m^{p}}{\Delta t} = k_{s,n,m}^{p} \left\{ 4\pi \left(\frac{\Delta r}{2} \right)^2 \right\} \frac{T_{s,n,m+1}^{p} - T_{s,n,m}^{p}}{\Delta r} + \dot{Q}_{MCE}^{p} \; (m = 1) \tag{4.12}$$

$$\rho_{s,n,m}^{p} c_{p,s,m}^{p} \left[\frac{4}{3}\pi \left[\{(m-1)\Delta r\}^3 - \left\{ \left(m - \frac{3}{2} \right) \Delta r \right\}^3 \right] \right] \frac{T_{s,n,m}^{p+1} - T_{s.n,m}^{p}}{\Delta t} = k_{s,n,m}^{p} \left[4\pi \left\{ \left(m - \frac{3}{2} \right) \Delta r \right\}^2 \right] \frac{T_{s,n,m-1}^{p} - T_{s,n,m}^{p}}{\Delta r} + \hbar_{s,n}^{p} [4\pi \{(m-1)\Delta r\}^2] \left(T_{f,n}^{p} - T_{s,n,m}^{p} \right) + \dot{Q}_{MCE}^{p} \; (m = M) \tag{4.13}$$

The source term by the MCE at time p, $\dot{Q}_{MCE}^{p}$, is defined as following assuming the MCE under the adiabatic process.

$$\dot{Q}_{MCE}^{p} = \rho_s^{p} c_{p,s}^{p} V_s^{p} \frac{dT_{ad,MCE,s}^{p}}{dt} \cong \rho_s^{p} c_{p,s}^{p} V_s^{p} \frac{\Delta T_{ad,MCE,s}^{p}}{\Delta t} \tag{4.14}$$

The adiabatic temperature change of the solid by MCE, $\Delta T^{p}_{ad,MCE,s}$, was obtained by experimental data using material properties at time p from Cadena [111].

For the axial thermal dispersion term in (4.6), the correlation below was applied.

$$\frac{\alpha_{ax}}{\alpha_f} = \frac{1}{\epsilon}\left(\frac{k_e^o}{k_f} + 0.5\mathrm{Pr}_f\mathrm{Re}_f\right) \tag{4.15}$$

The above correlation was deduced from the porous media thermal response experiment by Gunn and De Souza [112]. From the correlation, the effective thermal conductivity of a quiescent bed, k_e^o, can be obtained below.

$$\frac{k_e^o}{k_f} = \left(\frac{k_s}{k_f}\right)^n \tag{4.16}$$

Herein, n is expressed as

$$n = 0.280 - 0.757\, log_{10}\, \epsilon - 0.057\, log_{10}\left(\frac{k_s}{k_f}\right) \tag{4.17}$$

It should be noticed that (4.16) is one of the numerous models for the effective thermal conductivity of a quiescent bed [113].

For the interstitial convective heat transfer coefficient between the solid and the fluid phase, Nusselt number correlation by Wakao and Kagei [62] was applied as below.

$$\mathrm{Nu}_f = 2 + 1.1\, \mathrm{Pr}_f^{\frac{1}{3}}\, \mathrm{Re}_f^{0.6} \tag{4.18}$$

The most significant reason the correlation was adopted is that it is based on the modified DC model energy equation.

Meanwhile, the shape factor was introduced in the Nusselt number correlation to compensate for the irregularity of the interior particles in the packed bed porous media. According to Gamson [114], the inverse shape factor is applied to the modified Reynolds number, which results in attenuated mass transfer j factor, j_d. This factor, and besides, relates to the heat transfer j factor, j_h, having the analogy as below.

$$\frac{j_h}{j_d} = 1.076 \tag{4.19}$$

In other words, the shape factor reduces the heat transfer j factor, considering overlapped contact areas where interstitial convective heat transfer between the fluid and the solid phase does not occur. Therefore, in the same manner, shape factor was multiplied on the Nusselt number obtained by the (4.18).

$$Re_f = \frac{D_p G_f}{\mu_f} \tag{4.20}$$

Herein, particle diameter, D_p, is defined in (3.6).

$$D_p = \frac{6}{S_v} \tag{4.21}$$

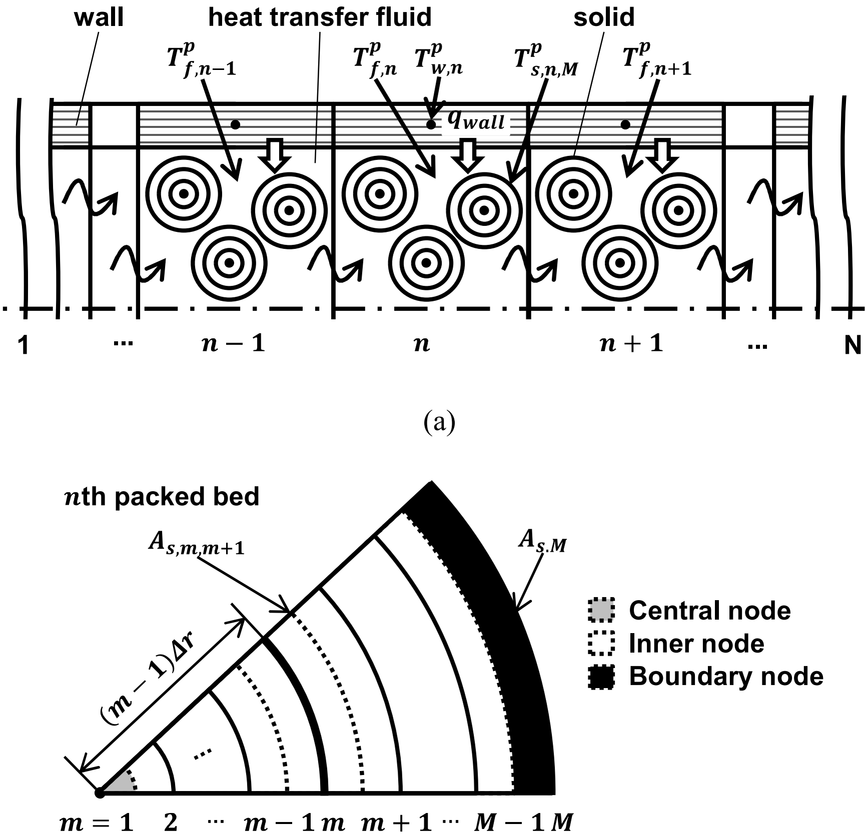

(b)

Figure 4.1 Schematic diagram of the fluid and solid phase in a packed bed: (a) Fluid phase in an AMR including solid particles and (b) one of the solid particles in an AMR.

4.2.2. Auxiliary parts modeling

Figure 4.3 shows the entire nodal domain for numerical analysis of auxiliary parts. Solid and fluid parts denoted in black and white in Figure 4.3 are auxiliary parts in this research. Thermal analysis in the parts was conducted using lumped parameter thermal modeling. Figure 4.4 - Figure 4.6 illustrate thermal resistance in the case of solid, fluid, and insulation layer, including thermal conductivity and heat transfer coefficient, respectively. The thermal resistances in each direction are calculated as follows.

$$R_{t,x}(r,x) = \frac{\frac{\Delta l_{x-1}}{2}}{k(r,x-1)A_x(r,x)} + \frac{\frac{\Delta l_x}{2}}{k(r,x)A_x(r,x)} + \frac{1}{h_x(r,x)A_x(r,x)} \tag{4.22}$$

$$R_{t,x}(r,x+1) = \frac{\frac{\Delta l_x}{2}}{k(r,x)A_x(r,x+1)} + \frac{\frac{\Delta l_{x+1}}{2}}{k(r,x+1)A_x(r,x+1)} + \frac{1}{h_x(r,x+1)A_x(r,x+1)} \tag{4.23}$$

$$R_{t,r}(r,x) = \frac{\frac{\Delta l_{r-1}}{2}}{k(r-1,x)A_r(r,x)} + \frac{\frac{\Delta l_r}{2}}{k(r,x)A_r(r,x)} + \frac{1}{h_r(r,x)A_r(r,x)} \tag{4.24}$$

$$R_{t,r}(r+1,x) = \frac{\frac{\Delta l_r}{2}}{k(r,x)A_r(r+1,x)} + \frac{\frac{\Delta l_{r+1}}{2}}{k(r+1,x)A_r(r+1,x)} + \frac{1}{h_r(r+1,x)A_r(r+1,x)} \tag{4.25}$$

Nusselt number between tube wall and fluid was obtained by assuming constant wall temperature in laminar flow.

$$\mathrm{Nu}_f = 3.66 \tag{4.26}$$

For turbulent flow, the correlation from Gnielinski [56] was applied.

$$\mathrm{Nu}_f = \frac{\left(\frac{f}{8}\right)\left(\mathrm{Re}_f - 1000\right)\mathrm{Pr}_f}{1 + 12.7\left(\frac{f}{8}\right)^{\frac{1}{2}}\left(\mathrm{Pr}^{\frac{2}{3}} - 1\right)} \tag{4.27}$$

Therefore, the heat transfer coefficient, h_r, calculated by

$$h_r(r,x) = \frac{k_f \mathrm{Nu}_f}{D_{hydraulic}} \tag{4.28}$$

where, k_f is the thermal conductivity of the fluid contact with the tube wall, and $D_{hydrauli}$ is the hydraulic diameter of the tube where the fluid flows. In this research, h_x is neglected due to the small contact area between the fluid and the tube wall in the x-direction compared to the r-direction.

Using the value obtained by the (4.22) - (4.25), heat transfer from each direction is calculated as below.

$$q_x(r,x) = \frac{T(r,x-1) - T(r,x)}{R_{t,x}(r,x)} \tag{4.29}$$

$$q_x(r,x+1) = \frac{T(r,x+1) - T(r,x)}{R_{t,x}(r,x+1)} \tag{4.30}$$

$$q_r(r+1,x) = \frac{T(r+1,x) - T(r,x)}{R_{t,r}(r+1,x)} \tag{4.31}$$

$$q_r(r,x) = \frac{T(r-1,x) - T(r,x)}{R_{t,r}(r,x)} \tag{4.32}$$

The temperature change of the tube wall is then calculated by energy conservation law to the volume of the node, $V(r,x)$, as follows.

$$\rho(r,x)V(r,x)c_p(r,x)\frac{\partial T(r,x)}{\partial t} = q_x(r,x) + q_x(r,x+1) + q_r(r+1,x) + q_r(r,x) \tag{4.33}$$

where, $\rho(r,x)$ is the density, and $c_p(r,x)$ is the specific heat of the node. The above equation is discretized by the explicit method.

$$\rho(r,x)V(r,x)c_p(r,x)\frac{T^{p+1}(r,x) - T^p(r,x)}{\Delta t} = q_x(r,x) + q_x(r,x+1) + q_r(r+1,x) + q_r(r,x) \tag{4.34}$$

To combine the AMR modeling and auxiliary parts modeling, temperature and heat transfer data calculated by each modeling were coupled during numerical analysis.

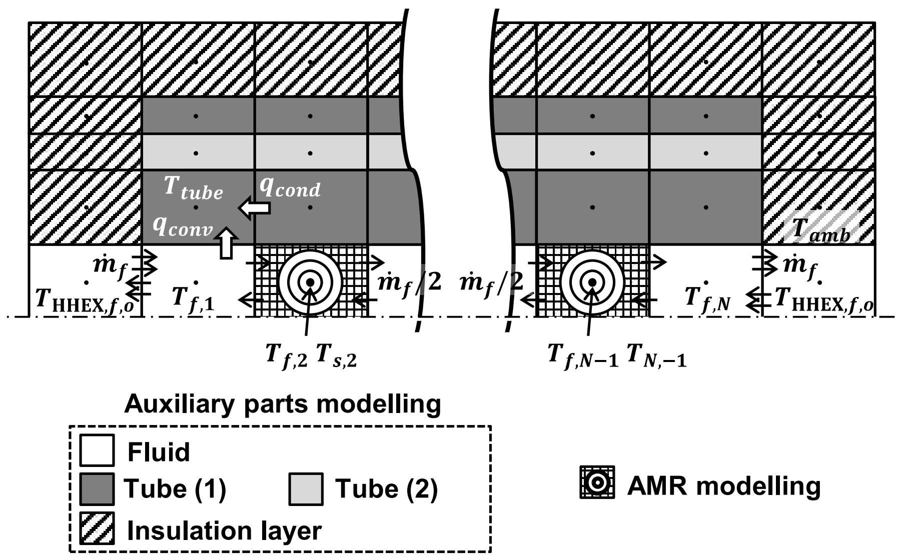

Figure 4.2 Shematic diagram of the auxiliary parts modeling including temperature nodes and mass flow rate of HTF.

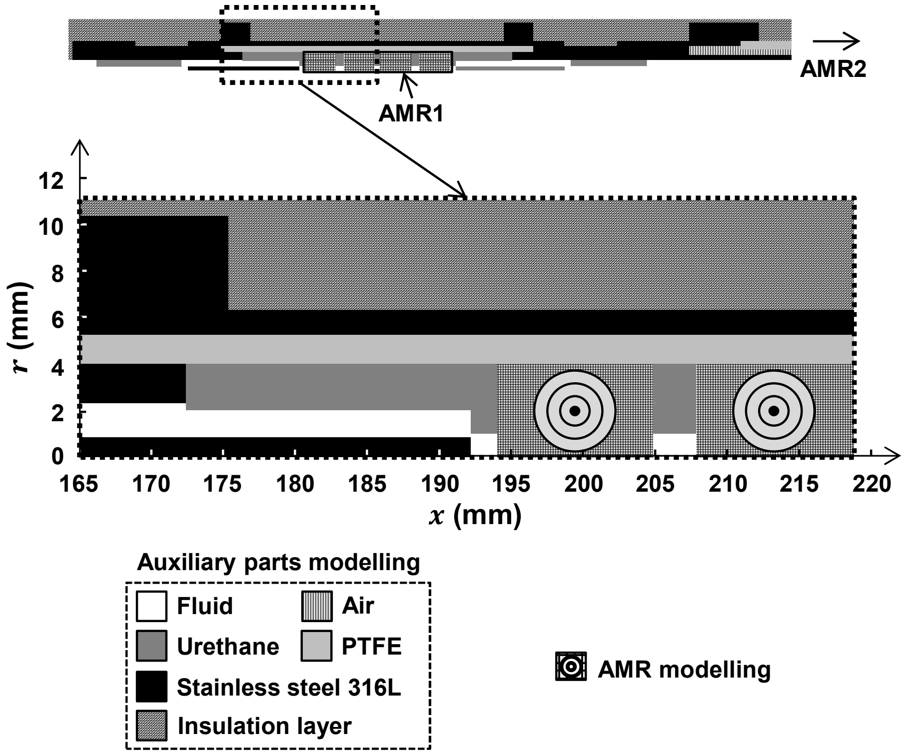

Figure 4.3 Shematic diagram of the auxiliary parts modeling around the position of the AMR1.

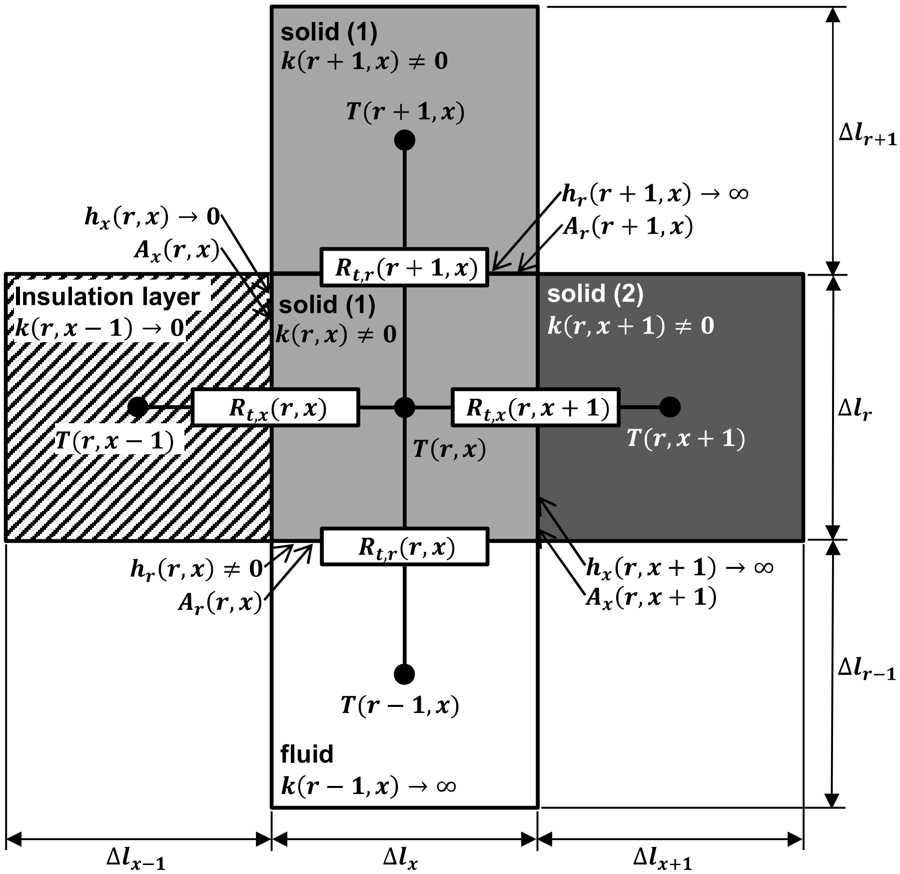

Figure 4.4 Thermal resistance circuit for a solid in the auxiliary parts modeling.

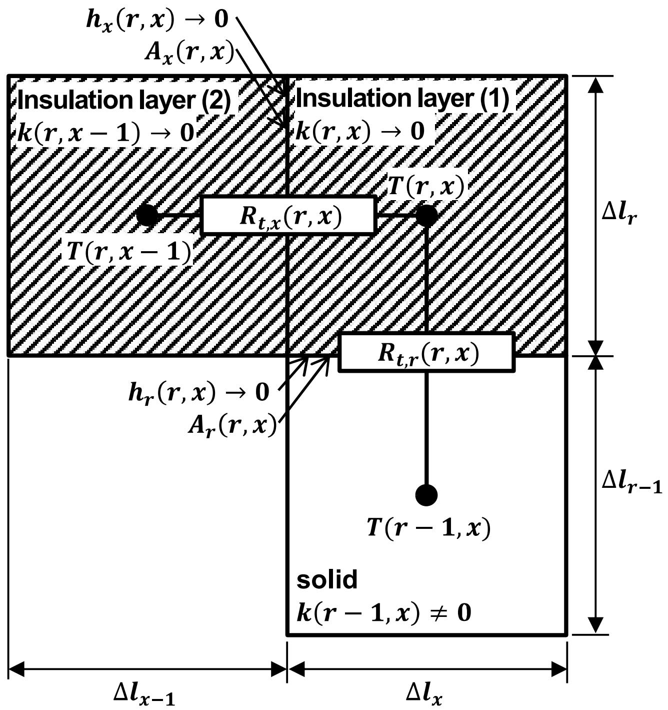

Figure 4.5 Thermal resistance circuit for an insulation layer in the auxiliary parts modeling.

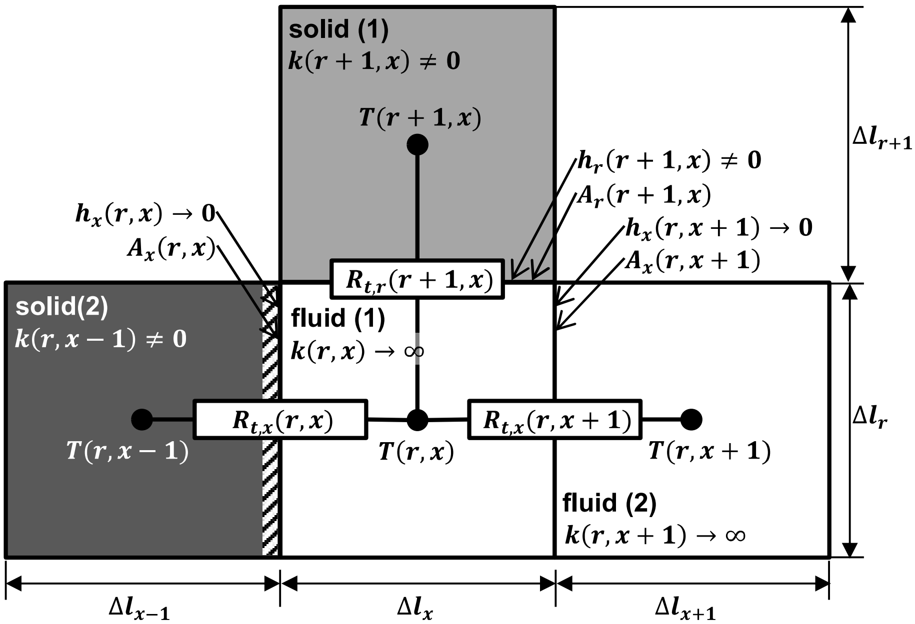

Figure 4.6 Thermal resistance circuit for fluid in the auxiliary parts modeling.

4.2.3. Test procedure

The numerical method was validated with experimental results from Chapter 2. The assumptions for the simulation are follows: Quasi-steady state condition;

Magnetic hysteresis of MCM is negligible (MCE is reversible process);

Incompressible flow; axial heat convection is neglected (small heat transfer area compared to the radial convection);

Uniform flow;

Homogeneous packed bed;

Constant temperature at the inlet;

Tubes except for the AMRs are insulated completely.

In this validation, the solid phase in a packed bed was assumed to be a singled node to facilitate the calculation. Time step was 0.0017s. The portion of the diameter of the AMR where only the MCM was included were considered as 0.341. Magnetic field was applied to the AMRs which were gradually increasing or decreasing according to the relative position between the magnets and the AMRs.

The first experimental results were conducted in 0.736 Hz. The Utilization factor was 0.243 during the tests. Moreover, the blow ratio and phase shift were controlled to be 1.0 and 29.1°, respectively. The operating temperature was

294.6 K. The shaped factor was 0.86 to consider the irregularity of the Gadolinium particles. As suggested in chapter 2, the size range of the Gadolinium was in 500 to 800 μm.

4.3. Results and discussion

Figure 4.7 (a) and Figure 4.8 shows the comparison between the simulation and experimental results. Both the cases with different frequency and utilization factor follow the tendency of the hot- and cold-end temperature from the experiments. However, there are several disagreements between the simulation and experiments.

First of all, the abrupt change of the temperatures appears well in both the experiment and simulation at the begging. However, the cold-end temperature shows more dropping in the simulation compared to the experiments. It was due to the lower heat capacity of the MR system in the simulation.

Meanwhile, the hot-end temperature of the experiment seems to maintain and approach a certain temperature. However, the hot-end temperature from the simulation decreases after the highest value at around 15 minutes in Figure 4.7 (a). In the experiment, there were T-connection for the inlet and outlet of the bidirectional flow where the mixing of the cold fluid from the HHEX and hot fluid from the hot-end of the AMRs can occur. However, the T-connection was reproduced as a straight line with the same volume in the simulation. This difference was anticipated to decrease the temperature of the fluid which flows into the hot-end of the AMR. This tendency is also found in Figure 4.8, but the significant increase in the hot-end temperature hardly appears in the middle of the time. It is because the large heat capacity from the high utilization factor in Figure 4.8 diminishes this effect.

It is also found that the cold-end temperature in the simulation keeps decreasing at the end of the simulation in both cases. It is because the complex fittings in the pipes were neglected during the simulation. This resulted in a lower cooling load in the simulation compared to the actual system. Moreover, fittings were assumed to be a single solid tube in the simulation. This means that the thermal resistance by the contact region was neglected. This led to higher heat transfer can occur between the tubes and the HTF which reduced the intrinsic load of the MR systems. Therefore, the lower temperature at the cold-end occurs in the simulation.

In addition, it can be verified by the simulation whether the hot- and cold-end temperatures measured by the fluid close to the AMR are similar to the temperature of the solid MCM. Figure 4.7 (b) shows the simulation result to compare them. First of all, the temperatures of the MCM fluctuate more than the fluid due to the MCE. Meanwhile, the temperatures of the fluid keep the average temperatures of the solid MCM. This result shows that the measured temperatures by the fluid at the hot- and cold-end of the AMR can evaluate the actual solid temperature of the MCM on average.

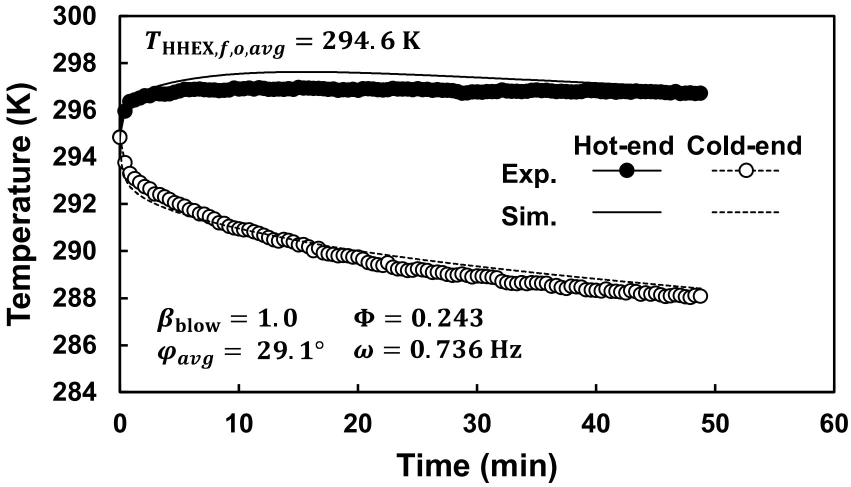

(a)

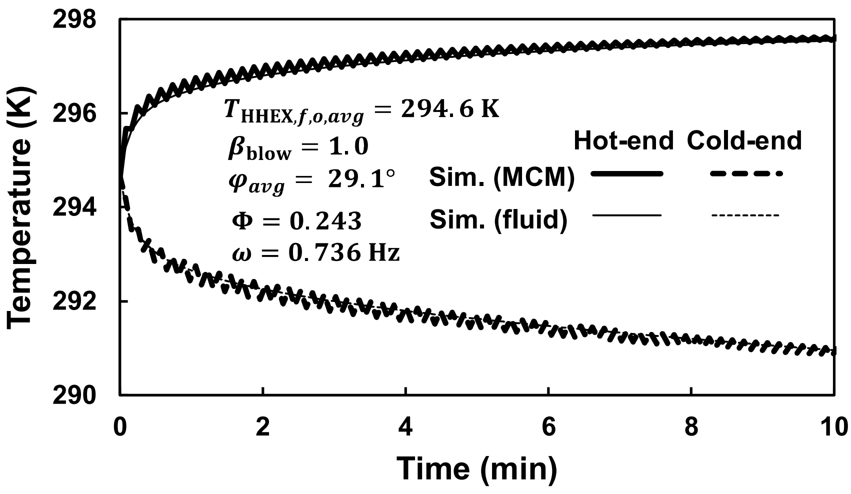

(b)

Figure 4.7 (a) Simulation and experimental results in 0.736 Hz, and 0.243 of utilization factor. (b) The solid (Gadolinium) and fluid temperautre by the simulation.

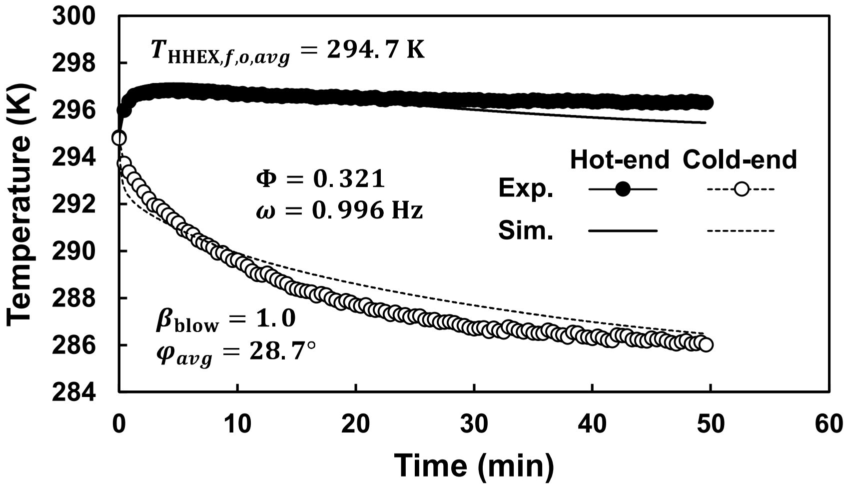

Figure 4.8 Simulation and experimental results in 0.996 Hz, and 0.321 of utilization factor.

4.4. Summary

In this chapter, the numerical model for the MR system was introduced. The model utilized the modified dispersion-concentric model, which was also applied to obtain the Nusselt number correlation between the fluid and solid in the packed bed. In consideration of the intrinsic cooling load by the heat transfer between the tubes and fluid, auxiliary parts modeling was added to the numerical model. This modeling is based on the lumped parameter thermal resistance circuits for fluid, solid, and insulation layers in the MR system.

The model was validated with the experimental results conducted in 0.736 and 0.996 Hz with different conditions of the utilization factor. The temperature profiles for both simulations follow fairly well the experimental results. However, there were several differences. First of all, the lower heat capacity in the simulation led to more temperature dropping at the cold-end of the AMR in the early stage. Moreover, the simplified T-connection in the simulation decreases the hot-end temperature in the simulation. Finally, the neglected thermal contact resistance in fittings and simplified tube geometries reduced the intrinsic cooling load in the simulation, compared to the actual system.

Lastly, the simulation results verified that the fluid temperature measured close to the AMR can be similar to the average temperature of the solid MCM inside the AMR.

Chapter 5. The optimal ratio of $\mathbf{La(Fe,Mn,Si)_{13}H_y}$ alloys in an active magnetic regenerator

5.1. Introduction

When layering $La(Fe,Mn,Si)_{13}H_y$ alloys in MR systems, they are positioned inside the AMR in a series according to their Curie temperatures. In other words, the alloy with the highest temperature is in the hot-end of the AMR, and the Curie temperature decreases as the alloy is close to the cold-end of the AMR. However, almost all studies using the alloys allocate them in the same mass or volume [72], [77]. Otherwise, specific mass ratios of them were not suggested [73]. One of the research proposed the different mass ratios of 10 layers of the $La(Fe,Mn,Si)_{13}H_y$ alloys, but the reason for that was not mentioned [17]. One of the studies proposed different length proportions when multi-layering, but the hypothetical materials based on $La(Fe,Mn,Si)_{13}H_y$ alloys were utilized during their simulation, and not by experiments [115].

In this chapter, various mass ratios of $La(Fe,Mn,Si)_{13}H_y$ alloys with different Curie temperatures were experimentally studied. The six cases for the test are first suggested. These cases are grouped along with the mass of alloy with the moderate Curie temperature which positions in the middle of the

AMRs. Next, the temperature span in no-load conditions is presented to verify which group of cases performs better that will be tested in the load condition. Under the thermal load condition, the cooling capacity and COP are evaluated to find the optimal mass ratio of layered $\mathrm{La(Fe, Mn, Si)_{13}H_y}$ alloys in the multi-layered AMR in the MR system. The tests are conducted in the MR system presented in Chapter 2.

5.2. Experimental method

5.2.1. AMRs including $\mathrm{La(Fe,Mn,Si)_{13}H_y}$ with different Curie Temperatures

$\mathrm{La(Fe,Mn,Si)_{13}H_y}$ alloys manufactured by Vacuumschmelze GmbH were prepared for the tests. The diameters of the particles are in the range of 0.3 to 0.6 mm. Those material properties, such as adiabatic temperature change by MCE from 0 to 1 T and specific heat at constant pressure in 0 and 1 T, are presented in Figure 5.1. As proposed, Gadolinium has better adiabatic temperature change by MCE than $\mathrm{La(Fe,Mn,Si)_{13}H_y}$ alloys in Figure 5.1 (a). However, the specific heat of $\mathrm{La(Fe,Mn,Si)_{13}H_y}$ alloys is much higher than that of Gadolinium in Figure 5.1 (b). Furthermore, as noticed, Gadolinium shows a continuous change of properties with respect to temperature because it undergoes a second-order phase transition (SOPT) during MCE. In contrast, $\mathrm{La(Fe,Mn,Si)_{13}H_y}$ alloys experience a rapid change of properties around their Curie temperatures because they are second-order phase transition (FOPT) materials.

The $\mathrm{La(Fe,Mn,Si)_{13}H_y}$ alloys with different Curie temperatures were aligned in AMRs with various mass ratios for comparison. The Curie temperatures of them were 287.9, 292.7, and 297.6 K. One of the AMRs is shown in Figure 5.2 where eight inner tubes containing the alloys with different mass ratios for every case. For a comparative study, the different numbers of inner tubes with the alloys were tested one by one in the MR system in Figure 2.7 and Figure 2.8. The entire six cases are shown in Table 5.1.

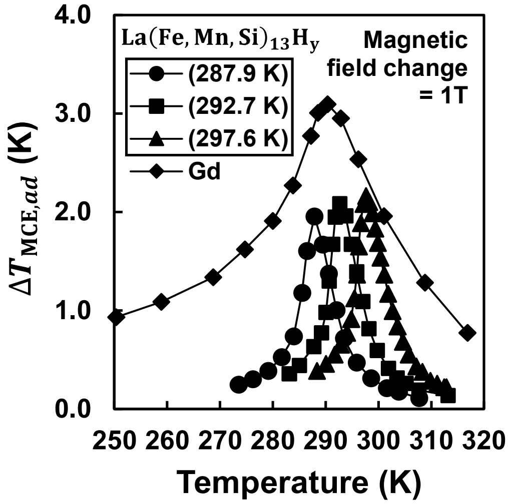

(a)

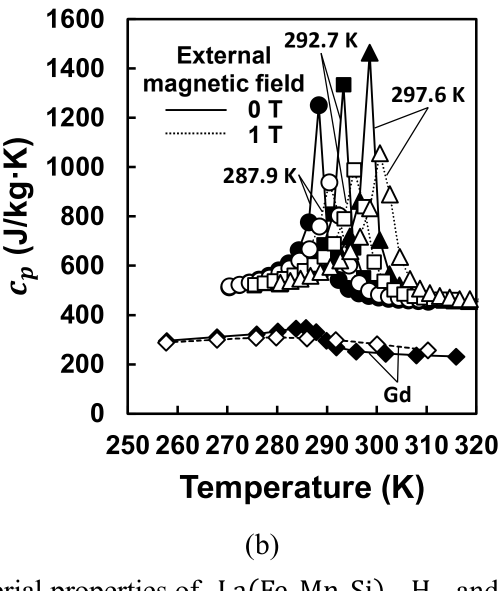

(b)

Figure 5.1 Material properties of $\mathrm{La(Fe, Mn, Si)_{13}H_y}$ and Gadolinium concerning magnetocaloric effect: (a) Adiabatic temperature change by MCE from 0 to 1 T and (b) specific heat at constant pressure in 0 and 1 T.

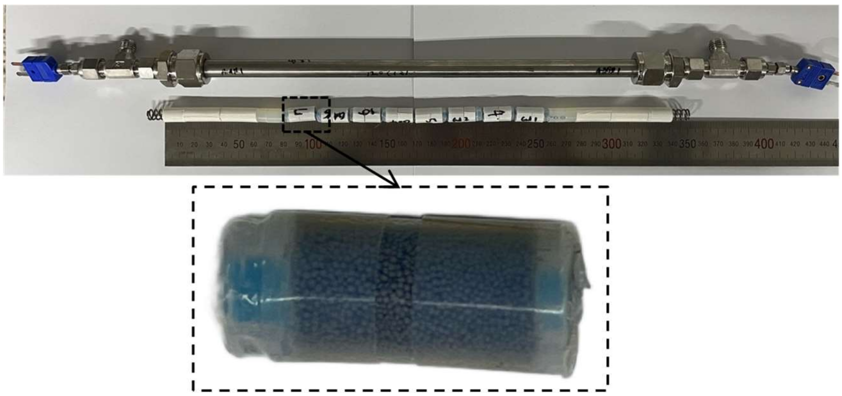

Figure 5.2 An active magnetic regenerator with serially connected eight inner tubes containing $La(Fe, Mn, Si)_{13}H_y$ with different Curie temperatures.

Table 5.1 The entire cases for the comparative study and the total mass of magnetocaloric material in active magnetic regenerators.

Case number	Number of inner tubes in a single AMR (Mass (g))			Total mass of MCM (g)	Porosity
	287.9 K	292.7 K	297.6 K		
1	2 (28.1)	3 (42.9)	3 (41.4)	112.4	0.377
2	3 (42.9)	3 (42.9)	2 (27.1)	112.9	0.374
3	4 (57.5)	3 (42.9)	1 (13.3)	113.7	0.370
4	1 (13.5)	4 (58.0)	3 (41.4)	112.9	0.374
5	2 (28.1)	4 (58.0)	2 (27.1)	113.2	0.373
6	3 (42.9)	4 (58.0)	1 (13.3)	114.2	0.367

5.2.2. Test procedure

The comparative study was separated into two groups depending on the number of inner tubes including $\mathrm{La(Fe,Mn,Si)_{13}H_y}$ alloys of 292.7 K of Curie temperature. The first group is the cases from 1 to 3, and the other is the cases from 4 to 6 in Table 5.1. Those cases were compared in their groups in no-load conditions by the results of the temperature span in different utilization factors. No-load tests were conducted in 294.2 K of the nominal operating temperature. As explained in Chapters 2 and 3, the operating temperature is the temperature of the HTF out of the HHEX, denoted by $T_{\mathrm{HHEX},f,o}$ in Figure 2.7. To calculate the utilization factor for the $\mathrm{La(Fe,Mn,Si)_{13}H_y}$ alloys in (2.8), 500 J/kg·K of the specific heat at constant pressure was applied. This is the background value of the specific heat of the $\mathrm{La(Fe,Mn,Si)_{13}H_y}$ alloys [17], [76], [116].

After the no-load test in the same operating temperature, the group resulting in the best performance was tested in different operating temperatures under the thermal load condition. The purpose of the test is to investigate the effect of the operating temperature and mass ratio of $\mathrm{La(Fe,Mn,Si)_{13}H_y}$ alloys with different Curie temperatures in AMRs on the performance of the MR system. Temperature span, cooling capacity, and COP are evaluated as the performance parameters, which are described in (2.9), (2.12), and (2.13) in chapter 2. The nominal utilization factor for the load test was controlled to be

0.160. The thermal load was supplied by the water from the thermostatic water bath to the CHEX. The cooling load was controlled by the mass flow rate of the water in the CHEX, which were 0.005, 0.015, and 0.030 kg/min. The temperature of the water at the inlet of the CHEX was set to be the same as the operating temperature of the HTF. The ambient temperature was controlled by an air-conditioner to be the same as the operating temperature. The operating frequency was controlled to be 0.720 Hz. The phase shift and the ratio of the blow time to the half-cyclic time were 28.5° and 1.0, respectively, during the whole tests.

5.3. Results and discussion

Figure 5.3 shows the test results in no-load condition for the case number from 1 to 3. First of all, as the utilization factor decreases, the temperature span improves for all the cases in Figure 5.3 (a). It is because the hot-end temperatures keep increasing even though the cold-end temperatures show the lowest between 1.0 and 2.0 as shown in Figure 5.3 (b). Most of all, case number 2 presents the best result for the temperature span in Figure 5.3 (a). As illustrated in Figure 5.3 (b), this case has higher hot-end temperatures and lower cold-end temperatures than the others in almost all ranges of the utilization factor. However, the cold-end temperatures still cannot reach the Curie temperature of 287.9 K in Figure 5.3 (b). This result indicates that the alloy with the Curie temperature of 287.9 K was not active to fully utilize MCE by the phase change. Meanwhile, the hot-end temperature is lower than the highest Curie temperature of 297.6 K in the AMR in Figure 5.3 (b). Nonetheless, the Curie temperature is still higher than the operating temperature of 294.6K as illustrated in Figure 5.3 (a). Therefore, it can be determined that $\mathrm{La(Fe, Mn, Si)_{13}H_y}$ alloy with the Curie temperature of 287.9 K should be replaced with the one with the higher Curie temperature in the AMR for better performance.

Figure 5.4 (a) describes the temperature span of the case numbers from 4 to 6 with respect to the utilization factor in no-load conditions. As shown in the legend of Figure 5.1, these cases have more mass ratio of the $\mathrm{La(Fe,Mn,Si)_{13}H_y}$ alloy with the moderate Curie temperature in an AMR, replacing a tube including the alloy with different Curie temperature in the cases from 1 to3. First of all, case number 4 shows a better temperature span than the others in the entire utilization factor ranges. This is attributed to the higher hot-end and lower cold-end temperatures, at the same time, in case number 4 as seen in Figure 5.4 (b).

It is noteworthy that more ratio of $\mathrm{La(Fe,Mn,Si)_{13}H_y}$ alloys with the lower Curie temperature cannot reduce the cold-end temperature. For example, the AMR in case number 1 has more mass ratio of the alloy with the Curie temperature of 287.9 K than in case number 4 as seen in Table 5.1. However, the cold-end temperature in case number 4 is lower, resulting in a larger temperature span in Figure 5.4 (a) than in case number 1 in Figure 5.3 (a). This tendency is also found between case numbers 2 and 5, or 3 and 6.

The results from the load tests are shown in Figure 5.5 to Figure 5.10 in different operating temperatures for the case number 4 to 6. First of all, as the operating temperature increases, the temperature span drops in all the cases in Figure 5.5, Figure 5.7, and Figure 5.9. However, when the mass ratio of the alloys with the lower Curie temperature is higher, the curve of the temperature span drops further while the operating temperature is increasing. This is because the higher the operating temperature is, the less the alloys with the lower Curie temperature make the MCE around their Curie temperature.

The cooling capacity is also described in Figure 5.6 (a), Figure 5.8 (a), and Figure 5.10 (a). Similar to the temperature span, differences in cooling capacity among the AMR cases are larger as increasing the mass flow rate of water to the CHEX for the thermal load. This tendency is also found in the COP results in Figure 5.6 (b), Figure 5.8 (b), and Figure 5.10 (b). However, the discrepancy of COP among the cases is larger than the cooling capacity. This was because of lower total power consumption by case number 5. For example, the average power consumption by the motor was 0.62, 0.59, and 0.44 W. Meanwhile, the average power consumption by the pump was 2.42, 2.80, and 2.73 W. Therefore, the total power consumption was 2.42, 2.80, and 2.73 W, in case numbers 4, 5, and 6, respectively. In this point, the higher power consumption by the motor in case number 4 means a larger MCE per unit time due to the Curie temperature of alloys in the AMRs close to the operating temperature. The power consumption by the pump was attributed to the total mass of the MCM and the porosity. For example, the total mass of the MCM was the largest value of 112.9 g but 0.374 of the porosity was the highest compared to case number 5 and 6.

This led to the lowest pressure drop among the other cases, leading to the smallest total power consumption. This also tells that case number 4 is the best arrangement using the $La(Fe, Mn, Si)_{13}H_y$ alloys with the Curie temperature because it generated the best performance even with the smaller amount of the MCM.

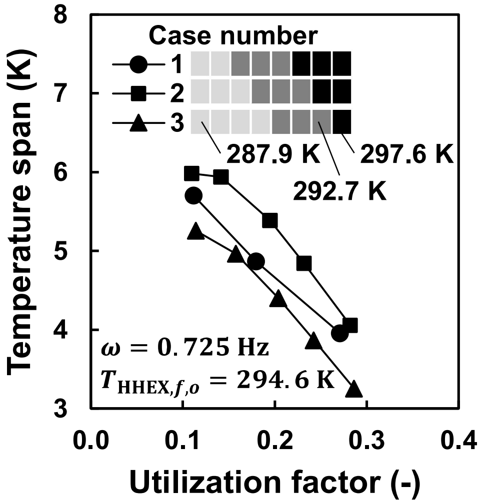

(a)

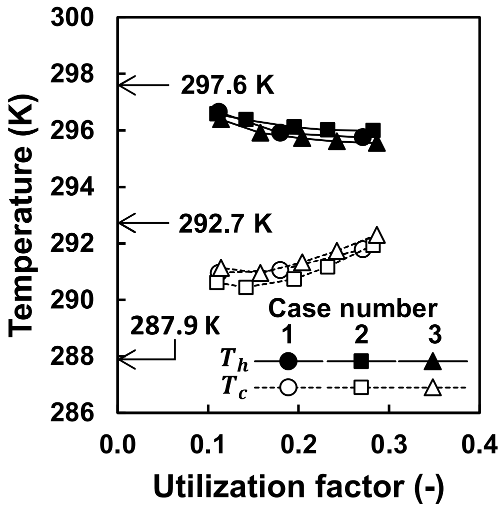

(b)

Figure 5.3 The results in no-load condition with respect to the utilization factor: (a) Temperature span and (b) hot- and cold-side temperatures for cases from 1 to 3.

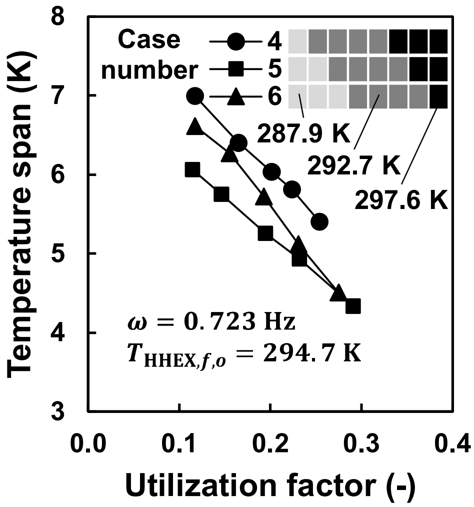

(a)

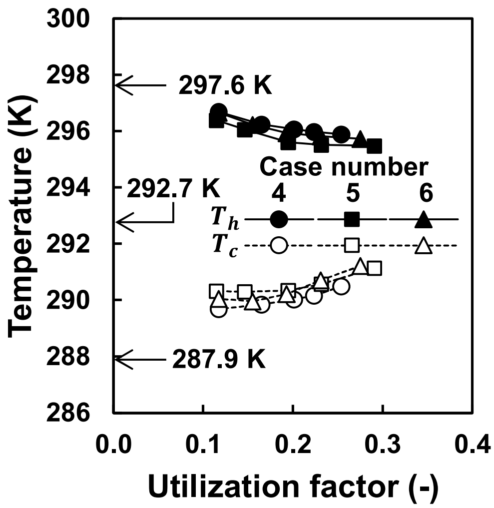

(b)

Figure 5.4 The results in no-load condition with respect to the utilization factor: (a) Temperature span and (b) hot- and cold-side temperatures for cases from 4 to 6.

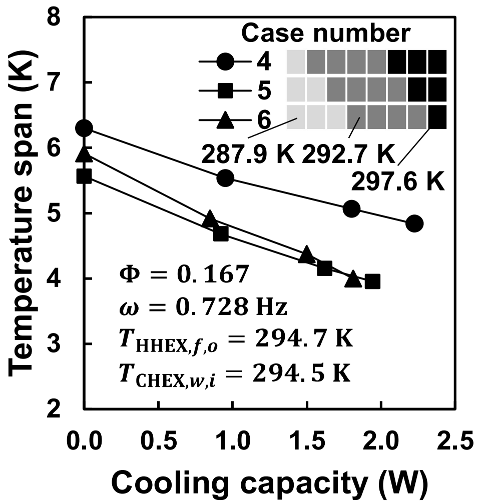

Figure 5.5 Temperature span with respect to cooling capacity in load condition in 294.7 K of the operating frequency for the cases from 4 to 6

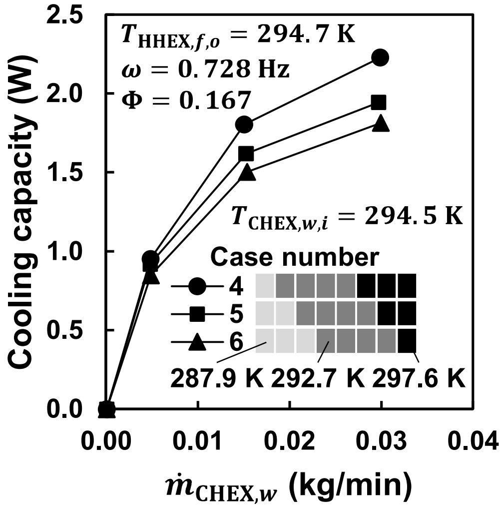

(a)

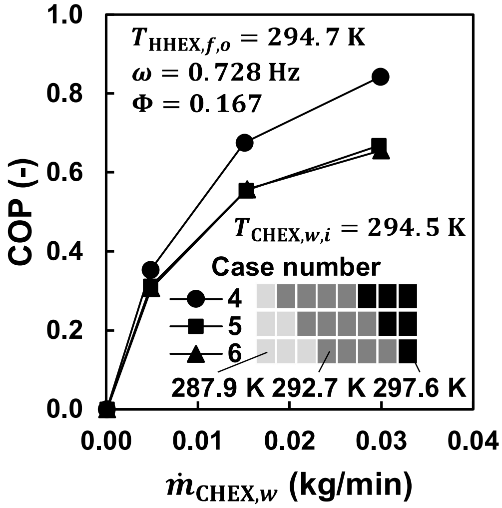

(b)

Figure 5.6 (a) Cooling capacity and (b) COP with respect to the mass flow rate of water in the CHEX in load condition in 294.7 K of the operating frequency for the cases from 4 to 6

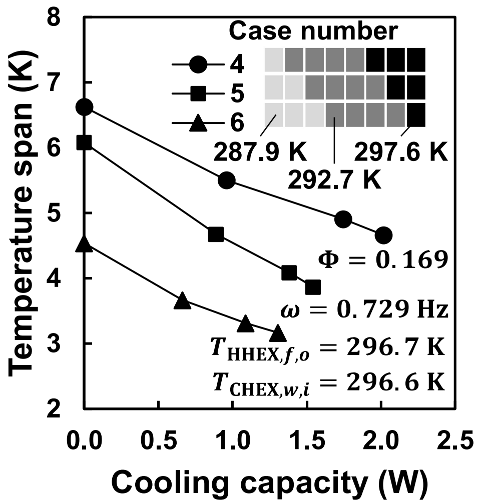

Figure 5.7 Temperature span with respect to cooling capacity in load condition in 296.7 K of the operating frequency for the cases from 4 to 6

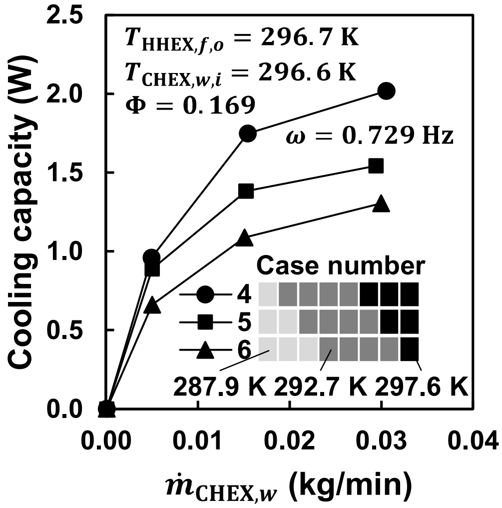

(a)

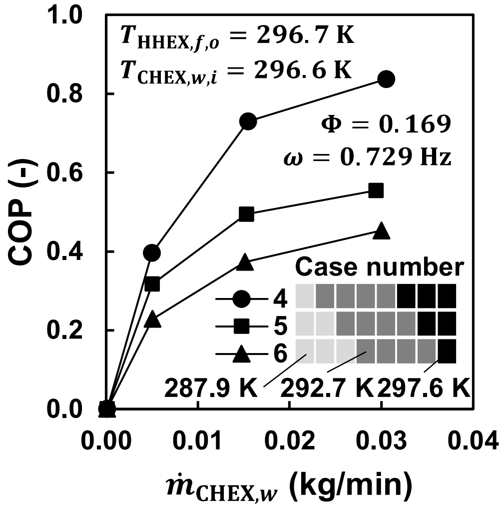

(b)

Figure 5.8 (a) Cooling capacity and (b) COP with respect to the mass flow rate of water in the CHEX in load condition in 296.7 K of the operating frequency for the cases from 4 to 6

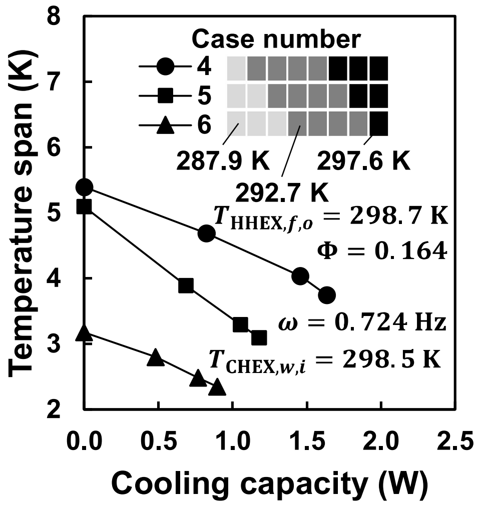

Figure 5.9 Temperature span with respect to cooling capacity in load condition in 298.7 K of the operating frequency for the cases from 4 to 6

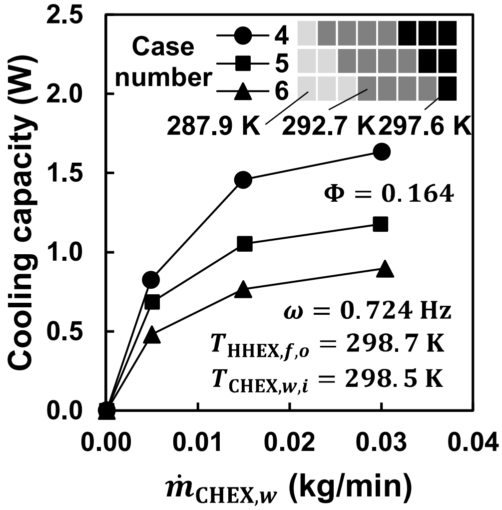

(a)

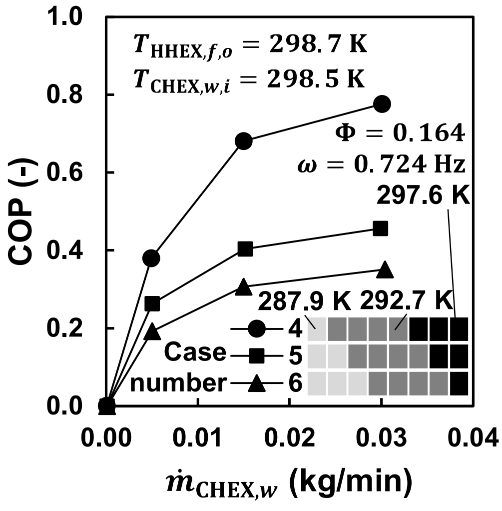

(b)

Figure 5.10 (a) Cooling capacity and (b) COP with respect to the mass flow rate of water in the CHEX in load condition in 298.7 K of the operating frequency for the cases from 4 to 6

5.4. Summary

In this chapter, the multi-layered AMRs with the different mass ratios of $La(Fe, Mn, Si)_{13}H_y$ alloys were compared to one another. The AMRs contained them with the Curie temperatures of 287.9, 292.7, and 297.6 K which were determined from the adiabatic temperature change in 1 T by data from the manufacturer. In total, 6 cases of different mass ratios of them were prepared.

The temperature span was first evaluated to find the better mass ratio of the alloy with the moderate Curie temperature. As the alloy with the lowest Curie temperature was included less, the temperature span improved in no-load tests. It was because the cold-end temperature of the AMR was still higher than the lowest Curie temperature. It was also found in the cases with the more mass ratio of the alloy with the moderate Curie temperature, but they resulted in a better temperature span. As a result, the 7.0 K of the maximum temperature span was obtained in case number 4 in the no-load tests.

In the load tests, the cases with the higher mass ratio of the moderate Curie temperatures were investigated to examine the effect of the thermal load, and operating temperature. Higher operating temperature deteriorates the temperature span in all the cases but the tendency was more severe in case of more mass ratio of the alloy with the lowest Curie temperature due to their less MCE per unit time. Moreover, even though case number 4 with the less total mass of the MCM presented better cooling capacity and COP. This fact indicates that the optimal mass ratio of the $\mathrm{La(Fe,Mn,Si)_{13}H_y}$ alloys should be considered when layering them in the AMRs in MR systems. The maximum cooling capacity was 2.23 W with 4.8 K of the temperature span in the MR system. In addition, the highest COP was 0.8. Both the maximum values of the cooling capacity and COP were produced with the AMRs of case number 4 where the mass ratio of the $\mathrm{La(Fe,Mn,Si)_{13}H_y}$ alloys with Curie temperatures of 287.9, 292.7, and 297.6 K were 13.5, 58.0, and 41.4 g, respectively.

Chapter 6. Concluding remarks

As the HFC refrigerants are phasing out, the replacements such as HFO or natural refrigerants are used in the conventional vapor compression refrigeration system. However, due to their higher power consumption or flammability, alternative technology is required in the industry. Moreover, an efficient system is also demanded to reduce CO2 emissions worldwide. The magnetic refrigeration (MR) system is one of the alternatives to the vapor compression refrigeration system. For a better operation of the MR system, it is necessary to define the operating parameters in the MR system, to find which is crucial for better performance. Moreover, it is also important to reduce the power consumption by the pump in the MR system, because the active magnetic regenerator (AMR) is the essential component but it brings about a high-pressure drop. So far, various simulation model was developed for the MR system, but most of the studies use energy equation which does not match the Nusselt number correlation for the fluid and solid phase in the packed bed of AMRs. Finally, the first-order phase transition (FOPT) materials should be layered in the AMRs for the MR system because of their abrupt MCE around their Curie temperatures. However, most of the research layered only with the same mass ratios of the FOPT materials.

In chapter 2, the parametric study for the MR system was presented. First of all, the experimental setup and its operation method were explained. The new parameters such as phase shift and blow fraction were defined to evaluate the synchronization between the magnet assembly and the AMRs. Moreover, the utilization factor, operating frequency, and operating temperature were tested to figure out their effect on the performance of the MR system. The heat source temperature was also controlled to find the second law of efficiency of the MR system. The best temperature span was obtained as 11.5 K in 1.151 Hz of the operating frequency in the no-load test. In addition, 4.82 W and 2.40 of the COP were produced in load tests. It was also proven that the operating temperature can increase the cooling capacity and COP, by maintaining the total power consumption.

In chapter 3, a novel method to reduce the pressure drop in the AMR was introduced. The AMRs with the irregular Gadolinium particle were prepared, and the external magnetic field was applied to align them. For comparison, the non-aligned AMRs were also tested. According to the X-ray computed tomography, the particles were observed to be packed in parallel to the flow direction. Meanwhile, the particles were randomly distributed in the non-aligned AMRs. The pressure drop by the aligned AMR was 18.8% less than the non-aligned AMRs. It was also found that the friction factor of the aligned AMR was 20.5% smaller than the packed bed with spheres having the equivalent diameter, according to the Carman correlation. Finally, the COP was improved up to 37.3% in the 4.5 K of the temperature span by using the aligned AMRs, compared to the one with the non-aligned AMRs.

In chapter 4, the simulation model was developed. The simulation used the energy equations in a packed bed for the solid and fluid phases, which also match the Nusselt number correlation for the packed bed. Even though the temperature profiles from the simulation follow the experimental results, there were several differences. The main reasons were simplified T-connection and tubes. Moreover, the simplified geometries resulted in a less intrinsic cooling load in simulation. Furthermore, it was verified that the hot- or cold-end temperature measured from the HTF can indicate the solid temperature at both ends of AMRs.

In the last chapter, the different mass ratios of the $\mathrm{La(Fe,Mn,Si)_{13}H_y}$ alloys were tested for better performance using the same total mass of the alloys. In no-load tests, the higher mass ratio of the alloy with the moderate Curie temperature presented a better temperature span. The maximum temperature span from the no-load tests was 7.0 K by the optimal mass ratios of the $\mathrm{La(Fe,Mn,Si)_{13}H_y}$ alloys. In the load tests, the optimal mass ratio of the alloys showed less reduction of the cooing capacity and COP in different operating temperatures. In conclusion, 2.23 W of the maximum cooling capacity, and 0.8 of the best COP were obtained by using the optimal mass ratio of the $La(Fe,Mn,Si)_{13}H_y$ alloys.

Reference

[1] X. She, L. Cong, B. Nie, G. Leng, H. Peng, Y. Chen, X. Zhang, T. Wen, H. Yang, Y. Luo. Energy-efficient and-economic technologies for air conditioning with vapor compression refrigeration: A comprehensive review. Applied Energy. 232 (2018) 157-86.

[2] G. Myhre, D. Shindell, J. Pongratz. Anthropogenic and Natural Radiative Forcing. 2014.

[3] R. Llopis, D. Sánchez, R. Cabello. Refrigerants for vapor compression refrigeration systems: A review on natural and artificial heat transfer fluids. Advances in New Heat Transfer Fluids. 2017. pp. 463-522.

[4] J.L. Yang, Y.T. Ma, M.X. Li, H.Q. Guan. Exergy analysis of transcritical carbon dioxide refrigeration cycle with an expander. Energy. 30 (2005) 1162-75.

[5] J. Sarkar, S. Bhattacharyya, M.R. Gopal. Transcritical CO2 heat pump systems: exergy analysis including heat transfer and fluid flow effects. Energy Conversion and Management. 46 (2005) 2053-67.

[6] F. Bruno, M. Belusko, E. Halawa. CO2 refrigeration and heat pump systems—a comprehensive review. Energies. 12 (2019) 2959.

[7] D. Calleja-Anta, L. Nebot-Andrés, J. Catalán-Gil, D. Sánchez, R. Cabello,

R. Llopis. Thermodynamic screening of alternative refrigerants for R290 and R600a. Results in Engineering. 5 (2020) 100081.

[8] IEC 60335-2-89: 2019. Household and similar electrical appliances-Safety-Part 2-89: Particular requirements for commercial refrigerating appliances and ice-makers with an incorporated or remote refrigerant unit or motor-compressor. (2019).

[9] International Energy Agency. The Future of Cooling: Opportunities for energy-efficient air conditioning. OECD Publishing. (2018).

[10] M. Isaac, D.P. Van Vuuren. Modeling global residential sector energy demand for heating and air conditioning in the context of climate change. Energy Policy. 37 (2009) 507-21.

[11] R. Gauß, G. Homm, O. Gutfleisch. The resource basis of magnetic refrigeration. Journal of Industrial Ecology. 21 (2017) 1291-300.

[12] W. Goetzler, R. Zogg, J. Young, C. Johnson. Energy savings potential and RD&D opportunities for non-vapor-compression HVAC technologies. Navigant Consulting Inc, prepared for US Department of Energy. 199 (2014).

[13] Y. Zhang, J. Wu, J. He, K. Wang, G. Yu. Solutions to obstacles in the commercialization of room-temperature magnetic refrigeration. Renewable and Sustainable Energy Reviews. 143 (2021) 110933.

[14] D.B.N. Fernandez, J. Dirks, T. Stout. The Prospects of Alternatives to

Vapor Compression Technology for Space Cooling and Food Refrigeration Applications. 2010.

[15] A. Kitanovski, P.W. Egolf. Application of magnetic refrigeration and its assessment. Journal of Magnetism and Magnetic Materials. 321 (2009) 777-81.

[16] O. Gutfleisch, M.A. Willard, E. Brück, C.H. Chen, S. Sankar, J.P. Liu. Magnetic materials and devices for the 21st century: stronger, lighter, and more energy efficient. Advanced Materials. 23 (2011) 821-42.

[17] M. Masche, J. Liang, S. Dall'Olio, K. Engelbrecht, C.R.H. Bahl. Performance analysis of a high-efficiency multi-bed active magnetic regenerator device. Applied Thermal Engineering. 199 (2021) 117569.

[18] B. Yu, Q. Gao, B. Zhang, X. Meng, Z. Chen. Review on research of room temperature magnetic refrigeration. International Journal of Refrigeration. 26 (2003) 622-36.

[19] P. Weiss, A. Piccard. Le phénomène magnétocalorique. Journal of Physics: Theories and Applications. 7 (1917) 103-9.

[20] A. Smith. Who discovered the magnetocaloric effect? The European Physical Journal H. 38 (2013) 507-17.

[21] A.H. Morrish. The Physical Principles of Magnetism. The Institute of Electrical and Electronics Engineers. 2001.

[22] V.K. Pecharsky, K.A. Gschneidner Jr. Magnetocaloric effect and magnetic

refrigeration. Journal of Magnetism and Magnetic Materials. 200 (1999) 44-56.

[23] V. Pecharsky, K. Gschneidner Jr, A. Pecharsky, A. Tishin. Thermodynamics of the magnetocaloric effect. Physical Review B. 64 (2001) 144406.

[24] J. Tušek, A. Kitanovski, S. Zupan, I. Prebil, A. Poredoš. A comprehensive experimental analysis of gadolinium active magnetic regenerators. Applied Thermal Engineering. 53 (2013) 57-66.

[25] P.V. Trevizoli, A.T. Nakashima, G.F. Peixer, J.R. Barbosa Jr. Performance assessment of different porous matrix geometries for active magnetic regenerators. Applied Energy. 187 (2017) 847-61.

[26] Z. Li, J. Shen, K. Li, X. Gao, X. Guo, W. Dai. Assessment of three different gadolinium-based regenerators in a rotary-type magnetic refrigerator. Applied Thermal Engineering. 153 (2019) 159-67.

[27] M. Kondo, K. Ueno, K. Takeuchi, R. Nomura, T. Kizaki. Effects of magnetocaloric wire on increase in magnetic refrigeration cycle. Fujikura Technical Review. 47 (2017) 47-50.

[28] A. Waske, M.E. Gruner, T. Gottschall, O. Gutfleisch. Magnetocaloric materials for refrigeration near room temperature. MRS Bulletin. 43 (2018) 269-73.

[29] T. Lei, K. Engelbrecht, K.K. Nielsen, C.T. Veje. Study of geometries of

active magnetic regenerators for room temperature magnetocaloric refrigeration. Applied Thermal Engineering. 111 (2017) 1232-43.

[30] D. Vuarnoz, T. Kawanami. Numerical analysis of a reciprocating active magnetic regenerator made of gadolinium wires. Applied Thermal Engineering. 37 (2012) 388-95.

[31] Y.Q. Cai, Y.Y. Jiao, Q. Cui, J.W. Cai, Y. Li, B.S. Wang, M.T. Fernández-Díaz, M.A. McGuire, J.Q. Yan, J.A. Alonso, J.G. Cheng. Giant reversible magnetocaloric effect in the pyrochlore Er2Mn2O7 due to a cooperative two-sublattice ferromagnetic order. Physical Review Materials. 1 (2017) 064408.

[32] J. Liu, T. Gottschall, K.P. Skokov, J.D. Moore, O. Gutfleisch. Giant magnetocaloric effect driven by structural transitions. Nature Materials. 11 (2012) 620-6.

[33] M. Bratko, E. Lovell, A.D. Caplin, V. Basso, A. Barcza, M. Katter, L.F. Cohen. Determining the first-order character of La(Fe,Mn,Si)13. Physical Review B. 95 (2017) 064411.

[34] J. Chen, B. Shen, Q. Dong, F. Hu, J. Sun. Large reversible magnetocaloric effect caused by two successive magnetic transitions in ErGa compound. Applied Physics Letters. 95 (2009) 132504.

[35] J. Xu, X. Zheng, S. Yang, L. Xi, D. Wang, C. Liu, J. Zhang, Y. Wu, J. Shen, S. Wang. Large reversible magnetic entropy change of R3Ni6Al2 (R= Dy, Ho

and Er) compounds. Journal of Alloys and Compounds. 879 (2021) 160468.

[36] K. Binnemans, P.T. Jones, K. Van Acker, B. Blanpain, B. Mishra, D. Apelian. Rare-earth economics: the balance problem. The Journal of The Minerals, Metals & Materials Society. 65 (2013) 846-8.

[37] K.A. Gschneidner Jr, V.K. Pecharsky. Rare earths and magnetic refrigeration. Journal of Rare Earths. 24 (2006) 641-7.

[38] V. Zepf. Rare Earth Elements: What and Where They Are. Springer. 2013. pp. 11-39.

[39] S.R. Taylor. Abundance of chemical elements in the continental crust: A new table. Geochimica et Cosmochimica Acta. 28 (1964) 1273-85.

[40] L. Talens Peiró, G. Villalba Méndez. Material and energy requirement for rare earth production. The Journal of The Minerals, Metals & Materials Society. 65 (2013) 1327-40.

[41] J. Lozano, K. Engelbrecht, C.R. Bahl, K.K. Nielsen, D. Eriksen, U.L. Olsen, J. Barbosa Jr, A. Smith, A. Prata, N. Pryds. Performance analysis of a rotary active magnetic refrigerator. Applied Energy. 111 (2013) 669-80.

[42] D. Benke, M. Fries, M. Specht, J. Wortmann, M. Pabst, T. Gottschall, I. Radulov, K. Skokov, A.I. Bevan, D. Prosperi. Magnetic refrigeration with recycled permanent magnets and free rare-earth magnetocaloric La–Fe–Si. Energy Technology. 8 (2020) 1901025.

[43] A.T. Nakashima, F.P. Fortkamp, N.M. de Sá, V.M. dos Santos, G. Hoffmann, G.F. Peixer, S.L. Dutra, M.C. Ribeiro, J.A. Lozano, J.R. Barbosa Jr. A magnetic wine cooler prototype. International Journal of Refrigeration. 122 (2021) 110-21.

[44] L. Griffith, A. Czernuszewicz, J. Slaughter, V. Pecharsky. CaloriSMART: Small-scale test-stand for rapid evaluation of active magnetic regenerator performance. Energy Conversion and Management. 199 (2019) 111948.

[45] B. Huang, J. Lai, D. Zeng, Z. Zheng, B. Harrison, A. Oort, N. van Dijk, E. Brück. Development of an experimental rotary magnetic refrigerator prototype. International Journal of Refrigeration. 104 (2019) 42-50.

[46] J. He, J. Wu, B. Lu, C. Liu. Comparative study on the series, parallel and cascade cycles of a multi-mode room temperature magnetic refrigeration system. International Journal of Refrigeration. 117 (2020) 94-103.

[47] S. Lionte, M. Risser, C. Muller. A 15kW magnetocaloric proof-of-concept unit: Initial development and first experimental results. International Journal of Refrigeration. 122 (2021) 256-65.

[48] L.A. Tagliafico, F. Scarpa, F. Valsuani, G. Tagliafico. Preliminary experimental results from a linear reciprocating magnetic refrigerator prototype. Applied Thermal Engineering. 52 (2013) 492-7.

[49] T. Keawkamrop, A.S. Dalkilic, L.G. Asirvatham, J. Amani, O. Mahian, S.

Wongwises. Experimental investigation on the performance of a parallel plate-based active magnetic regenerator. International Journal of Air-Conditioning and Refrigeration. 26 (2018) 1850018.

[50] T. Keawkamrop, S. Wongwises. Effect of cycle frequency of a reciprocating magnetic refrigerator prototype on the temperature span and cooling capacity. International Journal of Air-Conditioning and Refrigeration. 27 (2019) 1950002.

[51] S. Lionte, C. Vasile, M. Siroux. Numerical analysis of a reciprocating active magnetic regenerator. Applied Thermal Engineering. 75 (2015) 871-9.

[52] M. Risser. Modélisation Multiphysique et MulticonfigurationNelle D'évaluation et D'optimisation des Performances des Systèmes de Réfrigération Magnétocalorique. Strasbourg. 2011.

[53] T.F. Petersen, N. Pryds, A. Smith, J. Hattel, H. Schmidt, H.J.H. Knudsen. Two-dimensional mathematical model of a reciprocating room-temperature active magnetic regenerator. International Journal of Refrigeration. 31 (2008) 432-43.

[54] K.K. Nielsen, C.R.H. Bahl, A. Smith, R. Bjørk, N. Pryds, J. Hattel. Detailed numerical modeling of a linear parallel-plate active magnetic regenerator. International Journal of Refrigeration. 32 (2009) 1478-86.

[55] M.S. Kamran, J. Sun, Y.B. Tang, Y.G. Chen, J.H. Wu, H.S. Wang.

Numerical investigation of room temperature magnetic refrigerator using microchannel regenerators. Applied Thermal Engineering. 102 (2016) 1126-40.

[56] V. Gnielinski. New equations for heat and mass transfer in turbulent pipe and channel flow. International Journal of Chemical Engineering. 16 (1976) 359-68.

[57] K. Engelbrecht. A Numerical Model of an Active Magnetic Regenerator with Experimental Validation. Ph D Thesis, University of Wisconsin-Madison. (2008).

[58] F.P. Fortkamp, G.B. Lang, J.A. Lozano, J. Barbosa Jr. Design trade-offs for an active magnetic regenerator device. Applied Thermal Engineering. 165 (2020) 114467.

[59] P.V. Trevizoli. Development of thermal regenerators for magnetic cooling applications. Federal University of Santa Catarina. 2015.

[60] D. Silva, J. Ventura, J. Araújo, A. Pereira. Maximizing the temperature span of a solid state active magnetic regenerative refrigerator. Applied Energy. 113 (2014) 1149-54.

[61] K. Hamdani, A. Smaili, O. Sari. Numerical simulation of hydrogen active magnetic regenerative liquefier. Renewable Energy. 158 (2020) 487-99.

[62] N. Wakao, S. Kagei. Heat and mass transfer in packed beds. Taylor & Francis. 1982.

[63] J. Tušek, A. Kitanovski, A. Poredoš. Geometrical optimization of packed-bed and parallel-plate active magnetic regenerators. International Journal of Refrigeration. 36 (2013) 1456-64.

[64] J. Tušek, A. Kitanovski, I. Prebil, A. Poredoš. Dynamic operation of an active magnetic regenerator (AMR): Numerical optimization of a packed-bed AMR. International Journal of Refrigeration. 34 (2011) 1507-17.

[65] X. Guo, K. Li, J. Shen, Z. Li, X. Gao, W. Dai. A correction of porous media model for active magnetic regenerator based on a finite thermal penetration depth. Applied Thermal Engineering. 152 (2019) 468-74.

[66] H. Johra, K. Filonenko, P.K. Heiselberg, C.T. Veje, S. Dall'Olio, K. Engelbrecht, C. Bahl. Active magnetic regenerators implemented as a magnetocaloric heat pump for residential buildings. Thermag VIII: International Conference on Caloric Cooling. International Institute of Refrigeration IIF/IIR2018. pp. 21-6.

[67] M. Katter, V. Zellmann, G.W. Reppel, K. Uestuener. Magnetocaloric properties of La(Fe,Co,Si)13 bulk material prepared by powder metallurgy. IEEE Transactions on Magnetics. 44 (2008) 3044-7.

[68] J. Lyubina, R. Schäfer, N. Martin, L. Schultz, O. Gutfleisch. Novel design of La(Fe,Si13 alloys towards high magnetic refrigeration performance. Advanced Materials. 22 (2010) 3735-9.

[69] A. Barcza, M. Katter, V. Zellmann, S. Russek, S. Jacobs, C. Zimm. Stability and magnetocaloric properties of sintered La(Fe,Si,Mn)13Hz alloys. IEEE transactions on magnetics. 47 (2011) 3391-4.

[70] A. Smith, C.R. Bahl, R. Bjørk, K. Engelbrecht, K.K. Nielsen, N. Pryds. Materials challenges for high performance magnetocaloric refrigeration devices. Advanced Energy Materials. 2 (2012) 1288-318.

[71] V. Basso, M. Küpferling, C. Curcio, C. Bennati, A. Barzca, M. Katter, M. Bratko, E. Lovell, J. Turcaud, L.F. Cohen. Specific heat and entropy change at the first order phase transition of La(Fe-Mn-Si)13-H compounds. Journal of Applied Physics. 118 (2015) 053907.

[72] K. Navickaitė, H.N. Bez, T. Lei, A. Barcza, H. Vieyra, C.R. Bahl, K. Engelbrecht. Experimental and numerical comparison of multi-layered La(Fe,Si,Mn)13Hy active magnetic regenerators. International Journal of Refrigeration. 86 (2018) 322-30.

[73] H.N. Bez, K. Navickaité, T. Lei, K. Engelbrecht, A. Barcza, C. Bahl. Epoxy-bonded La(Fe,Mn,Si)13Hz as a multi layered active magnetic regenerator. 7th International Conference on Magnetic Refrigeration at Room Temperature (Thermag VII). International Institute of Refrigeration. 2016.

[74] T. Christiaanse, P. Trevizoli, A. Rowe. Modelling two layer Mn–Fe–Si–P materials in an active magnetic regenerator. International Journal of

Refrigeration. 106 (2019) 225-35.

[75] M. Zhang, O. Abdelaziz, A.M. Momen, A. Abu-Heiba. A numerical analysis of a magnetocaloric refrigerator with a 16-layer regenerator. Scientific Reports. 7 (2017) 1-12.

[76] J. Liang, M. Masche, K. Engelbrecht, K.K. Nielsen, H.A. Vieyra, A. Barcza, C.R. Bahl. Experimental study of non-bonded packed bed active magnetic regenerators with stabilized La(Fe,Mn,Si)13Hy particles. Applied Thermal Engineering. 197 (2021) 117383.

[77] B.P. Vieira, H.N. Bez, M. Kuepferling, M.A. Rosa, D. Schafer, C.C.P. Cid, H.A. Vieyra, V. Basso, J.A. Lozano, J.R. Barbosa Jr. Magnetocaloric properties of spheroidal La(Fe,Mn,Si)13Hy granules and their performance in epoxy-bonded active magnetic regenerators. Applied Thermal Engineering. 183 (2021) 116185.

[78] V. Chaudhary, X. Chen, R.V. Ramanujan. Iron and manganese based magnetocaloric materials for near room temperature thermal management. Progress in Materials Science. 100 (2019) 64-98.

[79] S. Lionte, A. Barcza, M. Risser, C. Muller, M. Katter. LaFeSi-based magnetocaloric material analysis: Cyclic endurance and thermal performance results. International Journal of Refrigeration. 124 (2021) 43-51.

[80] K.H. Kang, Y. Oh, J.H. Kim, E.J. Kim, H. Kim, C.S. Yoon. Magnetocaloric

effect of compositionally partitioned Mn5−xGe3Nix alloys produced by solid state sintering. Journal of Alloys and Compounds. 681 (2016) 541-6.

[81] A. Tura, A. Rowe. Permanent magnet magnetic refrigerator design and experimental characterization. International Journal of Refrigeration. 34 (2011) 628-39.

[82] J.A. Lozano, M.S. Capovilla, P.V. Trevizoli, K. Engelbrecht, C.R. Bahl, J.R. Barbosa Jr. Development of a novel rotary magnetic refrigerator. International Journal of Refrigeration. 68 (2016) 187-97.

[83] K. Engelbrecht, D. Eriksen, C. Bahl, R. Bjørk, J. Geyti, J. Lozano, K.K. Nielsen, F. Saxild, A. Smith, N. Pryds. Experimental results for a novel rotary active magnetic regenerator. International Journal of Refrigeration. 35 (2012) 1498-505.

[84] F. Fortkamp, D. Eriksen, K. Engelbrecht, C. Bahl, J. Lozano, J. Barbosa Jr. Experimental investigation of different fluid flow profiles in a rotary multi-bed active magnetic regenerator device. International Journal of Refrigeration. 91 (2018) 46-54.

[85] Z. Li, K. Li, X. Guo, X. Gao, W. Dai, M. Gong, J. Shen. Influence of timing between magnetic field and fluid flow in a rotary magnetic refrigerator. Applied Thermal Engineering. 187 (2021) 116477.

[86] A.T. Nakashima, S.L. Dutra, P.V. Trevizoli, J.R. Barbosa Jr. Influence of

the flow rate waveform and mass imbalance on the performance of active magnetic regenerators. Part I: Experimental analysis. International Journal of Refrigeration. 93 (2018) 236-48.

[87] R. Teyber, P. Trevizoli, I. Niknia, T. Christiaanse, P. Govindappa, A. Rowe. Experimental performance investigation of an active magnetic regenerator subject to different fluid flow waveforms. International Journal of Refrigeration. 74 (2017) 38-46.

[88] D. Eriksen, K. Engelbrecht, C. Bahl, R. Bjørk, K.K. Nielsen, A.R. Insinga, N. Pryds. Design and experimental tests of a rotary active magnetic regenerator prototype. International Journal of Refrigeration. 58 (2015) 14-21.

[89] L. Griffith, A. Czernuszewicz, J. Slaughter, V. Pecharsky. Active magnetic regenerative cooling with smaller magnets. International Journal of Refrigeration. 125 (2021) 44-51.

[90] J. Kaštil, J. Tětek, A. Tuček. Experimental investigation of small-scale magnetocaloric refrigerator. Acta Physica Polonica, A. 124 (2013).

[91] J. Taylor. Introduction to Error Analysis, the Study of Uncertainties in Physical Measurements. 1997.

[92] ASHRAE. Guideline 2-2010 (RA 2014) - Engineering Analysis of Experimental Data. Atlanta, GA. 2014.

[93] P.V. Trevizoli, A.T. Nakashima, G.F. Peixer, J.R. Barbosa Jr. Performance

evaluation of an active magnetic regenerator for cooling applications–part I: Experimental analysis and thermodynamic performance. International Journal of Refrigeration. 72 (2016) 192-205.

[94] C. Zimm, A. Jastrab, A. Sternberg, V. Pecharsky, K. Gschneidner, M. Osborne, I. Anderson. Description and performance of a near-room temperature magnetic refrigerator. Advances in Cryogenic Engineering. Springer1998. pp. 1759-66.

[95] M.S. Kamran, H.O. Ahmad, H.S. Wang. Review on the developments of active magnetic regenerator refrigerators–Evaluated by performance. Renewable and Sustainable Energy Reviews. 133 (2020) 110247.

[96] A. Kitanovski, J. Tušek, U. Tomc, U. Plaznik, M. Ožbolt, A. Poredoš. Magnetocaloric Energy Conversion. Springer. 2016.

[97] T. Johnson, P. Levison, P. Shearing, D. Bracewell. X-ray computed tomography of packed bed chromatography columns for three dimensional imaging and analysis. Journal of Chromatography A. 1487 (2017) 108-15.

[98] Y. Wang, C. Lin, J. Miller. Quantitative analysis of exposed grain surface area for multiphase particles using X-ray microtomography. Powder Technology. 308 (2017) 368-77.

[99] T. Buchwald, G. Schmandra, L. Schützenmeister, T. Fraszczak, T. Mütze, U. Peuker. Gaseous flow through coarse granular beds: The role of specific

surface area. Powder Technology. 366 (2020) 821-31.

[100] A. Rabbani, S. Jamshidi, S. Salehi. Determination of specific surface of rock grains by 2D imaging. Journal of Geological Research. 2014 (2014).

[101] D. Müter, H. Sørensen, D. Jha, R. Harti, K. Dalby, H. Suhonen, R. Feidenhans'l, F. Engstrøm, S. Stipp. Resolution dependence of petrophysical parameters derived from X-ray tomography of chalk. Applied Physics Letters. 105 (2014) 043108.

[102] B. Dietrich. Heat transfer coefficients for solid ceramic sponges–Experimental results and correlation. International Journal of Heat and Mass Transfer. 61 (2013) 627-37.

[103] D. Wen, Y. Ding. Heat transfer of gas flow through a packed bed. Chemical Engineering Science. 61 (2006) 3532-42.

[104] J. Yang, J. Wang, S. Bu, M. Zeng, Q. Wang, A. Nakayama. Experimental analysis of forced convective heat transfer in novel structured packed beds of particles. Chemical Engineering Science. 71 (2012) 126-37.

[105] B. Munson, D. Young, T. Okiishi, W. Huebsch. Fundamentals of Fluid Mechanics, 6th international student ed. John Wiley: Hoboken, NJ, USA. 2010.

[106] S. Whitaker. Flow in porous media I: A theoretical derivation of Darcy's law. Transport in Porous Media. 1 (1986) 3-25.

[107] H. Darcy. Les fontaines publiques de la ville de Dijon: Exposition et

application des principes à suivre et des formules à employer dans les questions de distribution d'eau: Ouvrage terminé par un appendice relatif aux fournitures d'eau de plusieurs villes, au filtrage des eaux et à la fabrication des tuyaux de fonte, de plomb, de tôle et de bitume. V. Dalmont. 1856.

[108] G. Zheng, X. Dai, Y. Diao. Parameter analysis of water flow during EPBS tunnelling and an evaluation method of spewing failure based on a simplified model. Engineering Failure Analysis. 58 (2015) 96-112.

[109] D.A. Nield, A. Bejan. Convection in Porous Media. Springer. 2006.

[110] R.B. Bird, W.E. Stewart, E.N. Lightfoot, D.J. Klingenberg. Introductory Transport Phenomena. Wiley Global Education. 2015.

[111] J.L. Cadena. Designing a rotary magnetic refrigerator. Ph D Thesis, Federal University of Santa Catarina. 2015.

[112] D. Gunn, J. De Souza. Heat transfer and axial dispersion in packed beds. Chemical Engineering Science. 29 (1974) 1363-71.

[113] R. Krupiczka. Analysis of heat conductivity in granular materials (Heat conductivity coefficients of granular materials calculated by cylindrical and spherical models with porosity of 0.215 and 0.476 respectively). Chemia Stosowana, Seria B. 3 (1966) 183-226.

[114] B.W. Gamson. Heat and mass transfer-fluid solid systems. Chemical Engineering Progress. 47 (1951) 19-28.

[115] L. Yuan, S. Qian, J. Yu. Numerical study on the multi-layered magnetocaloric regenerators. Applied Thermal Engineering. 204 (2022) 118001.

[116] J. Liang, C.D. Christiansen, K. Engelbrecht, K.K. Nielsen, R. Bjørk, C.R. Bahl. Heat transfer and flow resistance analysis of a novel freeze-cast regenerator. International Journal of Heat and Mass Transfer. 155 (2020) 119772.

국문 초록

프레온 냉매에 대한 국제 규제와 자연 냉매의 화염성으로 인해 기존의 증기 압축식 냉동 시스템을 대체할 기술의 필요성이 대두된다. 또한, 공조 냉동 시스템에서의 높은 CO_2 배출량은 대안적인 냉동 시스템을 필요로 한다. 한편, 자기 냉동 시스템은 기존의 증기 압축식 냉동 시스템을 대체할 비압축식 냉동 시스템 중 하나로 평가받는다. 그러나 자기 냉동 시스템은 그 구성과 작동 방법이 기존의 증기 압축식 냉동 시스템과 다르므로 시스템 운전 변수에 관한 포괄적인 연구가 필요하다. 또한, 자기 냉동 시스템에서 펌프에 의한 전력 소모는 열전달 유체의 질량 유량이 크고 자석 어셈블리의 작동 주파수가 높을 때 더욱 증가한다. 위의 두 운전 변수는 자기 냉동 시스템의 냉방 용량을 높이기 위해 필수적이므로 시스템 압력 강하를 줄이는 것은 적은 소모 동력과 향상된 COP를 위해 중요하다. 한편, 자기 냉동 시스템에 대한 다양한 시뮬레이션 모델이 개발되었음에도 능동형 자기 재생기에 대한 에너지 방정식과 누셀 수가 대응되지 않는 경우가 많다. 마지막으로 자기 냉동 시스템에서의 보편적인 자기 칼로리 물질인 가돌리늄은 희토류이다. 따라서 자기 냉동 시스템의 상용화를 위해서는 궁극적으로 대안적인 소재로 대체되어야 한다. 따라서 본 연구에서는 자기 냉동 시스템의

운전 변수에 관한 연구를 시작으로 COP 향상을 위한 방안을 제시한다. 또한 자기 냉동 시스템에 대한 새로운 시뮬레이션 모델을 제안하고 $La(Fe,Mn,Si)_{13}H_y$ 합금의 질량 비율을 달리하는 성능 향상 방안을 소개한다.

본 연구의 2장에서는 자기 냉동 시스템의 운전 변수에 관한 연구가 진행되었다. 먼저, 자석과 능동형 자기 재생기의 상대적인 위치를 제어하는 위상 이동 변수를 제시하고, 전체 사이클에서 유체가 흐르는 시간에 대한 유량 비율 변수를 소개하였다. 또한 활용 계수, 운전 주파수 및 작동 온도의 시스템에 대한 영향을 평가하였다. 마지막으로 제2 법칙 효율을 구하기 위해 열원 온도의 영향을 확인하였다. 실험 결과, 자기 냉동 시스템 실험 장치는 11.5 K의 무부하 온도 차이를 보였다. 최대 냉방 성능은 1.128 Hz의 운전 주파수에서 4.82 W이며 시스템의 최고 COP는 2.40으로 나타났다. 또한 실험 결과를 토대로 최적의 작동 온도를 통해 자기 냉동 시스템의 소모 동력을 유지하며 냉방 출력 및 COP를 향상시킬 수 있는 것으로 확인되었다.

3장에서는 자기 냉동 시스템에서 능동형 자기 재생기 내부의 압력 강하를 감소시키기 위한 새로운 자기 칼로리 물질 배열 방법을 제시하였다. 먼저, 비정형 가돌리늄을 능동형 자기 재생기에 충전할 때 외부 자기장을 가하여 소재를 배열시켰다. 그리고 기존의

방법으로 충전된 능동형 자기 재생기와의 비교 실험을 진행하였다. 먼저 X선 단층 촬영 결과에 따르면 배열형 능동형 자기 재생기 내부에서는 가돌리늄 소재가 유동 방향과 평행하게 배열된 것을 확인하였다. 반면, 비 배열 능동형 자기 재생기의 경우 소재가 무작위로 배열되며 유동 방향과 상당히 수직한 것으로 보였다. 또한 마찰 계수는 배열형 능동형 자기 재생기에서 더 적은 것으로 나타났으며 이는 상당직경의 구형 소재 충전층보다 그 값이 작았다. 결론적으로 배열형 능동형 자기 재생기는 0.56Hz의 작동 주파수, 부하 조건 및 4.5K의 시스템 온도 차이에서 COP를 비 배열 능동형 자기 재생기 대비 최대 37.3%까지 향상시켰다.

4장에서는 능동형 자기 재생기 충전층에 대한 누셀 수에 대응하는 에너지 방정식을 활용하여 새로운 자기 냉동 시뮬레이션을 개발하였다. 또한 자기 냉동 시스템에서 양방향 유동에 의한 내부 냉방 부하를 고려하기 위해 부가 컴포넌트에 대한 시뮬레이션 모델링도 추가하였다. 시뮬레이션 결과는 실험 결과와 상당히 유사한 것으로 확인되었으나 시스템 내부 튜브에 의한 열용량 차이, 튜브 연결부의 접촉 저항 및 단순화된 형상으로 인한 차이도 분석되었다. 또한 본 시뮬레이션을 통해 열 전달 물질을 통해 측정된 능동형 자기 재생기 양단에서의 온도가 고체의 자기 칼로리 물질 평균 온도를 상당히 유사하게 표현하는 것으로 확인되었다.

마지막 장에서는 퀴리 온도가 다른 $La(Fe,Mn,Si)_{13}H_y$ 합금의 최적 질량 비율을 통한 자기 냉동 시스템 성능 향상 방안을 제시하였다. 무부하 시험에서는 중간의 퀴리 온도 소재의 질량이 증가할수록 시스템 온도 차가 증가하는 것을 확인하였다. 반면 해당 소재가 감소하면 시스템 최소 온도가 상승하며 이는 시스템 온도 차를 감소시켰다. 부하 실험을 통해서 최적의 질량비를 갖는 능동형 자기 재생기가 4.8 K의 시스템 온도 차에서 2.23 W의 냉방 출력과 0.8의 COP를 나타내었다. 결론적으로 퀴리 온도가 287.9, 292.7 및 297.6 K인 $La(Fe,Mn,Si)_{13}H_y$ 합금을 활용한 능동형 자기 재생기에서 최적 질량비는 각각 13.5, 58.0 및 41.4 g으로 확인되었다.

본 연구를 통해 저자는 자기 냉동 시스템에 대한 포괄적인 이해를 제시하고 그 상용화에 이바지하고자 한다.

주요어: 자기 냉동 시스템, 능동형 자기 재생기, 가돌리늄, 수치 해석, 복층 배열, 일차 상변화 물질

학 번: 2017-24111